Doctoral Dissertation

Catalytic Mechanism for Silane Water-Crosslinking Reaction in the Poly-α-Olefin System: Combined Insights from Kinetic and Quantum Chemical Studies

(ポリ-α-オレフィン系内にて進行するシラン水-架橋反応に対する触媒機構の速度論的・量子化学的研究)

2022 年 3 月

TANAKA SHOHEI

田中 祥平

Graduate School of Sciences and Technology for Innovation

Yamaguchi University, Japan

山口大学大学院創成科学研究科自然科学系専攻

Contents

Chapter 1

General Introduction

Polymer science is a relatively new and specialized field of materials science. The empirical use of polymeric materials derived from natural substances has been documented for centuries; however, the pioneering work of Hermann Staudinger in the 1920s provided the basis for the systematic understanding of this class of materials.[1-3] Staudinger discovered the molecular blueprints of natural and synthetic high-molecular-weight polymeric materials. His revolutionary concept, which involved linking numerous small monomer molecules via covalent bonds into macromolecules, marked the beginning of a new era in the molecular design of high-molecular-weight structural and functional polymeric materials. Since then, polymer science has developed and became technically demanded and industrially important.[4-7] Nowadays, synthetic polymers are ubiquitous and be increasingly used in numerous common everyday devices, such as desktops, laptops, smartphones, and tablets. Therefore, polymers are one of the most important material classes in our society, and their global annual production reached approximately 400 million tons in 2020.[8]

Polyolefins present numerous applications and have a large market share among polymeric materials.[9-13] Polyolefins are a group of thermoplastic polymers formed via polymerization of olefins, such as propylene, ethylene, isoprene, and butene, which are commonly obtained from natural carbon sources, such as crude oil and gas. Polyolefins, which can be linear or branched, contain only covalently bonded C and H atoms. The production of polyolefins started in research laboratories. Polyethylene was the first

polyolefin fabricated by Eric Fawcett and Reginald Gibson in the research laboratories of the Imperial Chemical Industries in 1933, and its commercial production started in 1938.[14] Approximately two decades after high-pressure free radical polymerization was used to fabricate polyethylene from ethylene, catalysts that promoted the production of linear high-molecular-weight polyethylene and other polyolefins under much lower pressures were developed. Therefore, the timeline for the development of polyolefins matches that of catalyst development. The method used to fabricate linear polyolefins was developed by Nobel laureate Karl Ziegler in the early 1950s.[15-20] Ziegler prepared high-density polyethylene by polymerizing ethylene at low pressure and ambient temperatures using mixtures of triethylaluminum and titanium tetrachloride. Giulio Natta, another Nobel laureate, used Ziegler's complex coordination catalysts to produce crystalline polypropylene.[21-25] These catalysts are currently referred to as Ziegler–Natta catalysts (Figure 1-1(A)). Additionally, in 1951, Paul Hogan and Robert Banks of Phillips Petroleum Company fabricated crystalline polypropylene while attempting to convert propylene into gasoline.[26-28] This discovery led to the development of a new chromium oxide-based catalyst, currently referred to as the Phillips catalyst (Figure 1-1(B)), which was used to fabricate polypropylene and high-density polyethylene in 1953. The Phillips and Ziegler–Natta catalysts have been the primary industrial catalysts used for fabricating polyolefins until 1979 when Walter Kaminsky reported the use of methylaluminoxane as the activator for metallocene catalysts (Figure 1-1(C)).[29-32] Kaminsky determined that owing to their homogeneous nature, metallocene-based catalytic systems were "significantly different from Ziegler–Natta catalysts." Olefin polymerization generates polyolefins with various geometrical and configurational arrangements known as tacticity. Having control over these arrangements is critical because tacticity affects the physical

properties of polymers. When monomers comprise olefinic C atoms attached to R groups and H atoms, chiral C atoms are obtained via polymerization. The R groups and H atoms of polymers can present two arrangements, as illustrated in Figure 1-2. The type of isomeric form obtained via polymerization is important and can induce three types of structures, namely “isotactic,” “syndiotactic,” and “atactic” (Figure 1-3).[33-35] Owing to their crystalline nature and good mechanical properties, isotactic polymers are preferred for commercial applications. Olefin metathesis polymerization, also known as ring-closure metathesis, was introduced in the 1970s by Grubbs and his colleagues and became an important organic synthesis method.[36-40] The stable Ru-based catalyst used for this reaction is presented in Figure 1-1(D). Subsequent studies advanced olefin metathesis polymerization, which became an increasingly versatile method for synthesizing new polymers. Furthermore, the scientific advances in the 1990s promoted the industrial use of new post or non-metallocene, which is the outcome of the recent advancements. These catalysts are easy to assemble, have high activity, and allow for good control over the desired polymer structures. This is reflected in the numerous uses of polyolefins in everyday life applications. However, because polyolefins are thermoplastics with low melt viscosity, their service temperature is low. Therefore, researchers should focus on modifying polyolefins to increase their thermal stability and promote their use at high temperatures.

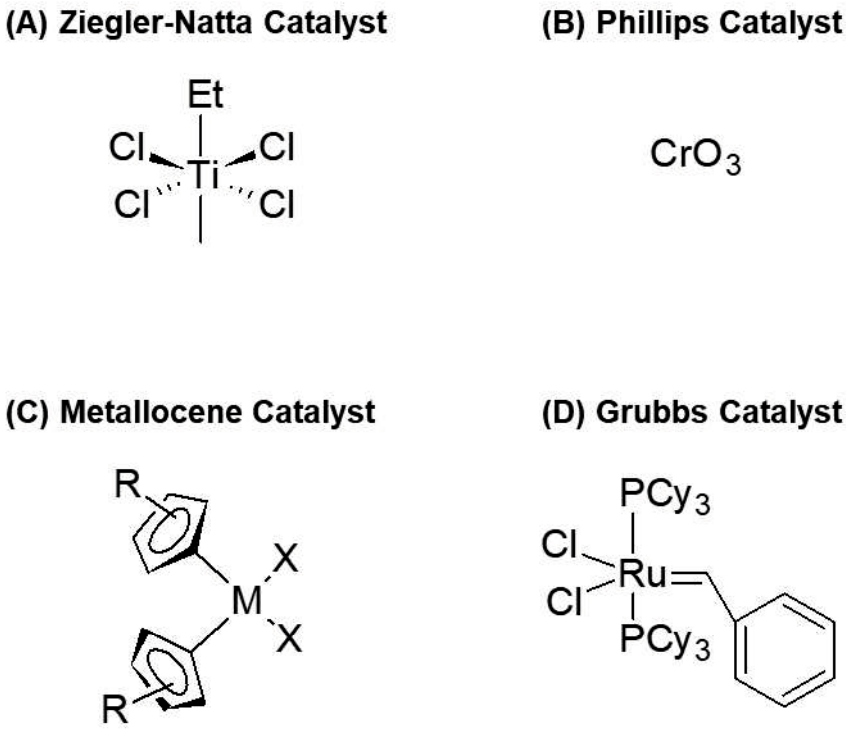

Figure 1-1. Structures of (A) Ziegler–Natta, (B) Phillips, (C) metallocene, and (D) Grubbs catalysts.

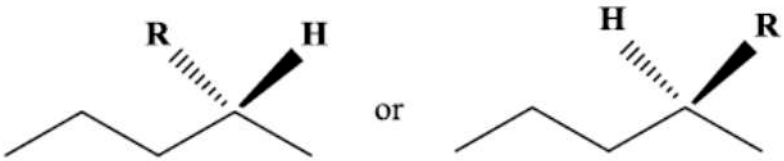

Figure 1-2. Typical steric structures of polyolefins

Isotactic : all repeated units show same configuration

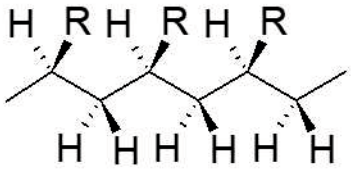

Syndiotactic : configuration of repeated units alternates between unit and the next in a synchronized manner

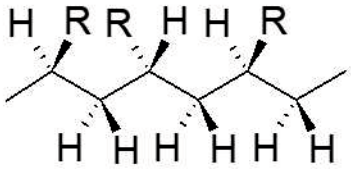

Atactic : Configuration of repeated units is placed randomly in an unpredictable manner

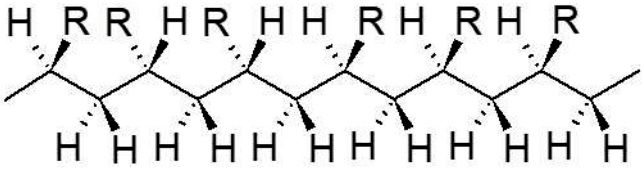

Figure 1-3. Polyolefin tacticity. The C atoms of the backbone are located in the plane of the page and the H atoms and R groups are oriented into or away from the page.

Crosslinking, which is broadly used for modifying polymeric materials, involves the formation of tridimensional structures and gels and causes significant changes in material properties.[41-45] The studies conducted by Goodyear and colleagues between 1838 and 1841 revealed that the strength an hardness of natural rubber increased upon heating with S, thereby demonstrating the practical importance of polyolefin crosslinking.[46,47] Nowadays, S is still the primary crosslinking agent. In 1948, Dole reported that the macroalkyl radicals obtained upon subjecting polyethylene to high-energy irradiation combined into three-dimensional networks via C–C crosslinkages, emphasizing the

critical industrial importance of polyolefin crosslinking.[48,49] The conversion of the approximately linear structure of polyolefin chains into three-dimensional structures via crosslinking significantly improved numerous polyolefin properties, such as their high-temperature properties, mechanical properties, and chemical/stress cracking resistance, and imparted polyolefins new useful properties, such as shape memory. Currently, three commercial methods are used for polyolefin crosslinking: (i) peroxide,[50-54] (ii) irradiation,[55-59] and (iii) silane–water-crosslinking.[60-69] Researchers started using peroxides as crosslinking agents during the 1970s because peroxides can be easily dispersed within the molding constituents and careful processing promotes the formation of uniform crosslinks throughout the products. Irradiation crosslinking is a "one-step" process involving irradiation of shaped polymers into crosslinked structures. These two crosslinking methods are initiated by the formation of macroalkyl radicals, which generate three-dimensional networks via C–C bonding; moreover, they increase the molecular mass of polyolefins and improve some of their properties. However, these crosslinking processes present disadvantages, such as the high cost of irradiation equipment, the pre-curing step required for peroxide crosslinking, the inability to crosslink polyolefins with tertiary-bonded C atoms, such as polypropylene, using free radicals, and the formation of voids in cable insulation. The research efforts to improve crosslinking methods led to the development of the silane–water-crosslinking method, which overcame some disadvantages of the conventional crosslinking methods and promoted the applications of crosslinked polyolefins.

Since the fabrication of water-crosslinkable silane-grafted polyolefins by Scott et al.[70] in the 1970s, they have been increasingly used in the polymer industry owing to the energy saving, low cost, and high productivity of the crosslinking method. The silane–

water-crosslinking method is based on the traditional silica sol–gel chemistry, and the reaction mechanism is presented in Scheme 1-1.[71-73] Alkoxysilane groups are first introduced onto the polyolefin backbone via peroxide-initiated grafting of unsaturated alkoxysilane. Next, water-crosslinked polyolefins with siloxane networks (Si–O–Si) are formed through catalytic hydrolysis and condensation reactions using water or moisture as the reaction trigger. In the absence of catalysts, water-crosslinking reactions in polyolefin systems are slow. Therefore, catalysts should be used for the hydrolysis and condensation reactions to shorten curing time and promote formation of fully crosslinked materials. Organotin compounds (OTCs), such as dibutyltin dilaurate (DBTL) or dioctyltin dilaurate act as catalysts to accelerate water-crosslinking of silane-grafted polyolefins.[74-77] Even though the OTCs-catalyzed silane–water-crosslinking reaction was developed in the 1950s, its mechanism is poorly understood and is still a matter of controversy. The “accepted” catalytic mechanism, as postulated by van Der Weij in the 1980s (Scheme 1-2) can be described as follows.[78-80] First, the OTCs react with free water molecules to form organotin hydroxides, which are considered to be the “true” catalysts of the water-crosslinking reaction. Thereafter, a nucleophilic attack at the alkoxysilane groups generates transient Sn–O–Si bonds. This promotes the attack of silanol (Si–OH) on the activated Si atoms, resulting in the formation of new Si–O–Si linkages in the polymer system. The critical step of the silane–water-crosslinking process is the initial reaction between the catalyst active sites and free water molecules, which serve as reaction initiators. This leads to the formation of nucleophilic species, which promote the hydrolysis and condensation of alkoxysilane moieties on the polyolefin backbone.

OTCs are ubiquitous for silane–water-crosslinking processes in the polymer industry owing to their excellent shelf life, short crosslinking time, and remarkable

selectivity. Nevertheless, high amounts of toxic OTCs have accumulated in water sediments, various aquatic organisms, and bird and mammal tissues. Owing to their potential noxious effects for humans, OTCs have already been banned in several countries. In Europe, the use of dibutyltin (DBT) compounds “in mixtures and articles used by the general public” has been prohibited since July 2012. Moreover, the use of DBT for fabricating one- and two-component room-temperature vulcanization (RTV) sealants, adhesives, paints, and coatings has been banned in Europe since January 2015. Consequently, researchers worldwide have focused their attention on developing alternative, non-toxic, and environmentally benign catalysts to replace noxious Sn-based compounds.

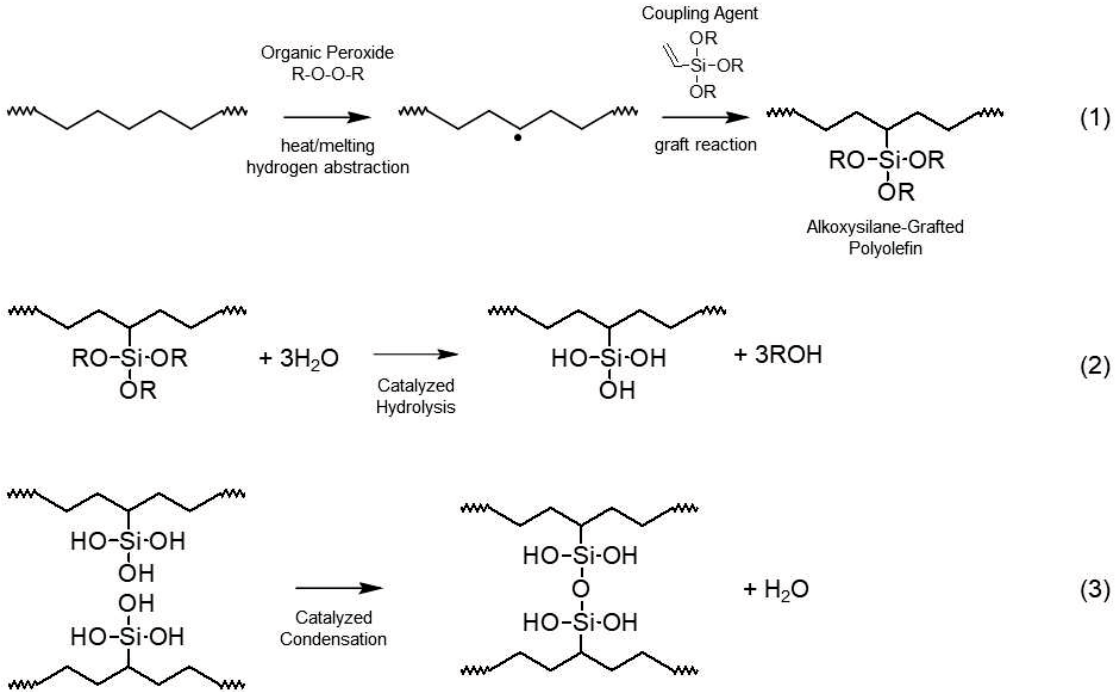

Scheme 1-1. Mechanism of the silane water-crosslinking reaction in polymer system.

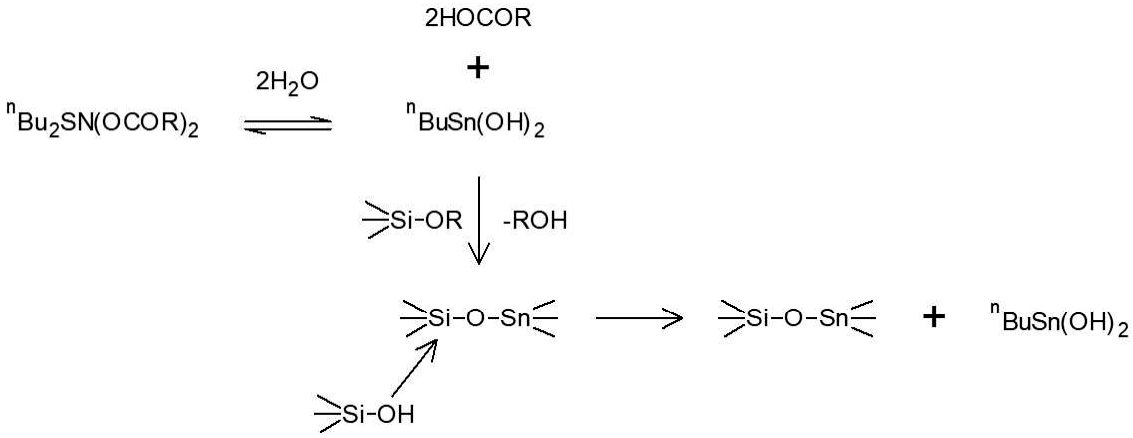

Scheme 1-2. Reported catalytic mechanism of the OTC-catalyzed silane water-crosslinking reaction.

Since the pioneering study on the utilization of organometal compounds as alternatives to OTC catalysts of Chu et al. in 1990, various types of organometal compounds have been used as catalysts for water-crosslinking reactions in polymer systems.[81-87] For example, metal alkoxides with Lewis acid metal ions as the catalytic active sites have been used as water-crosslinking catalysts.[88,89] In addition, metal complexes have been used as Lewis acid catalysts. Some of the most commonly used metal complex catalysts are copper complexes with Cu–O–C bonds, such as copper acetylacetonate.[90-93] Because of the acetylacetonate as the chelating agent, the stability of copper acetylacetonate significantly increases than those of metal alkoxide catalysts. In contrast to the abundance of metal-based catalysts, only a few organocatalysts are used for water-crosslinking reactions in polymer systems.[94-98] Since the Piers–Rubinsztajn reaction, namely the condensation of alkoxysilane with hydrosilane moieties, was developed in the 1990s, a boron compound, primarily trispentafulorophenylborane, have become a promising class of Lewis base crosslinking catalysts.[99,100] The aforecited studies demonstrated the effectiveness of boron compounds as water-crosslinking catalysts for the silane–water crosslinking reactions of polymer materials.

Metal complexes and aforementioned organic compounds act as Lewis acid and Lewis base catalysts, respectively. Lewis acid and base catalytic mechanisms for silane water-crosslinking reaction in polymer material show in Scheme 1-3. In hydrolysis reaction catalyzed by Lewis acids, Lewis acid is joining the O atom of water molecules, increasing the electrophilicity of the adjoining H atom and making more susceptible to nucleophilic attack.[101,102] The O atom in alkoxysilanes nucleophilic attacks to H atom in water molecules, and Si-O bond simultaneously forms. Eventually the intermediate gives a silanol, alcohol, and original Lewis acid catalyst. In the Lewis base catalyst case, Lewis

base acts as a nucleophile for a water molecule.[103] The water molecules activated by Lewis base are more conveniently employed as nucleophilic reactants to attack a Si atom of the alkoxysilane, and then form hypervalent penta-coordinated silicon complex. Eventually, the intermediate gives a silanol, alcohol, and original Lewis base catalyst. For the catalytic mechanism, the key step is the activation of the water by Lewis acid and base catalysts. Therefore, Lewis acidity and basicity of catalysts are critical factors in controlling the silane water-crosslinking reaction rate.

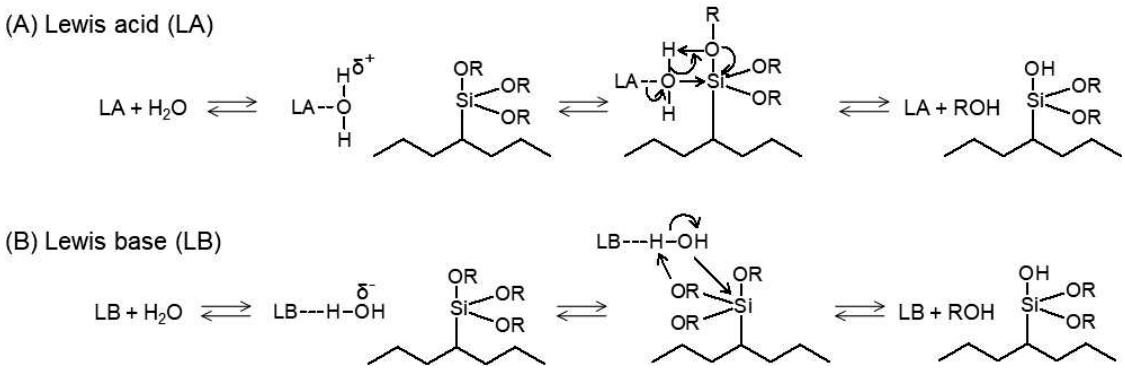

Scheme 1-3. Different mechanisms for catalyst performance in silane water-crosslinking reaction: (A) Lewis acid catalyst and (B) Lewis base catalyst.

Tuning the Lewis acidity and basicity of catalytic active sites can significantly change catalytic activity. Dinkar and coworkers demonstrated great potential for Zr-catalyzed system to effectively silane water-crosslinking reaction in comparison with other metal-catalyzed systems owing to strong Lewis acidity of Zr ion.[86] Several experimental proofs for the underlying different catalytic system for silane water-crosslinking reaction in polyolefin system have been carried out. However, the curing time and crosslinked density achieved using these catalysts have been inferior to those achieved using OTCs as catalysts. Thus, to date, OTCs is still the industrial "golden standard" catalysts for silane–water-crosslinking reaction.

Building blocks, such as ligands of metal complexes and substituents of organic compounds, are also important factors in controlling the Lewis acidity and basicity of catalysts. The electron withdrawing / donating properties of building blocks can change the electron affinity of catalytic active sites, leading to a more precise controlling of Lewis acidity and basicity. The crosslinking conditions and mechanical properties should be controllable to meet the requirement in each industrial applications. A precise control of Lewis acidity and basicity by building blocks will contribute to the development of tailor-made catalysts. Therefore, the establishment of the comprehensive design or modification guidelines of building blocks is an important issue.

The aim of this thesis is to introduce the concept of controllable catalytic performance by the electron withdrawing / donating properties of building blocks, and to find out crucial insight into designing complex and efficient catalytic systems. The selection of the catalytic active centers and design of the building blocks by themselves are insufficient for improving the performance of water-crosslinking catalysts; they should be combined for developing high-efficiency catalysts. Based on this strategy, I

focus on the clarification of the detailed effects of the building blocks on the performance of water-crosslinking catalysts. I describe in detail the effects of ligand structure on the performance of copper(II) β-diketonate (Cu(II)(βDiK)$_2$) complex as Lewis acid catalysts (Chapter 3) and those of substituents on the activity of organophosphorus compounds as Lewis base catalysts (Chapter 4). The findings in both Chapter 3 and Chapter 4 will lead to a new concept of tailor-made catalyst design for desired water-crosslinking reaction in polymer industry. Moreover, we report newly designed bifunctional water-crosslinking catalysts comprising Lewis acid and Lewis base catalysts (Chapter 5). Unlike the two-component acid and base co-catalyst system previously reported, the synthesized complexes present two types of catalytic active sites within the same molecule. If the acid-base bifunctional catalyst can work in the water-crosslinking reaction, it opens the door to a new guideline of a rational design for the silane water-crosslinking catalysis.

Chapter 3 describes the catalytic properties of the newly synthesized Cu(II)(βDiK)$_2$ complex catalysts for the water-crosslinking reaction of the 3-methacryloxypropyltrimehoxysilane–grafted ethylene–propylene copolymer (EPR-*g*-MTMS). Moreover, owing to their strong electron-withdrawing properties, curcuminoids can form Cu(II)(βDiK)$_2$ complexes that are more stable than those of other β-diketone (βDiK) ligands. Our results revealed that the Cu(II)(βDiK)$_2$ complexes presented good catalytic activity for the water-crosslinking reaction in the EPR-*g*-MTMS system, and the catalytic performance of the Cu(II)(βDiK)$_2$ complexes depended significantly on their stability. Furthermore, our results indicated that the catalytic behavior of the Cu(II)(βDiK)$_2$ complexes can be finely controlled by changing the electron-withdrawing/donating properties of the βDiK ligands.

Chapter 4 focuses on effects of substituents on the catalytic performance of organophosphorus compounds as Lewis base catalysts for the water-crosslinking reaction in the EPR-*g*-MTMS system. The catalyst, which presented a highly nucleophilic phosphoryl (P=O) moiety, promoted the silane water-crosslinking reaction in this system. The use of an electron-withdrawing substituent improved the Lewis basicity of the P=O moieties. Consequently, in this study, we improved the catalytic properties of organophosphoryl compounds by judiciously selecting the substituents and developed more efficient Lewis base catalysts than the previously reported catalytic system.

Chapter 5 describes a new concept of Lewis acid-based catalysts comprising Lewis acid metal complex and Lewis base alkylamine compounds for the water-crosslinking reaction in the EPR-*g*-MTMS system. The newly developed one-component catalyst possessed two types of catalytic active sites in one molecule. Therefore, we

determined that the synthesized acid–base hybrid catalyst exhibited bifunctional behavior as the silane water-crosslinking catalyst in the EPR-*g*-MTMS system.

References

1. H. Staudinger, *Ber. Dtsch. Chem. Ges.*, **1920**, *53*, 103-1085.
2. H. Frey, T. Johann, *Polym. Chem.*, **2020**, *11*, 8-14.
3. R. Mulhaupt, *Angew. Chem. Int. End.*, **2004**, *43*, 1054-1063.
4. S. Koltzenburg, M. Maskos, O. Nuyken, *Polymer Chemistry*, Springer Nature, Berlin, Germany, **2017**.
5. A. S. Adb-El-Aziz, et al., *Macromol. Chem. Phys.*, **2020**, *221*, 2000216.
6. P. Galli, G. Vecellio, *J. Polym. Sci. A Polym. Chem.*, **2004**, *42*, 396-415.
7. P. S. Chum, K. W. Swogger, *Prog. Polym. Sci.*, **2008**, *33*, 797-819.
8. Economic data presented on the homepage of the Ministry of Economy, Trade and Industry
9. J. Qiao, M. Guo, L. Wang, D. Liu, X. Zhang, L. Yu, W. Song, Y. Lin, *Polym. Chem.*, **2011**, *2*, 1611-1623.
10. C. E. Carraher, Jr., *Polymer Chemistry 6th ed.*, Marcel Dekker Inc., Florida, USA, **2003**.
11. M. A.-A. AlMa'adeed, I. Krupa, *Polyolefin Compounds and Materials Fundamentals and Industrial Applications*, Springer Nature, Berlin, Germany, **2016**.
12. P. Galli, J. C. Haylock, E. Albizzati, A. Denicola, *Macromol. Symp.*, **1995**, *98*, 1309-1332.
13. K. B. Nicole, A. H. Mare, *Chem. Soc Rev.*, **2005**, *34*, 267-275.
14. E. W. Fawcett, R. O. Gibson, *Polymerization of olefins*, US Patent US2153553A, **1939**.
15. K. Ziegler, E. Holzkamp, H. Breil, H. Martin, *Angew. Chem.*, **1955**, *67*, 541-547.

16. K. Ziegler, H. G. Gellert, *Polymerization of ethylene*, US Patent US2699457A, **1955**.

17. K. Ziegler H. Breil, E. Holzkamp, H. Martin, *Process for preparing high-molecular-weight polyethylene*, German Patent DBP973626, **1960**.

18. L. Bohm, *Angew. Chem. Int. Ed.*, **2003**, *42*, 5010-5030.

19. R. Mulhaupt, *Macromol. Chem. Phys.*, **2003**, *204*, 289-327.

20. M. Knickmeier, G. Erker, T. Fox, *J. Am. Chem. Soc.*, **1996**, *118*, 9623-9630.

21. G. Natta, P. Piero, M. Giorgio, *Isotactic polypropylene*, US Patent US3112300A, **1963**.

22. G. Natta, P. Piero, M. Giorgio, *Prevailingly isotactic polypropylene*, US Patent US3112301A, **1963**.

23. N. Kashiwa, *J. Polym. Sci. A Polym. Chem.*, **2004**, *42*, 1-8.

24. G. Natta, *Angew. Chem.*, **1964**, *76*, 553-566.

25. R. Waymouth, P. Piero, *J. Am. Chem. Soc.*, **1990**, *112*, 4911-4914.

26. J. P. Hogan, R. L. Banks, *Solid polymers of 4-methyl-1-pentene*, US Patent US4342854A, **1971**.

27. J. P. Hogan, R. L. Banks, *Solid polymers of olefins and production of such polymers*, US Patent US4376851A, **1956**.

28. D. S. McGuinness, N. W. Davies, J. Horne, I. Ivanov, *Organometallics*, **2010**, *29*, 6111-6116.

29. W. Kaminsky, *J. Polym. Sci. A Polym. Chem.*, **2004**, *42*, 3911-3921.

30. W. Kaminsky, H. Sinn, H.-J. Vollmer, R. Woldt, *Method for producing polymers and copolymers of ethylene*, German Patent DE3007725A1, **1981**.

31. W. Kaminsky, *Rend. Fis. Acc. Lincei*, **2017**, *28*, 87-95.

32. W. Kaminsky, *Macromolecules*, **2012**, *45*, 3289-3297.

33. G. W. Coates, *Chem. Rev.*, **2000**, *100*, 1223-1252.

34. W. Kaminsky, *Macromol. Chem. Phys.*, **2008**, *209*, 459-466.

35. H. Matsuda, T. Inoue, M. Okabe, T. Ukaji, *Polym. J.*, **1987**, *19*, 323-329.

36. R. H. Grubbs, W. Tumas, *Science*, **1989**, *243*, 907-915.

37. T. M. Trnka, R. H. Grubbs, *Acc. Chem. Res.*, **2001**, *34*, 18-29.

38. R. H. Grubbs, *J. Macromol. Sci. Chem. A*, **1994**, *31*, 1929-1833.

39. P. Schwab, M. B. France, J. W. Ziller, R. H. Grubbs, *Angew, Chem. Int. Ed.*, **1995**, *34*, 2039-2041.

40. R. H. Grubbs, A. Miyashita, *J. Am. Chem. Soc.*, **1978**, *100*, 7416-7418.

41. A. Bhattacharya, J. W. Rawlins, P. Ray, *Polymer Grafting and Crosslinking*, John Wiley & Sons, Inc., New Jersey, USA, **2009**.

42. G. Tiller, B. Boutevin, B. Ameduri, *Prog. Polym. Sci.*, **2011**, *36*, 191-217.

43. M. Muthukumar, H. H. Winter, *Macromolecules*, **1986**, *19*, 1284-1285.

44. K. A. Walker, L. J. Markoski, G. A. Deeter, G. E. Spilman, D. C. Martin, J. S. Moore, *Polymer*, **1994**, *35*, 5012-5017.

45. I. Chodak, *Prog. Polym. Sci.*, **1995**, *20*, 1165-1199.

46. M. Dole, *The History of the Crosslinking of Polyolefins*, Springer Nature, Berlin, Germany, **1986**.

47. C. Goodyear, *Gum Elastic and Its Varieties: With a Detailed Account of Its Applications and Uses and of the Discovery of Vulcanization, Vol. 2.*, New Haven, USA, **1853**.

48. M. Dole, *J. Macromol. Sci. Chem.*, **1981**, *15*, 1403-1409.

49. V. Stannett, T. Memetea, M. Dole, J. Salik, *J. Polym. Sci. Polym. Lett.*, **1978**, *16*, 63-65.

50. L. D. Loan, *J. Polym. Sci. A1*, **1964**, *2*, 3053-3066.

51. M. Akiba, A.S. Hashim, *Prog. Polym. Sci.*, **1997**, *22*, 475-521.

52. L. D. Loan, *J. Appl. Polym. Sci.*, **1963**, *7*, 2259-2268.

53. C. Twigg, K. Ford, S. Parent, *Polymer*, **2019**, *176*, 293-299.

54. Y. X. Wang, Y. Shi, C. C. Wang, J. H. Cheng, Y. Wang, W. J. Shao, L. Z. Liu, *J. Appl. Polym. Sci.*, **2021**, *138*, 50651.

55. A. Singh, *Radiat. Phys. Chem.*, **2001**, *60*, 453-459.

56. C. Beveridge, A. Sabiston, *Mater. Design*, **1987**, *8*, 263-268.

57. T. Zaharescu, R. Setnescu, S. Jipa, T. Setnescu, *J. Appl. Polym. Sci.*, **2000**, *77*, 982-987.

58. K. Makuuchi, S. Cheng, *Radiation Processing of Polymer Materials and its Industrial Applications*, John Wiley & Sons, Inc., New Jersey, USA, **2011**.

59. L. A. Kassekert, C. E. Dingwell, G. X. De How, M. A. Hillmyer, *Polym. Chem.*, **2020**, *11*, 712-720.

60. H. Yuan, Q. Shao, F. Liang, H. Shi, W. Song, *J. Appl. Polym. Sci.*, **2020**, *137*, 49534

61. J. Toynbee, *Polymer*, **1994**, *35*, 438-440.

62. N. C. Liu, G. P. Yao, H. Huang, *Polymer*, **2000**, *41*, 4537-4542.

63. C. Jiao, Z. Wang, Z. Gui, Y. Hu, *Eur. Polym. J.*, **2005**, *41*, 1204-1211.

64. A. K. Sen, B. Mukherjee, A. S. Bhattacharyya, P. P. De Anil, K. Bhowmick, *J. Appl. Polym. Sci.*, **1992**, *44*, 1153-1164.

65. H. Peng, M. Lu, F. Lv, M. Nu, W. Wang, *Polym. Bull.*, **2019**, *76*, 6413-6428.

66. M. Dana, G. H. Zohuri, S. Asadi, H. Salahi, *J. Macromol. Sci. A*, **2020**, *57*, 9-16.

67. J. Barzin, H. Azizi, J. Morshedian, *Polym. Plast. Technol. Eng.*, **2007**, *46*, 305-310.

68. H. Lu, Y. Hu, L. Yang, Z. Wang, Z. Chen, W. Fan, *J. Mater. Sci.*, **2005**, *40*, 43-46.

69. H. C. Kuan, J. F. Kuan, C. C. M. Ma, J. M. Huang, *J. Appl. Polym. Sci.*, **2005**, *96*, 2383-2391.

70. H. G. Scott, *Crosslinking of a polyolefin with a silane*, US Patent US3646155A, **1969**.

71. C. J. Brinker, G. W. Scherer, *Sol–gel science the physics and chemistry of sol–gel processing*, Academic Press, New York, USA, **1990**.

72. S. Al-Malaika, *Reactive modifiers for polymers*, Blackie Academic & Professional, London, UK, **1997**.

73. K. Adachi, T. Hirano, *Ind. Eng. Chem. Res.*, **2008**, *47*, 1812-1819.

74. D. Wang, J. Klein, E. Mejia, *Chem. Asian J.*, **2017**, *12*, 1180-1197.

75. J. Cervantes, R. Zarraga, C. S. Hernandez, *Appl. Organometal. Chem.*, **2012**, *26*, 157-163.

76. M. Nath, *Appl. Organometal. Chem.*, **2008**, *22*, 598-612.

77. R. Murai, S. Takahashi, S. Tanabe, I. Takeuchi, *Mar. Pollut. Bull.*, **2005**, *51*, 940-949.

78. F. W. van Der Weij, *Makromol. Chem.*, **1980**, *181*, 2541–2548.

79. V. Chandrasekhar, S. Nagendran, V. Baskar, *Coord. Chem. Rev.*, **2002**, *235*, 1-52.

80. K. Steliou, A. S. Nowosielska, A. Favre, M. A. Poupart, S. Hanessian, *J. Am. Chem. Soc.*, **1980**, *102*, 7578-7579.

81. C. Maliverney, D. Blanc, R. Ferhat, *Organopolysiloxane composition vulcanizable at room temperature into an elastomer, and novel catalysts for organopolysiloxane polycondensation*, French Patent WO2009103894A1, **2009**.

82. S. Dinkar, M. P. Maheshbai, A. Dhanabalan, *Moisture curable organopolysiloxane composition*, US Patent WO2013071078A1, **2013**.

83. C. Byrne, *Moisture curable organopolysiloxane composition,* US Patent WO2013101755A1, **2013**.

84. S. Cook, S. Han, M. Olsen, *Metal containing condensation reaction catalysts, methods for preparing the catalysts, and compositions containing the catalysts*, US Patent WO2015050583A1, **2015**.

85. S. Dinkar, E. J. Nesakumar, A. Dhanabalan, S. Murtuza, S. J. Landon, *Moisture curable organopolysiloxane composition*, US Patent WO2012033886A1, **2012**.

86. S. Dinkar, M. P. Maheshbai, A. Dhanabalan, *Moisture curable organopolysiloxane composition*, US Patent WO2013101751A1, **2013**.

87. H. R. He, R. J. Fraatz, M. J. P. Leiner, M. M. Rehnm J. K. Tusa, *Sens. Actuators B Chem.*, **1995**, *29*, 246-250.

88. Y. Liu, L. Deng, *J. Am. Chem. Soc.*, **2017**, 139, 1798-1801.

89. M. Huang, V. Kumar, R. Lim, C. Kondos, B. Okeefe, *Process for the preparation of silylated polyurethane polymers using titanium-containing and zirconium-containing catalysts*, US Patent US9321878B2, **2013**.

90. M. Guglie, G. Carturan, *J. Non-Cryst. Solids*, **1988**, *100*, 16-30.

91. C. Sanchez, J. Livage, M. Henry, F. Babonneau, *J. Non-Cryst. Solids*, **1988**, *100*, 65-76.

92. J. M. Vivar, C. J. Brinker, *J. Solgel Sci. Technol.*, **1994**, *2*, 393-397.

93. A. Verma, M. Kar, D. P. Singh, *J. Solgel Sci. Technol.*, **2010**, *54*, 129-138.

94. Q. Zhao, Q. Liu, H. Xu, Y. Bei, S. Feng, *RSC Adv.*, **2016**, *6*, 38447-38453.

95. K. Fuchise, M. Igarashi, K. Sato, S. Shimada, *Chem. Sci.*, **2018**, *9*, 2879-2891.

96. C. Thomasa, B. Bibal, *Green Chem.*, **2014**, *16*, 1687-1699.

97. J. Chojnowski, M. Cypryk, K. Kazmierski, *Macromolecules*, **2002**, *35*, 9904-9912.

98. N. Matsushita, K. Wakabayashi, T. Okamoto, *Curable composition*, Japanese Patent WO200094273A1, **2007**.

99. D. J. Parks, W. E. Piers, *J. Am. Chem. Soc.*, **1996**, *118*, 9440-9441.

100. J. M. Blackwell, K. L. Foster, V. H. Beck, W. E. Piers, *J. Org. Chem.*, **1999**, *64*, 4887-4892.

101. R. Wakabayashi, K. Kuroda, *ChemPlusChem*, **2013**, *78*, 764-774.

102. F. Liu, T. Wang, Y. Zheng, J. Wang, *J. Catal.*, **2017**, *355*, 17-25.

103. M. Kozelj, B. Orel, *Dalton Trans.*, **2013**, *42*, 9432-9436.

Chapter 2

Theory

In this study, we focused primarily on catalytic activation in polymer matrices. Understanding the thermodynamic underpinnings of the phase behavior of polymer solutions is critical. In this chapter we summarize the theories and models used to describe the phase behavior of polymer solutions.

Ideal and regular solution theories

The macroscopic behavior of physical systems is determined by two fundamental statements, which form the basis of thermodynamics: the first and second laws of thermodynamics. The first law of thermodynamics, which is also known as the law of conservation of energy, states that only processes that conserve energy can occur spontaneously. However, all real-life processes involve spontaneous changes. The second law of thermodynamics indicates the direction of such spontaneous changes. According to this law, any spontaneous changes in the state of an isolated system lead to an increase in its entropy (S), which is a state function. Therefore, to determine whether processes, such as phase separations and mixing, can occur spontaneously in a system, the changes in the total entropy of the system (ΔS) should be determined.

Under constant temperature and pressure conditions, the typical thermodynamic criteria for miscibility consist of a negative change in the Gibbs free energy of the system upon mixing (ΔG_{mix}). Conventionally, concentration is expressed as mole or volume fractions. The first condition is a universal requirement for any spontaneous process,

whereas the second condition ensures the stability of liquid mixtures. ΔG_{mix} can be calculated as follows:

$$\Delta G_{mix} = \Delta H_{mix} - T\Delta S_{mix}, \quad (2.1)$$

where ΔH_{mix}, T, and ΔS_{mix} are the enthalpy change during mixing, absolute temperature, and entropy change during mixing, respectively. ΔS_{mix} is always positive for mixing processes since mixing generates more available configurations for the entire mixture. However, ΔH_{mix} can be negative, zero, or positive depending on the nature of the intermolecular forces between system components. Consequently, the sign of ΔG_{mix} depends primarily on the sign and magnitude of ΔH_{mix}. This is especially important for macromolecular species.

The lattice fluid model for mixtures of two low-molecular-weight liquids is presented in Figure 2-1. For mixtures of two fluids (i.e., fluids A and B), three nearest neighbor interactions, namely w_{AA}, w_{BB}, and w_{AB}, occur. The simplest molecular-based solution theory is the ideal solution theory.[1] This theory is based on three assumptions: (i) the sizes of the molecules of all components are similar, (ii) the intermolecular interactions between components are non-directional and comparable in magnitude, and (iii) mixing is a random and entirely statical process. The first two assumptions imply that $\Delta H_{mix} = 0$; therefore, the spontaneity of the mixing process is exclusively determined by the increase in entropy caused by the extra degrees of freedom of each component in the solution. For binary systems, the corresponding entropy change upon mixing or configurational entropy can be expressed as follows:

$$\Delta S_{mix} = -R(n_A \ln x_A + n_B \ln x_B), \quad (2.2)$$

where n_i and x_i are the number of moles and mole fraction, respectively, of component i in the solution and R is the universal gas constant. Eq. (2.2) can be derived from the

Boltzmann law of entropy (i.e., $S = -k_B \ln \Omega$, where Ω is the number of microstates and k_B is the Boltzmann constant) and using the lattice model of concentrated solutions. According to the Boltzmann law of entropy, for non-ideal solutions, molecules of one type can congregate and not distribute uniformly in solution. Therefore, the configurational entropy of non-ideal solutions is lower than that estimated using Eq. (2.2). In other words, random mixing conditions provide an upper limit for ΔS_{mix}.

In 1929, Hildebrand introduced the non-ideal solution theory to describe the phase behavior of small-molecule liquid mixtures to develop a model for predicting activity coefficients.[2,3] According to this theory, different types of molecules have comparable sizes and ΔS_{mix} can be calculated using Eq. (2.2). The non-ideality of solutions or excess thermodynamic properties are ascribed entirely to the differences in intermolecular interactions between solution components. Because mixing is random, ΔH_{mix} can be determined as follows. The average number of type B molecules that are the nearest neighbor to a selected type A molecule is zx_B, where z is the coordination number. The total number of A–B pairs in solution is $n_A z x_B$. The pair interaction energy between molecules A and B (w) can be expressed as follows:

$$w = (w_{AA} + w_{BB}) - 2w_{AB}, \quad (2.3)$$

where w_{ij} is the energy required to separate molecule types i and j.

$$\Delta U_{mix} = n_A z x_B w = nzw x_A x_B, \quad (2.4)$$

where ΔU_{mix} is the change in internal energy of the solution during mixing.
Since the pressure–volume effects are not considered in the lattice model, $\Delta U_{mix} = \Delta H_{mix}$; therefore:

$$\Delta H_{mix} = nzw x_A x_B, \quad (2.5)$$

where w can be negative, zero, or positive. If w_{AB} is equal to the numerical average of the interaction energies of the pure individual components, that is:

$$w_{AB} = \frac{w_{AA} + w_{BB}}{2}, \quad (2.6)$$

then $w = 0$ and $\Delta H_{mix} = 0$. By combining Eqs. (2.2) and (2.5), ΔG_{mix} can be expressed as follows:

$$\Delta G_{mix} = nzwx_A x_B + RT(n_A \ln x_A + n_B \ln x_B) \quad (2.7)$$

Because activity coefficients are related to the derivatives of the excess ΔG_{mix}, Eq. (2.7) can be used to calculate activity coefficients. Many small-molecule liquids conform to the phase behavior predicted by Eq. (2.7). However, if quantitative agreement is desired, the dependence of the product zw on composition and temperature should be considered, because mixing is not a purely statistical process owing to intermolecular interactions and local concentration fluctuations. If strong repulsive or attractive forces manifest between system components, the ideal entropy approximation cannot be properly used. The greater the zw value is, the larger the deviation of the calculated entropy from the actual value. Moreover, according to the non-ideal solution theory, the product zw should not depend on system composition. If $zw > 2RT$, phase separation occurs. In other words, if $zw/RT \leq 2$, mixtures consist of a single phase across their entire composition range.

By replacing the mole fractions with volume fractions in Eq. (2.5) and using the Scatchard geometric mean approximation,[4] Eq. (2.5) can be rewritten as follows:

$$\frac{\Delta H_{mix}}{V} = (\delta_A - \delta_B)^2 \phi_A \phi_B, \quad (2.8)$$

where δ_i is the Hildebrand solubility parameter of component i, V is the total volume of the liquid mixture, and ϕ_i is the volume fraction of component i. Typically, δ_i can be calculated as follows:

$$\delta = \left(\frac{\Delta U_v}{V_l} \right)^{0.5} \quad \text{..... (2.9)}$$

where ΔU_v and V_i are the internal energy change of vaporization and molar volume of the liquid at room temperature, respectively. In other words, δ is a measure of the strength of intermolecular interactions in pure liquids. According to Eq. (2.8), two liquids with similar δ values should be thermodynamically miscible. Since this concept is straightforward and simple to apply, it has been widely used to predict the miscibility of various materials, including petroleum liquids and polymers. Moreover, δ values can be used to calculate activity coefficients. According to the geometric mean assumption, $\Delta H_{mix} > 0$ and the activity coefficients are greater than 1.

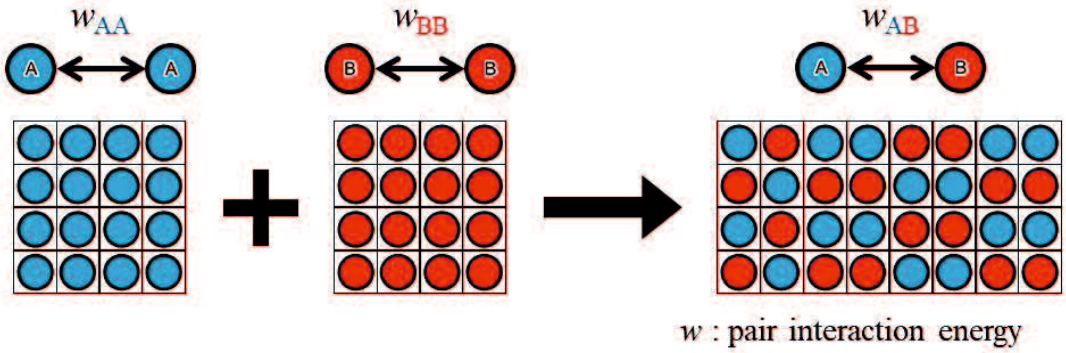

	Ideal Solution Theory	Regular Solution Theory
ΔS_{mix}	$\Delta S_{mix} = -R(n_A \ln x_A + n_B \ln x_B)$	$\Delta S_{mix} = -R(n_A \ln x_A + n_B \ln x_B)$
ΔH_{mix}	0 $w_{AA} = w_{BB} = w_{AB}$	$\Delta H_{mix} = nzwx_A x_B$ $w_{AA} \neq w_{BB} \neq w_{AB}$
ΔG_{mix}	$\Delta G_{mix} = RT(n_A \ln x_A + n_B \ln x_B)$	$\Delta G_{mix} = nzwx_A x_B + RT(n_A \ln x_A + n_B \ln x_B)$

Figure 2-1. Schematic of the lattice model of randomly mixed concentrated binary solutions containing molecule types A and B (top). Summary of the ideal and non-ideal solution theories (bottom).

Flory-Huggins Theory

Understanding the thermodynamic underpinning of the phase behavior of polymer solutions and mixtures began with the Flory–Huggins theory.[5-8] According to this theory, the interactions between different types of polymer chains are governed by a parameter related to the interactions at the monomer length scale and chain lengths. To model polymer solutions, we considered a mixture comprising polymer A and solvent B (Figure 2-2). Moreover, we hypothesized that the volume of the system did not change upon mixing; that is $V_A + V_B$ = constant. The mixture was macroscopically uniform, and the components were mixed randomly to fill the entire lattice. The volume fractions of the components of the binary mixture (ϕ_A and ϕ_B) can be expressed as follows:

$$\phi_A = \frac{V_A}{V_A + V_B} \text{ and } \phi_B = \frac{V_B}{V_A + V_B} = 1 - \phi_A \quad \text{..... (2.10)}$$

Similar mixing can occur if one or both mixed species are polymers. Typically, the lattice site volume (v_0) is defined as the volume of the smallest unit (solvent molecule or monomer), and larger molecules occupy multiple connected lattice sites. The molecular volumes of species A and B can be expressed as follows:

$$v_A = N_A v_0 , \quad \text{..... (2.11)}$$

$$v_B = N_B v_0 , \quad \text{..... (2.12)}$$

where N_A and N_B are the numbers of lattice sites occupied by molecules A and B, respectively.

Using the same approach to that used for the non-ideal solution theory, Flory and Huggins yielded the following expressions for ΔS_{mix} and ΔH_{mix} for binary polymer solutions:

$$\Delta S_{mix} = -R\left(\frac{\phi}{N}(\ln\phi) + (1-\phi)\ln(1-\phi)\right), \quad \text{..... (2.13)}$$

$$\Delta H_{mix} = \chi RT\phi(1-\phi), \quad \text{..... (2.14)}$$

where ϕ is the volume fraction of a monodisperse and linear polymer with a chain length of N, $(1-\phi)$ is the volume fraction of the solvent, and χ is the Flory–Huggins interaction parameter. ΔS_{mix} and ΔH_{mix} are expressed per mole of lattice sites. ΔG_{mix} can be calculated by combining Eqs. (2.13) and (2.14), and the results can be used to evaluate the corresponding activity coefficients. Typically, χ is defined as zw/RT. Herein, χ was considered to be concentration-independent and was inversely proportional to the temperature. Combining Eqs. (2.14) and (2.11), χ can be expressed as follows:

$$\chi = V\frac{\left(\delta_p - \delta_s\right)^2}{RT}, \quad \text{..... (2.15)}$$

Where δ_p and δ_s are the Hildebrand solubility parameters of the solvent and polymer, respectively. According to Eq. (2.15), χ depends on the reference volume used. The χ values determined using Eq. (2.15) are positive owing to the geometric mean assumption.

The ΔS_{mix} values calculated using Eq. (2.13) were determined assuming athermal mixing, which requires that macromolecules in solutions have no preferred conformation at the molecular level and do not interact with each other or with the solvent molecules through directional-dependent specific intermolecular interactions. Athermal mixing conditions are appropriate for polymer solutions containing linear, flexible, and non-polar macromolecules and non-polar solvents. In other words, if a polymer solution contains constituents with similar local structures or the constituents interact with each other via directional-specific intermolecular interactions, such as hydrogen bonding, π–π interactions, dipole–aromatic ring induction, ion paring, coordination with metallic ions, acid–base and charge-transfer interactions, the configurational entropy after mixing is considerably smaller than that associated with athermal mixing. Therefore, Eq. (2.14) is not appropriate for such solutions because mixing is not random. Moreover, the

mathematical relationship between w_{AA}, w_{BB}, and w_{AB} is complex. Therefore, Eq. (2.15) cannot be used to express the relationship between the χ, δ_s, and δ_p.

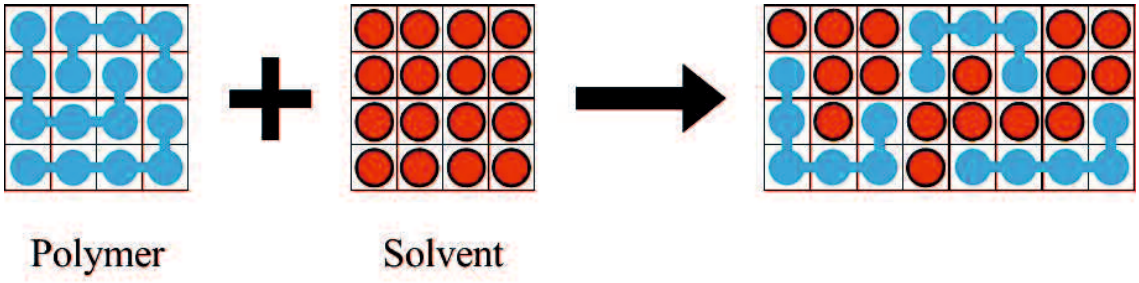

Figure 2-2. Schematic of the lattice model of a polymer–solvent mixture.

Flory-Rehner Theory

The typical benchmark for the theoretical description of swelling processes in crosslinked polymers is the Flory–Rehner theory, which is an extension of the phase theory for polymer solutions.[9-12] According to this theory, gels reach thermodynamic equilibrium when the chemical potentials of the solvent (μ_s) inside and outside the gel are equal:

$$\mu_s^{in} = \mu_s^{out} \quad \text{..... (2.16)}$$

Eq. (2.16) can be rewritten in terms of the osmotic pressure (Π), as follows:

$$\Pi = -\frac{\mu_s^{in} - \mu_s^{out}}{v_s} = 0, \quad \text{..... (2.17)}$$

where v_s is the molar volume of the solvent. Conversely, Π can be calculated from the change in Helmholtz free energy (ΔF), as follows:

$$\Pi = -\frac{N_A}{v_s}\frac{\partial \Delta F}{\partial N_s}, \quad \text{..... (2.18)}$$

where N_A is the Avogadro's number and N_s is the number of solvent molecules. The thermodynamic properties of incompressible lattices can also be determined using the free energy or the Gibbs free energy, since, in theory, the volume of the system (polymer + solvent) cannot change. According to the Flory–Rehner theory, ΔF can be expressed as follows:

$$\Delta F = \Delta F_{mix} + \Delta F_{el}, \quad \text{..... (2.19)}$$

where ΔF_{mix} and ΔF_{el} are the mixing free energy and elastic contribution, respectively. Consequently, Π can also be expressed as the sum of two contributions:

$$\Pi = \Pi_{mix} + \Pi_{el}. \quad \text{..... (2.20)}$$

According to the Flory–Rehner theory for gel swelling, ΔF_{mix} can be expressed as follows:

$$\Delta F_{mix} = N_s k_B T[\ln(1-\phi) + \chi\phi], \quad \text{..... (2.21)}$$

where ϕ is the volume fraction of the gel. The physical meaning of χ at the microscopic level can be determined using the lattice theory of solutions. If $\chi > 0$, ΔF_{mix} increases and the transfer process and mixing are not energetically favorable. In contrast, if $\chi < 0$, ΔF_{mix} decreases and the transfer is energetically favorable.

Combining Eqs. (2.18) and (2.21), Π_{mix} can be expressed as follows:

$$\Pi_{mix} = -\frac{N_A k_B T}{v_s}[\phi + \ln(1-\phi) + \chi\phi^2] \quad \text{..... (2.22)}$$

This calculation is not trivial since ϕ depends on N_s.

In their original work, Flory and Rehner assumed that each chain vector changed linearly with macroscopic deformation. For this ideal case, referred to as an affine network, the change in entropy associated with isotropic deformation can be calculated as follows:

$$\Delta S_{el} = \frac{3N_c k_B}{2}(\ln\alpha - \alpha^2 + 1), \quad \text{..... (2.23)}$$

where N_c is the number of chains in the network and α is the linear swelling ratio. Typically, α can be expressed as follows:

$$\alpha = \left(\frac{V}{V_0}\right)^{1/3} = \left(\frac{\phi_0}{\phi}\right)^{1/3}, \quad \text{..... (2.24)}$$

where V is the volume of the system at a given state and the subscript 0 refers to the reference state. However, this reference state is not well-defined for gels prepared in the presence of solvents, and its determination is still a controversial issue. Because elastic forces in polymer materials arise primarily from a decrease in deformation entropy, it can be concluded that

$$\Delta F_{el} \cong -T\Delta S_{el} = -\frac{3N_c k_B}{2}(\ln\alpha - \alpha^2 + 1) \quad \text{..... (2.25)}$$

Consequently, Π_{el} can be calculated as follows:

$$\Pi_{el} = -\frac{N_c k_B T}{V_0}\left[\frac{\phi}{2\phi_0} - \left(\frac{\phi}{\phi_0}\right)^{\frac{1}{3}}\right] = -n_c k_B T\left[\frac{\phi}{2\phi_0} - \left(\frac{\phi}{\phi_0}\right)^{\frac{1}{3}}\right], \quad \text{(2.26)}$$

where $n_c = N_c/V_0$ is the number of chains per unit of volume in the reference state.

Using Eqs. (2.20), (2.22), and (2.26), Π can be expressed as follows:

$$\Pi = -\frac{N_A k_B T}{v_s}\left[\phi + \ln(1-\phi) + \chi\phi^2\right] + n_c k_B T\left[\frac{\phi}{2\phi_0} - \left(\frac{\phi}{\phi_0}\right)^{\frac{1}{3}}\right] \quad \text{(2.27)}$$

$\Pi = 0$ if the gel is at equilibrium with the surrounding solvent. This condition is also necessary to minimize the free energy. From Eq. (2.27), this condition can be expressed as follows:

$$\phi + \ln(1-\phi) + \chi\phi^2 = \frac{n_c v_s}{N_A}\left[\frac{\phi}{2\phi_0} - \left(\frac{\phi}{\phi_0}\right)^{\frac{1}{3}}\right] \quad \text{(2.28)}$$

Consequently, the well-known Flory–Rehner equation can be expressed as follows:

$$M_c = -V\rho_p \frac{\left(\phi_p^{\frac{1}{3}} - \frac{\phi_p}{2}\right)}{\left[\ln\left(1 - \phi_p\right) + \phi_p + \chi\phi_p^{\,2}\right]}, \quad \text{(2.29)}$$

where M_c is the average molecular weight between crosslinks, V is the molar volume of the solvent, ρ_p is the polymer density, and ϕ_p is the volume fraction of polymer in the swollen gel. Typically, ϕ_p can be calculated as follows:

$$\phi_p = \frac{\rho_s M_d}{\rho_s M_d + \rho_p M_s}, \quad \text{(2.30)}$$

where ρ_s is the solvent density, and M_s and M_d are the masses of the polymer swelled with solvent after xylene extraction and dried polymer, respectively.

Eq. (2.30) can be used to determine the crosslinking characteristics of networks using the equilibrium swelling properties. Furthermore, M_c has been used as a critical parameter for characterizing crosslinked polymer networks.[13,14]

Gelation and gel fraction

Chain linking leads to progressively larger branched polymers. The polydisperse mixtures of the branched polymers thus obtained are known as sols. Upon further linking, larger branched polymers are obtained until the entire system is transformed into a single molecule. Such large molecules cannot dissolve in solvents but can swell. The thus-obtained "infinite polymers" are known as gels or networks and comprise finite branched polymers. The transition from systems comprising only finite branched polymers (sols) to systems containing infinite molecules (gels) is known as sol–gel transition or gelation, and the critical point where the gel starts forming is called the gel point (p_c).

The gel fraction is defined as the fraction of all monomers comprising the gel.[15,16] Each monomer is a part of the sol or the gel; therefore, the sum of the sol and gel fractions ($P_{sol}(p)$ and $P_{gel}(p)$, respectively) equals 1:

$$P_{gel}(p) + P_{sol}(p) = 1 \quad \text{..... (2.31)}$$

Below p_c, all monomers are either unreacted or comprise finite sized polymers; therefore:

$$P_{gel}(p) = 0, \; P_{sol}(p) = 1 \quad \text{for } p \leq p_c \quad \text{..... (2.32)}$$

In contrast, above p_c

$$P_{gel}(p) > 0, \; P_{sol}(p) < 1 \quad \text{for } p > p_c \quad \text{..... (2.33)}$$

$P_{gel}(p)$, which is the probability that a randomly selected monomer belongs to the gel phase, is the order parameter for gelation and indicates whether a reaction proceeds beyond p_c. The increase in $P_{gel}(p)$ is accompanied by a simultaneous decrease in $P_{sol}(p)$ at $p > p_c$. Because the order parameter does not change during sol–gel transition processes indicates that gelation is analogous to a continuous phase transition.

At $p \leq p_c$, all species are soluble in the solvent; therefore, the conventional dilute solution characterization methods can be used. At $p > p_c$, an insoluble gel fraction and a soluble sol fraction are present. Upon immersing the system in excess solvent, the gel fraction swells and the sol fraction slowly diffuses out of the swollen gel into the excess solvent. A convenient separation method is the Soxhlet extraction method (Figure 2-3). The solvent is boiled in a flask and condenses at the top of the extraction column, dripping down onto the swollen gel. The gel is placed inside a weighed glass thimble equipped with a fritted filter at the bottom. As the thimble is filled with solvent, the solvent flows through the filter, carrying with it the sol fraction. When the solvent outside the thimble reaches a certain level, it automatically siphons down into the boiling solvent in the bottom part of the experimental setup. The gel fraction is characterized by its swelling. After allowing the excess solvent to flow through the filter, the thimble and swollen gel are weighed to determine the mass of swollen gel. Thereafter, the solvent is removed under vacuum and the thimble is weighed again to determine the gel fraction.

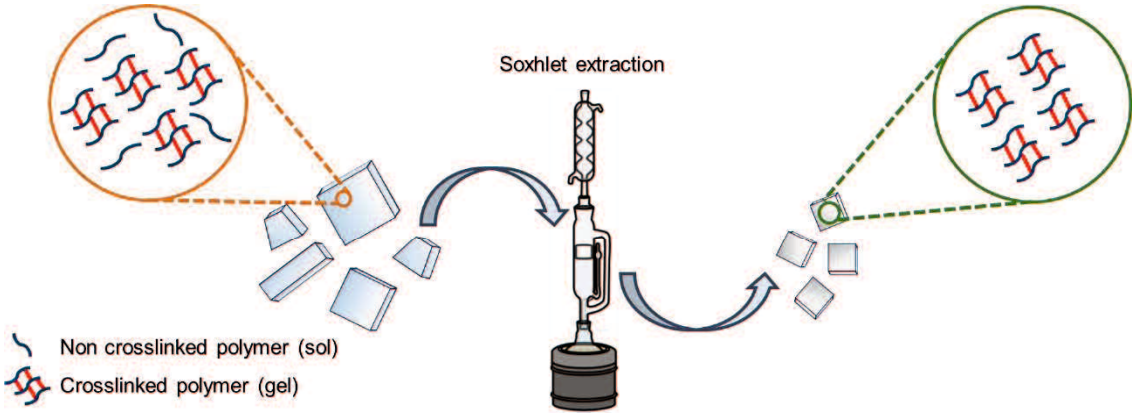

Figure 2-3. Schematic of Soxhlet extraction experimental setup for separating sol and gel fractions.

References

1. M. Rubinstein, R. H. Colby, *Polymer Physics*, Oxford University Press Inc., New York, USA, **2003**.
2. J. H. Hildebrand, *J. Am. Chem. Soc.*, **1929**, *51*, 66-80.
3. J. H. Hildebrand, R. L. Scott, *The Solubility of Nonelectrolytes 3rd ed.*, Dover, New York, USA, **1964**.
4. K. S. Schweizer, J. G. Curro, *Advances in Chemical Physics Vol. XCVIII*, John Wiley & Sons, Inc., New York, USA, **1997**.
5. P. J. Flory, *Principles of Polymer Chemistry*, Cornell University Press, New York, USA, **1971**.
6. M. L. Huggins, *J. Chem. Phys.*, **1941**, *9*, 440.
7. P. Choi, *Can. J. Chem. Eng.*, **2021**, *in press*.
8. Z. Xing, H. Lu, M. Hossain, *J. Appl. Polym. Sci.*, **2021**, *138*, e50304.
9. P. J. Flory, J. Rehner, *J. Chem. Phys.*, **1943**, *11*, 512-520.
10. P. J. Flory, J. Rehner, *J. Chem. Phys.*, **1943**, *11*, 521-526.
11. P. J. Flory, *J. Chem. Phys.*, **1950**, *18*, 108-111.
12. M. Q. Perez, J. A. M. Centeno, J. Forcada, R. H. Alvarez, *Soft Matter*, **2011**, *7*, 10536-10547.
13. F. Tanaka, E. F. Edwards, *Macromolecules*, **1992**, *25*, 1516-1523.
14. J. H. Lee, D. G. Bunknall, *J. Polym. Sci. Pol. Phys.*, **2008**, *46*, 1450-1462.
15. W. Burchard, *Solution Properties of Branched Macromolecules*, Springer, Berlin, Germany, **1999**.
16. Y. T. Shieh, J. S. Liau, T. K. Chen, *J. Appl. Polym. Sci.*, **2001**, *81*, 186-196.

Chapter 3

Effect of ligand structure on the catalytic activity of Cu(II)(βDiK)$_2$ complexes for the water-crosslinking reaction in a silane-grafted polyolefin system

Introduction

The water-crosslinking reactions in silane-grafted polyolefin systems occur via the hydrolysis and condensation reactions of the alkoxysilane groups grafted on the polyolefin backbone. In the absence of catalysts, alkoxysilane water-crosslinking occurs slowly in the presence of moisture. Therefore, the hydrolysis and condensation reactions should be catalyzed to shorten the curing time and obtain fully crosslinked materials. OTCs have been the most commonly used catalysts for these reactions. However, their removal from polyolefin matrices is often challenging, and deleterious catalyst residues are present in reaction systems. Several attempts have been made to replace Sn-based catalysts with more environmentally benign organometallic catalysts featuring Cu, Ti, and Zr, which act as Lewis acids. Recently, metal alkoxides have been used as Sn-free catalysts for fabricating sealants containing silane-grafted polyolefins via water-crosslinking (Scheme 3-1(A));[1] however, these types of catalysts are unstable in the presence of moisture; therefore, they can be easily hydrolyzed, which increases sealant curing time after storage in cartridges. To overcome these disadvantages, the effects of numerous chelating agents on the stability of metal ions were investigated. In particular, βDiK ligands can modify metal alkoxides into complexes, which effectively catalyze the

water-crosslinking reaction in silane-grafted polyolefin systems (Scheme 3-1(B)).[2-4] To precisely control the catalytic properties of metal complexes and develop highly functionalized water-crosslinking catalysts, the metal ion, which is the catalytic active site, should be deliberately selected, and the ligands should be judiciously designed.

Researchers have increasingly focused their attention on curcumin (1,7-bis(4-hydroxy-3-methoxyphenyl)-1,6-heptadiene-3,5-dione) and curcuminoids (curcumin derivatives) owing to their unique biological and pharmacological properties, such as antiinflammatory, antioxidant, and anticarcinogenic effects.[5,6] Moreover, a critical characteristic of plant-derived polyphenolic compounds, such as curcumin, is their ability to behave as bidentate chelators of metal ions, such as Cu(II) and Fe(III).[7-9] Mclean and Chandler demonstrated the primary role of the βDiK moiety within the heptadiene chain of curcumin in the coordination of metal ions.[10] In addition, Erika et al. demonstrated that the chelating ability of curcuminoids toward metal ions can be controlled by modifying the substituents in the meta and para positions of the peripheral phenyl rings.[11] Furthermore, recent studies revealed that the coordination of curcuminoids to metal ions significantly improved the Lewis acidity of metal ions, hence indicating the potential of metal–curcuminoid complexes as metal-based biological catalysts.

Inspired by this concept, we investigated the effect of the metal-chelating ability of several βDiK ligands on the catalytic performance of metal complexes for the silane–water-crosslinking reaction by using several curcuminoids and acetylacetones (acacs) as chelation agents (Scheme 3-2). Ultraviolet–visible (UV–vis) spectroscopic titrations and theoretical calculations revealed that the electron-withdrawing phenyl rings and extended π-conjugated structures of curcuminoids caused the electron densities on the βDiK moieties to increase, resulting in the formation of stable copper(II) complexes. The

catalytic activities of the Cu(II)(βDiK)$_2$ complexes for the water-crosslinking reaction in the EPR-*g*-MTMS system were investigated using attenuated total reflectance–Fourier-transform infrared (ATR–FTIR) spectroscopy. The kinetic results revealed that the hydrolysis activation energies of the EPR-*g*-MTMS systems containing various Cu(II)(βDiK)$_2$ complexes depended linearly on the stability constants of the corresponding complexes. This indicated that the highly stable Cu(II)(βDiK)$_2$ complexes exhibited remarkable catalytic activity for the silane–water-crosslinking reaction in polymer systems.

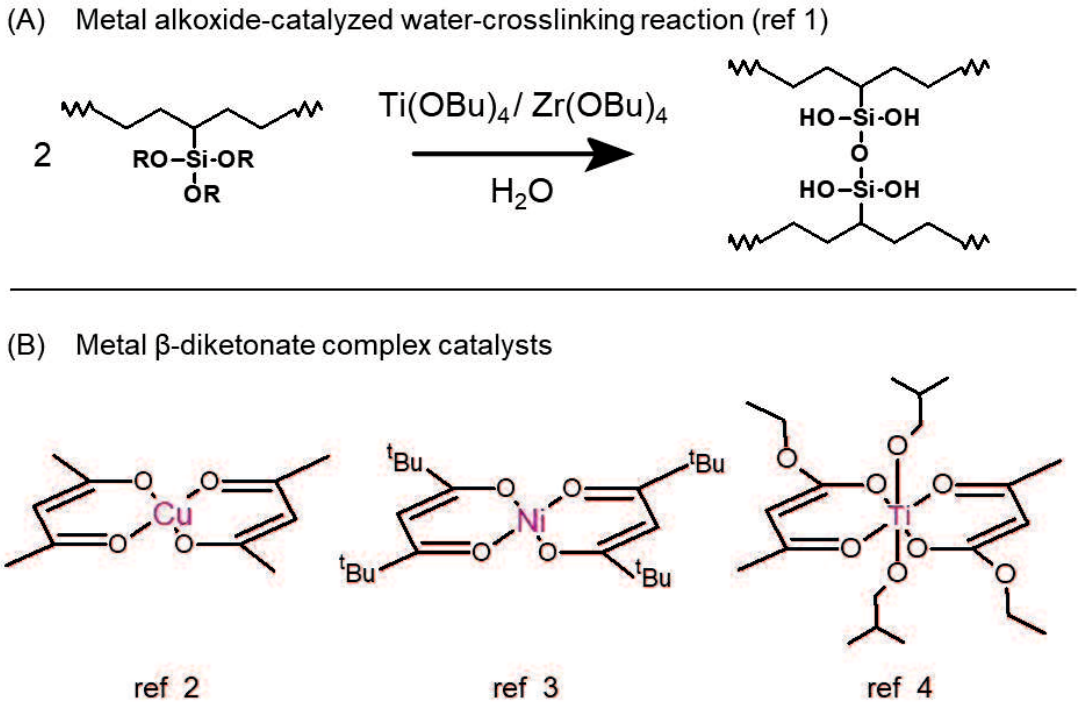

Scheme 3-1. (A) Metal-alkoxide-catalyzed water-crosslinking reaction.[1] (B) Metal β-diketonate complexes used as water-crosslinking catalysts in previous studies.[2-4]

Curcuminoid ligands

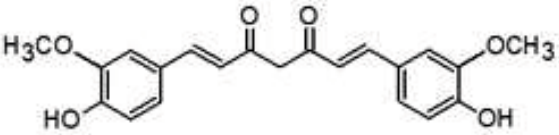

Curcumin
curc{Ph(OH)(OMe)}$_2$

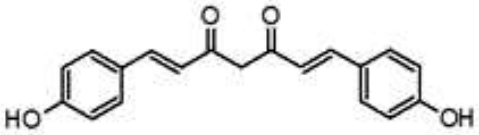

Bisdemethoxycurcumin
curc{Ph(OH)}$_2$

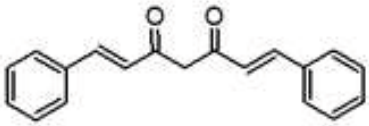

Bisdemethoxybisdehydroxylcurcumin
curc{Ph}$_2$

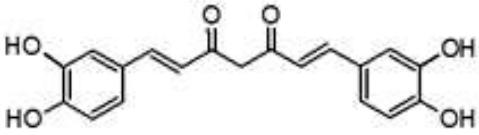

Tetrahydroxylcurcumin
curc{Ph(OH)$_2$}$_2$

Acetylacetone ligands

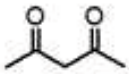

Acetylacetone
acac

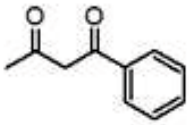

Phenylacetylacetone
acac{Ph}

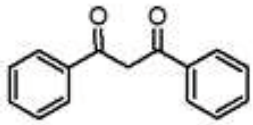

Diphenylacetylacetone
acac{Ph}$_2$

Scheme 3-2. Chemical structures of the curcuminoid and acetylacetone ligands used in this study.

Experimental

Materials

The ethylene–propylene copolymer (EPR) used in this study was purchased from Clariant Japan. The properties of the EPR are summarized in Table 3-1.[12] Curcumin (curc{Ph(OH)(OME)}$_2$), bisdemethoxycurcumin (curc{Ph(OH)}$_2$), bisacetylacetonatocopper(II) (99.9 % purity), 1-phenyl-1,3-butanedione, 1,3-iphenyl-1,3-propanedione, 2,4-pentadione, 3,4-dihydroxybenzaldehyde, benzaldehyde, tributyl borate, boron oxide, and *n*-butylamine were obtained from Tokyo Chemical Industry ((TCI); Tokyo, Japan); 3-methacryloxypropyltrimethoxysilane (MTMS; 98 % purity, USA) and dicumylperoxide (DCP; 98 % purity) were acquisitioned from Aldrich (City, PA, USA); and xylene (>80 % purity), acetone (>99 % purity), and methanol (>99 % purity) were acquired from Nacalai Tesque Inc. (Kyoto, Japan). All the chemicals were used as received.

Table 3-1. Properties of the ethylene–propylene copolymer used in this study.

M_w[a] / kg mol^{-1}	M_n/M_w[a]	crystallinity[b] / wt %	ethylene content[c] / mol %
27.7	2.3	34.9	10.1

[a] Number (M_n)- and weight (M_w)- averaged molecular masses.

[b] Determined by wide-angle X-ray scattering

[c] Determined by ^{13}C NMR

Synthesis of the curcuminoid ligands

Curc{Ph(OH)$_2$}$_2$ and curc{Ph}$_2$ were synthesized via the condensation of 2,4-pentadione with two equivalents of substituted benzaldehyde using the method of Bartob.[13] First, 2,4-pentadione (1.0 mol) and boron oxide (0.5 mol) were dissolved in ethylacetate (10 mL) and stirred for 30 min at 80 °C. Thereafter, benzaldehyde (2.0 mol)

and tributyl borate (0.02 mol) were added to the mixture. After 30 min, n-butylamine (0.4 mol), which served as the catalyst, was added dropwise over 30 min. After stirring at 80 °C for 4 h, the mixture was allowed to rest overnight to complete the reaction. Next, the mixture was acidified with 30 mL of a 0.4 M HCl solution, and the aqueous layer was extracted three times with ethyl acetate. The combined organic layers were washed with water and dried over Na_2SO_4. After solvent removal under low pressure, the residual paste was purified via column chromatography.

Curc{Ph(OH)$_2$}$_2$: 22 % yield from 3,4-dihydroxybenzaldehyde. Hydrogen nuclear magnetic resonance (^{1}H NMR) [400 MHz, $CDCl_3$]: δ 5.99 (s, 1H), 6.50 (d, J = 15.8 Hz, 2H), 6.88 (d, J = 8.6 Hz, 2H), 7.07 (d, J = 8.6 Hz, 2H), 7.19 (s, 2H), 7.53 (d, J = 15.8 Hz, 2H).

Curc{Ph}$_2$: 38 % yield from benzaldehyde. ^{1}H NMR [400 MHz, $CDCl_3$]: δ 5.86 (s, 1H), 6.64 (d, J = 16.0 Hz, 2H), 7.40 (m, 6H), 7.55 (m, 4H), 7.67 (d, J = 16.0 Hz, 2H).

Synthesis of the Cu(II)(βDiK)$_2$ complexes

The Cu(II)(βDiK)$_2$ complexes were synthesized by mixing methanolic solutions of the corresponding βDiK ligands with copper acetate at molar ratios of 2:1.[14] The βDiK methanolic solutions were prepared by adding 2.0 mol of each βDiK to 10 mL of methanol, followed by heating to 60 °C for dissolution. In addition, copper(II) acetate hydrate (1.0 mol) was dissolved in 100 mL of methanol under heating. The Cu(II)-containing methanolic solution was added to the βDiK solution and a dark-brown precipitate was produced immediately. Next, the mixture was refluxed for 2 h. Subsequently, the solid products were filtered and washed with cold methanol and then with water to remove the residual reactants. The purified products were dried under vacuum overnight, and the final

product was a dark-brown powder.

Cu(II)(curc{Ph(OH)(OME)}$_2$)$_2$: 78 % yield from copper(II) acetate. ^{1}H NMR [400 MHz, dimethyl sulfoxide (DMSO)-d_6] broad spectrum. Infrared (IR) (KBr pellet, cm^{-1}) 3508 (m), 2941 (w), 1619 (s), 1505 (s), 1415 (s), 1263 (s), 1153 (m), 976 (m).

Cu(II)(curc{Ph(OH)}$_2$)$_2$: 88 % yield from copper(II) acetate. ^{1}H NMR [400 MHz, DMSO-d_6] broad spectrum. IR (KBr pellet, cm^{-1}) 2931 (w), 1628 (s), 1508 (s), 1408 (s), 1280 (s), 1159 (m), 721 (m).

Cu(II)(curc{Ph}$_2$)$_2$: 85 % yield from copper(II) acetate. ^{1}H NMR [400 MHz, DMSO-d_6] broad spectrum. IR (KBr pellet, cm^{-1}) 2941 (w), 1624 (s), 1508 (s), 1404 (s), 1150 (m), 818 (m).

Cu(II)(curc{Ph(OH)$_2$}$_2$)$_2$: 71 % yield from copper(II) acetate. ^{1}H NMR [400 MHz, DMSO-d_6] broad spectrum. IR (KBr pellet, cm^{-1}) 3396 (s), 2938 (w), 1597 (s), 1505 (s), 1427 (s), 1270 (s), 1150 (m), 820 (m).

Cu(II)(acac{Ph})$_2$: 82 % yield from copper(II) acetate. ^{1}H NMR [400 MHz, DMSO-d_6] broad spectrum. IR (KBr pellet, cm^{-1}) 1590 (s), 1558 (s), 1516 (s), 1399 (s), 1314 (m), 774 (m), 706 (w).

Cu(II)(acac{Ph}$_2$)$_2$: 85 % yield from copper(II) acetate. ^{1}H NMR [400 MHz, DMSO-d_6] broad spectrum. IR (KBr pellet, cm^{-1}) 1592 (s), 1544 (s), 1525 (s), 1484 (w), 1399 (s), 759 (w), 707 (m).

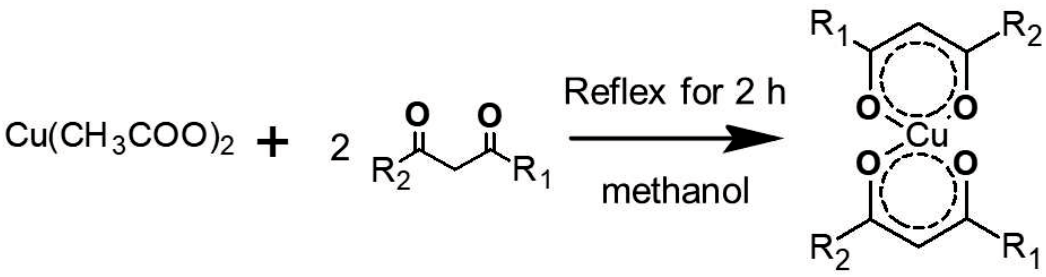

$R_1 = R_2$ = 1,7-bis(4-hydroxy-3-methoxyphenyl)-1,6-heptadiene : curc{Ph(OH)(Ome)}$_2$

$R_1 = R_2$ = 1,7-bis(4-hydroxyphenyl)-1,6-heptadiene : curc{Ph(OH)}$_2$

$R_1 = R_2$ = 1,7-bis(3,4-dihydroxyphenyl)-1,6-heptadiene : curc{Ph(OH)$_2$}$_2$

$R_1 = R_2$ = 1,7-diphenyl-1,6-heptadiene : curc{Ph}$_2$

$R_1 = R_2$ = methyl : acac

R_1 = phenyl, R_2 = methyl : acac{Ph}

$R_1 = R_2$ = Phenyl : acac{Ph}$_2$

Scheme 3-3. Synthesis of the Cu(II)(βDiK)$_2$ complexes.

UV–vis spectroscopic titration

To perform spectroscopic titrations, the curcuminoids were dissolved in methanol to obtain stock solutions (5.0×10^{-4} mol dm^{-3}). A stock solution of copper(II) acetate in methanol (5.0×10^{-3} mol dm^{-3}) was also prepared. The stock solution of copper(II) acetate was added to each curcuminoid methanolic solution in 1 cm quartz cuvettes to obtain mixtures with different Cu^{2+} ion:curcuminoid molar ratios. The prepared Cu(II)–curcuminoid solutions were stable for at least one week at room temperature. UV–vis spectra were obtained using a Shimadzu UV-1600 spectrometer. The changes in the UV–vis spectra of the mixtures obtained by adding the copper(II) acetate methanolic solution to the methanolic solutions of the acac-based ligands were measured using the same process. The stability constants of the Cu(βDiK)$_2$ complexes (K_{cpx}) were

calculated from the spectrometric data.

Computational methodology

All calculations were performed using the Gaussian 09 software package, and the GaussView 03 software was utilized to plot data for visualization.[15] The computations were performed using density functional theory (DFT) approaches, and the structures were fully optimized using the B3LYP hybrid-functional applied to the 6-31G basis set for C, H, and O atoms and the LANL2DZ basis set for Cu atoms.[16]

Silane grafting onto the EPR copolymer

Molten EPR-*g*-MTMS was prepared using DCP as the initiator, as previously described in the literature (Scheme 3-4).[17] In this study, we calculated the degree of silane grafting using ATR–FTIR spectroscopy. The ratio between the intensities of the absorbance peaks at 1095 cm^{-1} (A_{1095}), which was ascribed to the $–SiOCH_3$ groups, and 1460 cm^{-1} (A_{1460}; internal reference), which was attribute to the bending of $–CH_3$ groups, was used as an index of the degree of silane grafting onto the EPR. The obtained data indicated a good reproducibility of the experimental results. The silane grafting yield was approximately 90 % based on MTMS (detailed results are included in Appendix 1).

After grafting, the crosslinked catalyst (5.0×10^{-4} mol/100 g resin) was added to the EPR-*g*-MTMS resin melted at 120 °C. The resultant EPR-*g*-MTMS systems containing various $Cu(\beta DiK)_2$ complexes were removed and shaped into ~1.0 mm thick compression-molded sheets via air pressing. The sheets were cut into identical pieces, which were placed in water baths at 30, 50, or 80 °C. The samples were then removed from the water baths after various times to evaluate the reaction progress. To avoid undesired water-crosslinking while waiting for analysis or further treatment, the samples

were stored under dry conditions.

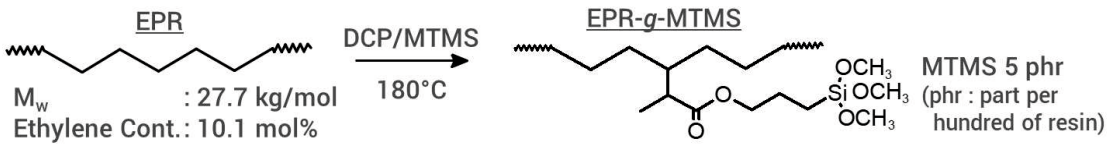

Scheme 3-4. Schematic of the melting and free radical grafting reactions used to fabricate EPR-*g*-MTMS.

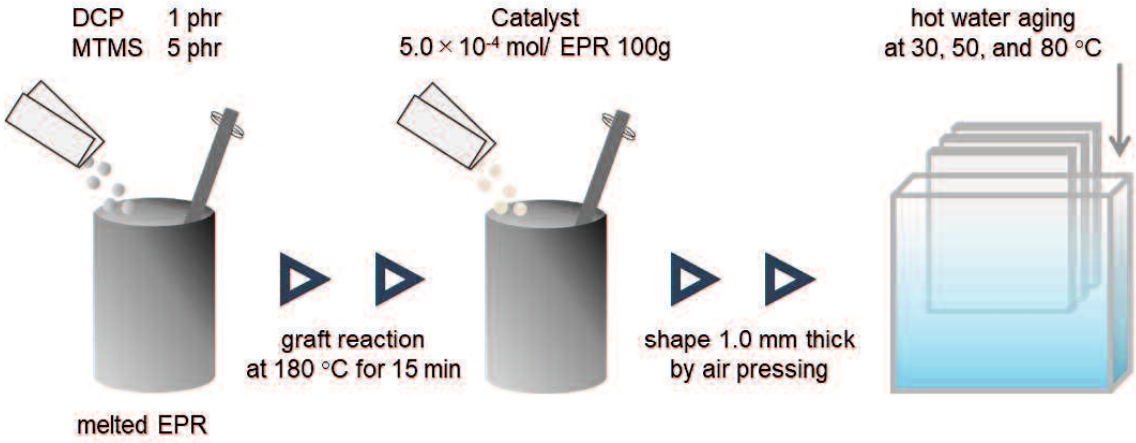

Scheme 3-5. Schematic of hot-water-aging of EPR-*g*-MTMS.

Kinetic analysis of the hydrolysis reaction of water-crosslinked EPR-*g*-MTMS

FTIR spectroscopy was used to analyze the alkoxysilane hydrolysis and condensation reactions in the EPR-*g*-MTMS system. The FTIR spectra were recorded using an AVATAR 370 spectrometer (Thermo Nicolet, City, State, USA) equipped with a Smart Orbit Ge ATR accessory (Thermo Nicolet, City, State, USA) in the wavenumber range of 800-4000 cm^{-1} with a resolution of 4 cm^{-1}. The average of 32 spectra was used to increase the signal-to-noise ratio.

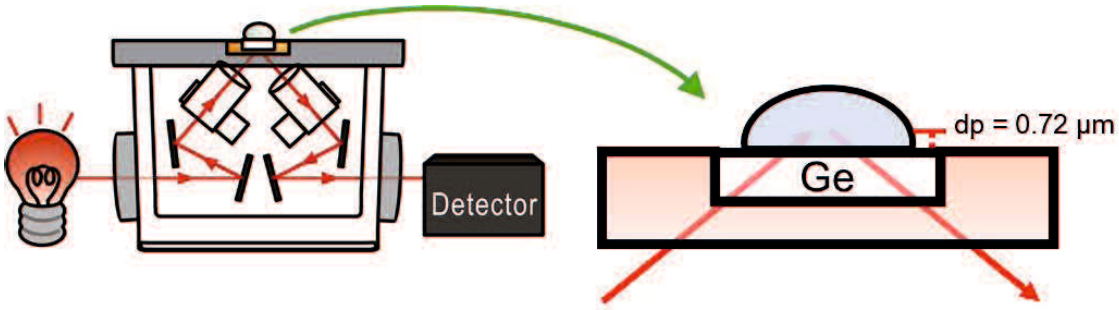

Scheme 3-6. Schematic of the experimental setup used to obtain the FTIR spectra..

The average molecular weight of between the water-crosslinked EPR-*g*-MTMS (M_c) was determined using the xylene extraction method. After water-crosslinking, the sheet samples were cut into small pieces. Subsequently, the material was placed in a wool filter, which was positioned in a standard Soxhlet extraction apparatus, and extraction was performed for 6 h. After in vacuo drying, the amount of residual resin was determined gravimetrically. Prolonging the extraction time did not affect the M_c values of the selected samples, and the EPR-*g*-MTMS samples that were not water-crosslinked contained no gel. According to the Flory–Rehner theory, M_c can be calculated as follows:

$$M_c = -V\rho_p \frac{\left(\sqrt[3]{\phi_p} - \frac{\phi_p}{2}\right)}{\left[\ln\left(1 - \phi_p\right) + \phi_p + \chi\phi_p^{\,2}\right]}, \quad \text{(3.1)}$$

where V is the molar volume of the solvent (V = 122 cm^3 mol^{-1}), ρ_p is the polymer density (ρ_p = 0.89 g cm^{-3}),[18] and ϕ_p is the volume fraction of polymer in the swollen gel. M_c is a critical structural parameter that can be used to characterize crosslinked polymers, and it is directly related to the crosslinking density. Typically, ϕ_p can be calculated as follows:

$$\phi_p = \frac{\rho_s M_d}{\rho_s M_d + \rho_p M_s}, \quad \text{(3.2)}$$

where ρ_s is the solvent density (ρ_s = 0.87 g cm^{-3}).[18]

Typically, χ can be calculated as follows:

$$\chi = V\frac{\left(\delta_s - \delta_p\right)^2}{RT}, \quad \text{(3.3)}$$

where δ_s and δ_p are the cohesive energy densities of the solvent and polymer, respectively. The δ_s and δ_p values used in this study are 18.3 and 15.2 MPa$^{0.5}$, respectively.[19]

Results and discussion

Characterization of the βDiK ligands used in this study

βDiK ligands, such as curcuminoids and acacs, must rise to di-keto/keto-enolic (DK/KE) equilibrium generated by proton dissociation. The UV–vis spectra of curcuminoids and acacs in dimethyl sulfoxide (DMSO)–water mixed solutions changed as the solution pH was increased from 5 to 10 (Figs. 3.1 and 3.2, respectively). The acid dissociation constants of the curcuminoids and acacs (K_a) were determined using the spectral changes, and the values are listed in Table 3-2. The K_a values decreased as follows: curc{Ph}$_2$ < curc{Ph(OH)}$_2$ < curc{Ph(OH)$_2$}$_2$ < curc{Ph(OH)(OMe)}$_2$ < acac{Ph}$_2$ < acac{Ph} < acac. Curcuminoids contain π-conjugated structures, which caused charge delocalization. Owing to the π-conjugated structures, the stabilizing activity of curcuminoids on the DK was stronger than that of the acacs. Additionally, the proton dissociation constants of the curcuminoids were remarkably affected by the substituents on their phenyl rings owing to the difference in electronegativity between substituents. As the number of substituents with electron-donating properties of the phenyl rings, such as hydroxyl and methoxy groups, decreased, the electron-withdrawing properties of the curcuminoids increased. Consequently, from an electronic standpoint, the DK forms of the curcuminoids became more stable than their KE forms. The molecular electrostatic potential (MEP) mappings of the curcuminoid ligands, which were plotted using the GaussView software, are illustrated in Figure 3-3. The electrostatic potentials of molecules correlate with the dipole moments, electronegativities, partial charges, and chemically active sites of molecules.[20] Therefore, MEP mappings provide a visual method for evaluating the relative polarity of molecules. The O atoms of the βDiK moieties of all the curcuminoids presented negative electrostatic potentials (red areas, Figure 3-3). However, in the presence of substituents on the phenyl rings, the peripheral

substituents were positively charged (blue areas, Figure 3-3), causing the electron densities on the O atoms of the βDiK moieties to decrease. The high charge density on the βDiK moieties can account for proton dissociation, enabling the good coordination of the curcuminoids with metal ions.

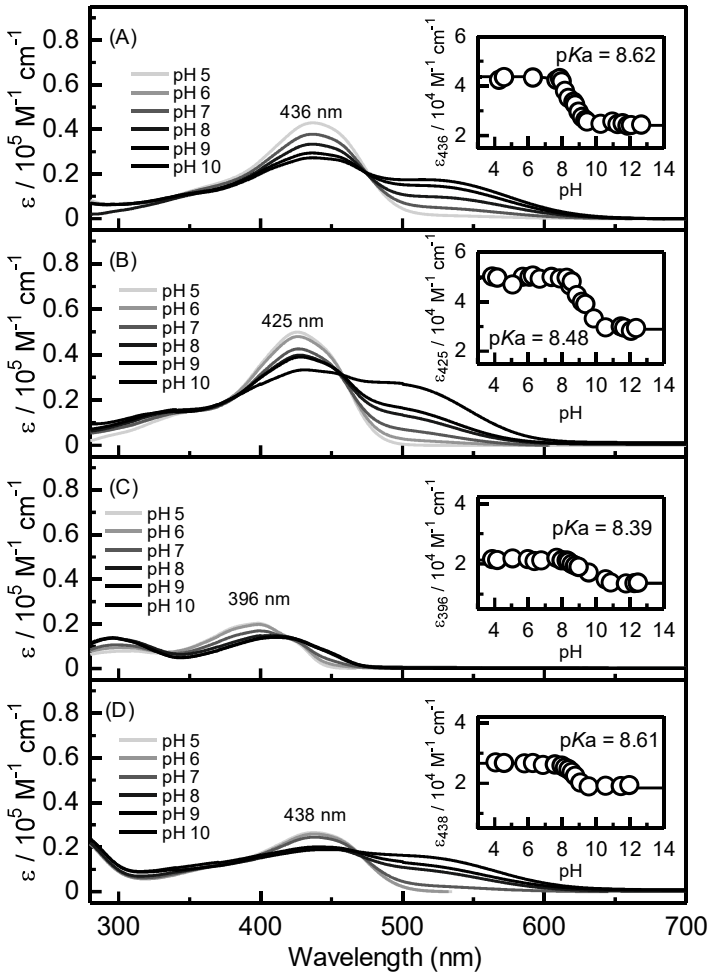

Figure 3-1. UV–vis absorption spectra of (A) curc{Ph(OH)(OMe)}$_2$, (B) curc{Ph(OH)}$_2$, (C) curc{Ph}$_2$, and (D) curc{Ph(OH)$_2$}$_2$ in DMSO–water solutions at several pH values. [βDiK] = 1.0×10^{-5} M, [Na_2SO_4] = 1.0×10^{-2} M. The molar extinction coefficients of the βDiK moieties at several pH values are illustrated in the insets.

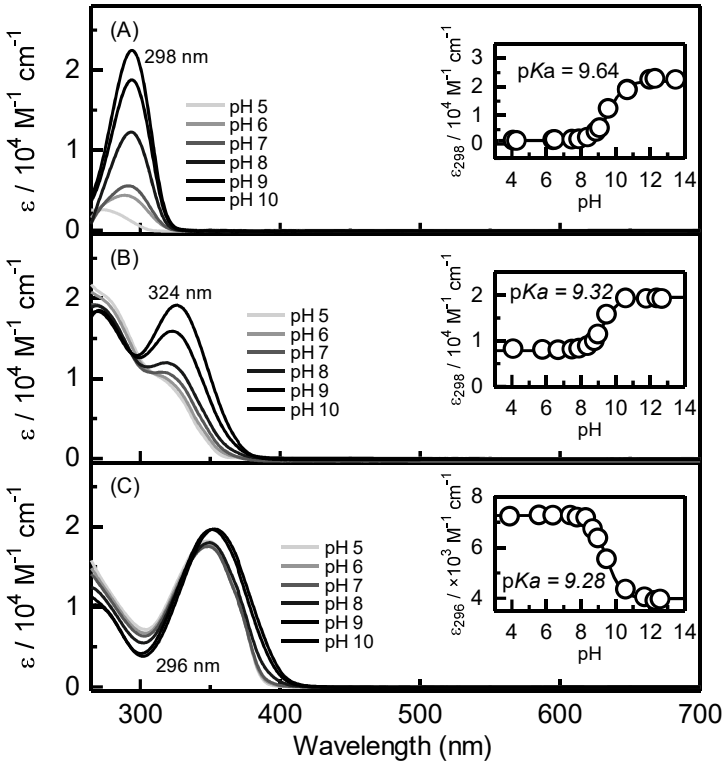

Figure 3-2. UV–vis absorption spectra of (A) acac, (B) acac{Ph}, and (C) acac{Ph}$_2$ in DMSO–water solutions at several pH values. [βDiK] = 1.0×10^{-5} M, [Na_2SO_4] = 1.0×10^{-2} M. The molar extinction coefficients of the βDiK moieties at several pH values are presented in the insets.

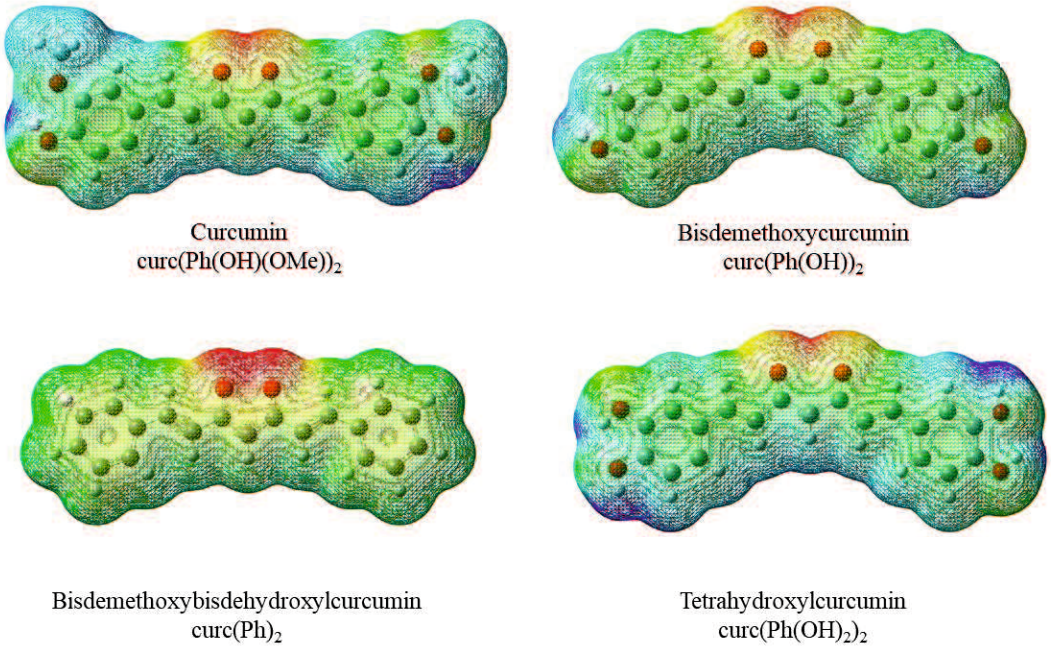

Figure 3-3. Molecular electrostatic potential mappings of the isodensities of the curcuminoids used in this study.

Table 3-2. Calculated numbers of ligands (n) and stability constants (K_{cpx}) of the copper(II) complexes and proton dissociation constants (K_a) of the ligands.

Ligand	Number of ligand n [a]	Stability constant K_{cpx} [a] [(mol dm^{-3})$^{-2}$]	Proton dissociation constant K_a [b] [mol dm^{-3}]
curc{Ph(OH)(OMe)}$_2$		$(2.6 \pm 0.1) \times 10^4$	$(4.1 \pm 0.1) \times 10^8$
curc{Ph(OH)$_2$}$_2$		$(2.9 \pm 0.1) \times 10^4$	$(4.0 \pm 0.1) \times 10^8$
curc{Ph(OH)}$_2$		$(5.3 \pm 0.1) \times 10^4$	$(3.0 \pm 0.1) \times 10^8$
curc{Ph}$_2$	2	$(6.4 \pm 0.1) \times 10^4$	$(2.5 \pm 0.1) \times 10^8$
acac		$(1.3 \pm 0.1) \times 10^4$	$(4.3 \pm 0.1) \times 10^9$
acac{Ph}		$(1.6 \pm 0.2) \times 10^4$	$(2.1 \pm 0.2) \times 10^9$
acac{Ph}$_2$		$(1.8 \pm 0.1) \times 10^4$	$(1.9 \pm 0.1) \times 10^9$

[a] determined using UV–vis spectroscopic titration

[b] in DMSO–Milli-Q water solutions

Stability of the βDiK ligands at different Cu^{2+} ion concentrations

The interactions of the βDiK ligands with Cu^{2+} ions in methanolic solutions were studied using UV–vis spectroscopy. The typical changes in the UV–vis spectra of the curcuminoids in methanolic solution with increasing concentration of Cu^{2+} ions are illustrated in Figure 3-4. In methanolic solutions, the KE tautomers, which exhibited a λ_{max} of approximately 400-430 nm depending on the substituents on the phenyl rings, prevailed for all the tested curcuminoids.[21] The addition of Cu^{2+} ions to the curcuminoid methanolic solutions led to significant changes in the UV–vis spectra of the solutions. A decrease in the absorbance at λ_{max} was observed; moreover, a new shoulder band at approximately 440-500 nm, which was ascribed to a ligand-to-metal charge-transfer reaction, emerged, and its intensity increased (Figure 3-4).[21] The isosbestic points were distinctly observed in the tested wavelength region, indicating that the spectral changes were ascribed to the initial and final species, and the side reactions did not affect the spectra. Similar spectral changes were observed for the acacs (Figure 3-5). To determine the stability constants (K_{cpx}) of the $Cu(II)(\beta DiK)_n$ complexes, $\log([Cu(II)(\beta DiK)_n]/[Cu^{2+}])$ was plotted as a function of log [βDiK] using the following equations:

$$Cu^{2+} + n\beta DiK \overset{K_{cpx}}{\rightleftharpoons} Cu(II)(\beta DiK)_2$$

$$K_{cpx} = \frac{[Cu(II)(\beta DiK)_n]}{[Cu^{2+}][\beta DiK]^n}, \quad \text{..... (3.4)}$$

$$\log\left(\frac{\left[Cu(II)\left(\beta DiK\right)_n\right]}{\left[Cu^{2+}\right]}\right) = n \log\left[\beta DiK\right] + \log K_{cpx}, \quad \text{..... (3.5)}$$

where $[Cu^{2+}]$, [βDiK], and $[Cu(II)(\beta DiK)_n]$ are the equilibrium concentrations of the Cu^{2+} ions, βDiK ligands, and $Cu(II)(\beta DiK)_n$ complexes, respectively, and n is the number of ligands coordinated with Cu^{2+} ions. The K_{cpx} and n values of the $Cu(II)(\beta DiK)_2$ complexes

were calculated using the least-squares curve fitting in Figure 3-4(B), and the results are summarized in Table 3-2. The stoichiometric analysis of the experimental data using Eq. (3.5) suggested the formation of Cu(II)(βDiK)$_2$ complexes with a βDiK ligand:Cu^{2+} ion molar ratio of 2:1 for the all tested systems. The K_{cpx} values of the Cu(II)(βDiK)$_2$ complexes decreased as follows: acac < acac{Ph} < acac{Ph}$_2$ < curc{Ph(OH)(OMe)}$_2$ < curc{Ph(OH)$_2$}$_2$ < curc{Ph(OH)}$_2$ < curc{Ph}$_2$. The logK_{cpx} vs. the acid dissociation constant (pK_a) plots of the ligands are presented in Figure 3-5. The logK_{cpx} values varied linearly with the pK_a values; therefore, the βDiK moieties with lower pK_a values can easily form stable Cu(II)(βDiK)$_2$ complexes. These results indicate that the Cu^{2+} ions presented significant affinity for the ligands capable of easily deprotonating the KE tautomers. Furthermore, the different substituents on the phenyl rings of the curcuminoids affected the chelating ability of the curcuminoids with Cu^{2+} ions. As predicted using theoretical calculations, the charge densities on the βDiK moieties increased with decreasing number of electron-donating substituents, such as hydroxyl and methoxy groups, on the phenyl rings. It was expected that the negatively charged O atoms easily reacted with the Cu^{2+} cations, leading to the formation of highly stable Cu(II)(βDiK)$_2$ complexes. Next, we focused on the Cu(II)/curc{Ph}$_2$ and Cu(II)/acac{Ph}$_2$ binary systems with different lengths of the unsaturated alkyl chains connected to the βDiK moieties. According to the data in Table 3-2, curc{Ph}$_2$ can form a more stable complex with Cu^{2+} ions than acac{Ph}$_2$. The absence of electron-donating substituents on the phenyl rings of curcumin or the π-conjugated structures of the βDiK moieties were insufficient to provide good chelating ability with Cu^{2+} ions; therefore, both should be present to promote the formation of stable complexes.

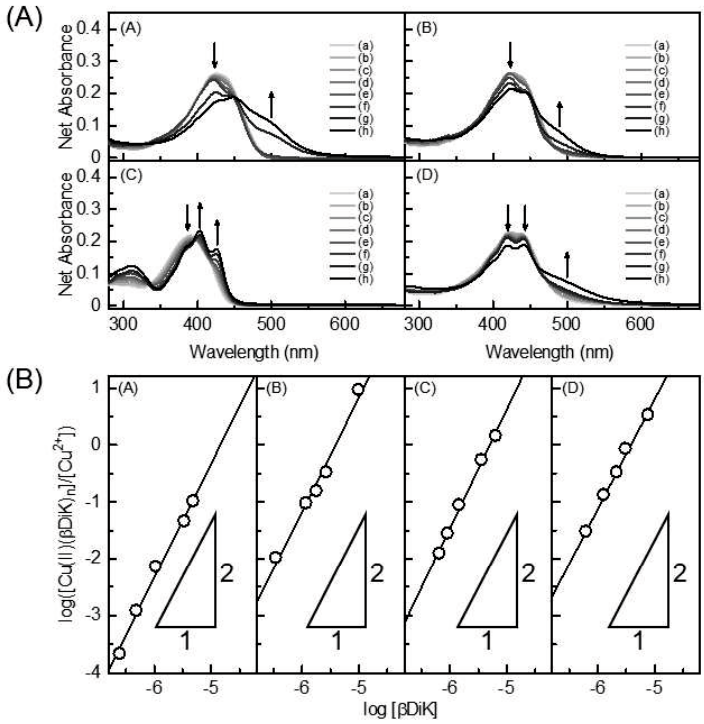

Figure 3-4. (A) Changes in the UV–vis absorption spectra of (A) curc{Ph(OH)(OMe)}$_2$, (B) curc{Ph(OH)}$_2$, (C) curc{Ph}$_2$, and (D) curc{Ph(OH)$_2$}$_2$ methanolic solutions with the concentration of added Cu^{2+} ions. [βDiK] = 5.0×10^{-6} mol dm^{-3}; [Cu^{2+}]/[βDiK] ratios of: (a) 0, (b) 0.1, (c) 0.2, (d) 0.5, (e) 1, (f) 1.5, (g) 2, and (h) 5. The arrows indicate the directions of the changes in absorbance with increasing Cu^{2+} ion concentration. (B) Dependence of log([Cu(II)(βDiK)$_2$]/[Cu^{2+}]) on log[βDiK] for (A) curc{Ph(OH)(OMe)}$_2$, (B) curc{Ph(OH)}$_2$, (C) curc{Ph}$_2$, and (D) curc{Ph(OH)$_2$}$_2$ in methanolic systems. The solid lines were obtained using Eq. (3.5).

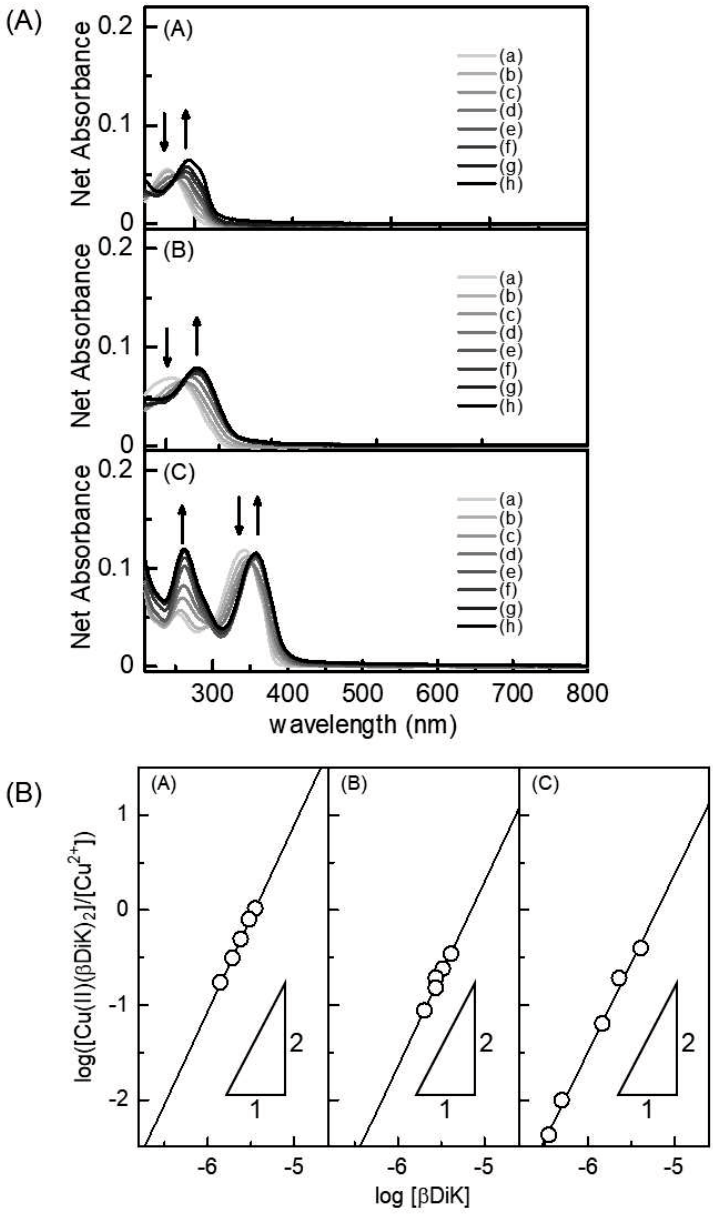

Figure 3-5. (A) Changes in the UV–vis absorption spectra of (A) acac, (B) acac{Ph}, and (C) acac{Ph}$_2$ methanolic solution with the concentration of added Cu^{2+} ions. [βDiK] = 5.0×10^{-6} mol dm^{-3}; [Cu^{2+}]/[βDiK] ratios of (a) 0, (b) 0.1, (c) 0.2, (d) 0.5, (e) 1, (f) 1.5, (g) 2, and (h) 5. The arrows indicate the directions of the changes in absorbance with increasing Cu^{2+} ion concentration. (B) Dependence of log([Cu(II)(βDiK)$_2$]/[Cu^{2+}]) on log[βDiK] for (A) acac, (B) acac{Ph}, and (C) acac{Ph}$_2$ in methanolic systems. The solid lines were obtained using Eq. (3.5).

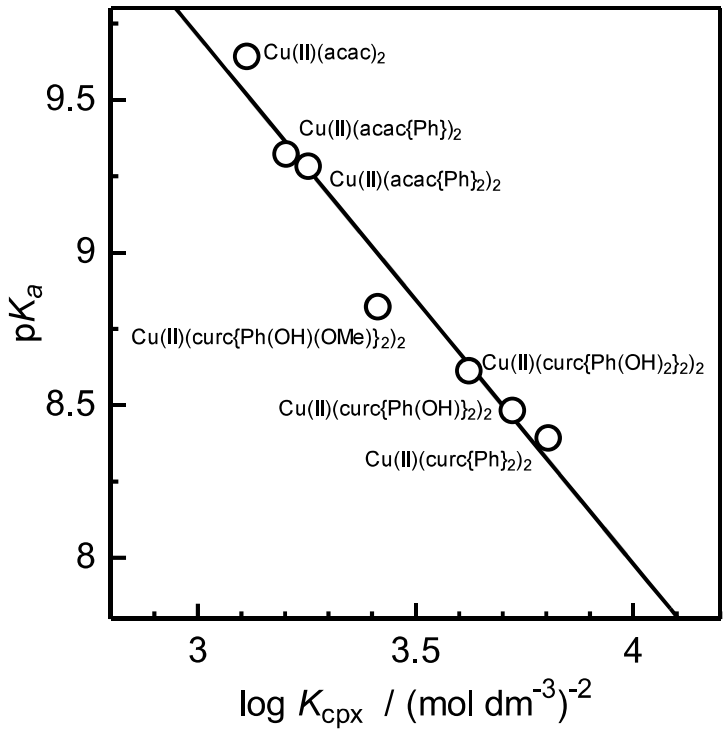

Figure 3-6. Dependence of the logK_{cpx} values of the Cu(II)(βDiK)$_2$ complexes on the pK_a values of the corresponding βDiK ligands.

Water-crosslinking reaction of EPR-*g*-MTMS resins containing Cu(II)(βDiK)$_2$ complexes

The typical ATR–FTIR spectra of the EPR-*g*-MTMS system containing Cu(II)(curc{Ph(OH)(OMe)}$_2$)$_2$ that underwent water-crosslinking are presented in Figure 3-7. Similar spectral changes were observed for the EPR-*g*-MTMS system containing the other Cu(II)(βDiK)$_2$ complexes. The peaks at 1095 and 1193 cm^{-1} in the initial spectra are the characteristic absorption peaks ascribed to the Si–O and Si–C stretching vibration of the methoxysilane groups (–Si–OCH$_3$) of MTMS.[22] The intensities of peaks decreased gradually with aging time until the peaks disappeared. Concurrently, new absorption bands at 1045 and 1120 cm^{-1} emerged, and their intensities increased with aging time. According to several FTIR studies of silicon compounds,[23,24] these peaks were assigned to –Si–O–Si– and multi-siloxane linkages (–Si=(O)$_2$=Si– or –Si≡(O)$_3$≡Si–), respectively. These results indicate that the degree of water-crosslinking (hydrolysis and condensation) of the EPR-*g*-MTMS systems containing the evaluated Cu(II)(βDiK)$_2$ complexes can be directly monitored using ATR–FTIR spectroscopy. The reaction sequence for the silane–water-crosslinking reaction in polymer systems is presented in Scheme 3-5. During alkoxysilane hydrolysis, the alkoxy groups on the Si atoms are replaced by hydroxyl groups; however, replacement does not occur simultaneously on all the alkoxy units. Since the peaks at approximately 900 and 3700 cm^{-1}, which are typically assigned to Si–OH, were not observed in this study, we inferred that Si–OH was consumed immediately in the condensation reaction. Consequently, we concluded that the condensation rate was significantly higher than the hydrolysis rate.

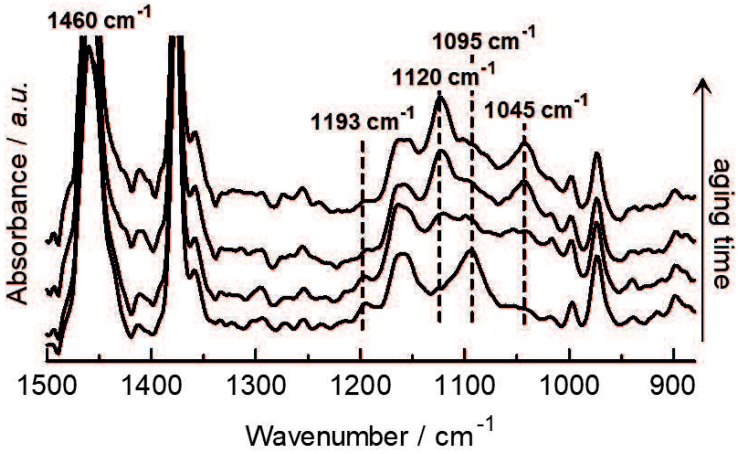

Figure 3-7. Changes induced by water-crosslinking in the ATR–FTIR spectra of EPR-*g*-MTMS in the presence of the Cu(II)(curc{Ph(OH)(OMe)}$_2$)$_2$ complex (5.0×10^{-4} mol/100 g EPR resin) at 80 °C. The peak assignments are summarized in the text.

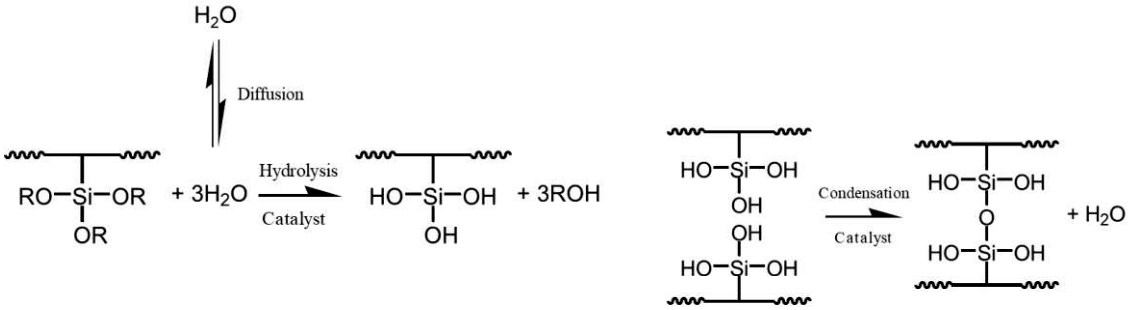

Scheme 3-7. Water-crosslinking reaction pathway in silane-grafted polyolefin system

Kinetics of the hydrolysis reaction in the EPR-*g*-MTMS systems containing various Cu(II)(βDiK)$_2$ complexes

In this study, the kinetics of the hydrolysis of EPR-*g*-MTMS was studied using the A_{1095}/A_{1460} ratio. The time evolution of the A_{1095}/A_{1460} ratio during the hydrolysis in the EPR-*g*-MTMS system containing various copper(II) curcuminoid complexes at 30, 50, and 80 °C is presented in Figure 3-8. The initial hydrolysis rate (r^0_{hyd} (h^{-1})), which was calculated using Eq. (3.6), was obtained by differentiating the quadratic equation used to fit the experimental data in Figure 3-8, as follows:

$$r^0_{hyd} = \left| \frac{d\left(A_{1095} / A_{1460}\right)}{dt} \right|_{t=0} . \quad \text{..... (3.6)}$$

The r^0_{hyd} values calculated using Eq. (3.6) increased linearly with increasing the concentration of –Si–OCH_3 groups (Figure 3-9).[25] Therefore, we concluded that the hydrolysis step was primarily controlled by the hydrolysis rate, and the effect of the rate of water diffusion on this step was negligible. In this study, r^0_{hyd} was calculated as follows:

$$r^0_{hyd} = k_{hyd}[\text{MTMS}], \quad \text{..... (3.7)}$$

where k_{hyd} is the hydrolysis reaction rate constant and [MTMS] is the concentration of MTMS. At the beginning of the hydrolysis reaction, the MTMS concentration was approximately constant, and Eq. (3.8) was obtained after taking logarithm of Eq. (3.7), as follows:

$$r^0_{hyd} = A'_{hyd} \exp\left(\frac{-E_{a,hyd}}{RT}\right), \quad \text{..... (3.8)}$$

where A'_{hyd} is the empirical constant comprising the frequency factors A and [MTMS], and $E_{a,hyd}$ is the activation energy of the hydrolysis step. The relationship between $\ln r^0_{hyd}$ and the reciprocal of the aging temperature ($1/T$) was linear (Figure 3-10). The $E_{a,hyd}$ values for the Cu(II)(βDiK)$_2$ complexes were calculated from the slopes of the $\ln r^0_{hyd}$ vs.

1/*T* curves, and the results are summarized in Table 3-3. The obtained $E_{a,hyd}$ values for all the tested complexes were significantly smaller than that of the EPR-*g*-MTMS system in the absence of catalysts, suggesting that the Cu(II)(βDiK)$_2$ complexes promoted the hydrolysis of EPR-*g*-MTMS. The ATR–FTIR spectra acquired during the hydrolysis of EPR-*g*-MTMS containing various Cu(II)(βDiK)$_2$ complexes were similar; however, the $E_{a,hyd}$ values of the Cu(II)(βDiK)$_2$complexes increased as follows: Cu(II)(acac)$_2$ > Cu(II)(acac{Ph})$_2$ > Cu(II)(acac{Ph}$_2$)$_2$ > Cu(II)(curc{Ph(OH)(OMe)}$_2$)$_2$ > Cu(II)(curc{Ph(OH)$_2$}$_2$)$_2$ > Cu(II)(curc{Ph(OH)}$_2$)$_2$ > Cu(II)(curc{Ph}$_2$)$_2$. Although it is not possible to identify the catalytic active sites of the Cu(II)(βDiK)$_2$ complexes, we confirmed that the curcuminoids and acacs were ineffective catalysts for the hydrolysis of EPR-*g*-MTMS. These results suggest that the Lewis acid Cu sites of the Cu(II)(βDiK)$_2$ complexes served as the catalytic active sites for the hydrolysis in the EPR-*g*-MTMS system. Furthermore, since the K_{cpx} values of the Cu(II)(βDiK)$_2$ complexes depended on the βDiK ligands, we hypothesized that the difference in catalytic activity between the Cu(II)(βDiK)$_2$ complexes was ascribed to the stability of the complexes in the EPR-*g*-MTMS system.

Moreover, we determined the M_c values to evaluate the kinetics of the overall water-crosslinking reaction, which caused the formation of network structures through siloxane bonding (–Si–O–Si–). The M_c value is the primary parameter affecting the properties and determining the behavior of different types of crosslinked polymers. The M_c values of the EPR-*g*-MTMS system aged in 80 °C water (saturated reactant) for 24 h were calculated using the Flory–Rehner equation (Eq. (3.1)), and the results are summarized in Table 3-3. The M_c values decreased as follows: Cu(II)(acac)$_2$ > Cu(II)(acac{Ph})$_2$ > Cu(II)(acac{Ph}$_2$)$_2$ > Cu(II)(curc{Ph(OH)(Ome)}$_2$)$_2$ >

Cu(II)(curc{Ph(OH)$_2$}$_2$)$_2$ > Cu(II)(curc{Ph(OH)}$_2$)$_2$ > Cu(II)(curc{Ph}$_2$)$_2$, which matched the trend in the $E_{a,hyd}$ values. These results also demonstrated that the internal network structure of the water-crosslinked EPR-*g*-MTMS depended upon the catalyst used for the hydrolysis reaction.

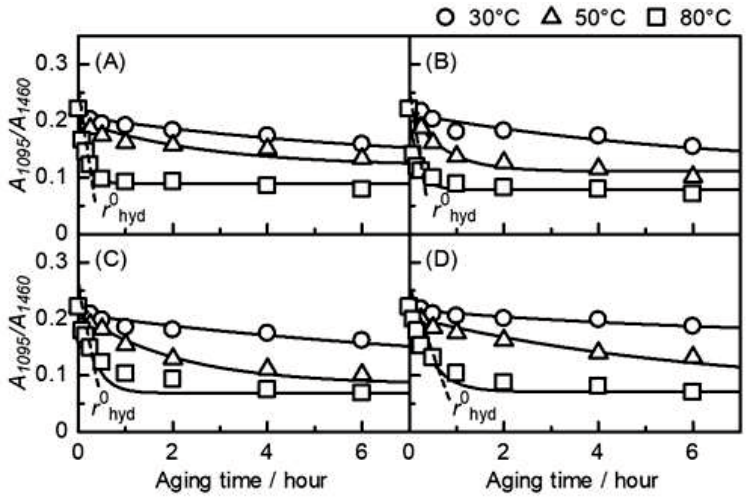

Figure 3-8. Time evolution of the A_{1095}/A_{1460} ratio of the water-crosslinked EPR-*g*-MTMS system in the presence of the (A) Cu(II)(curc{Ph(OH)(Ome)}$_2$)$_2$, (B) Cu(II)(curc{Ph(OH)}$_2$)$_2$, (C) Cu(II)(curc{Ph}$_2$)$_2$, and (D) Cu(II)(curc{Ph(OH)$_2$}$_2$)$_2$ complexes at 30 (open circle), 50 (open triangle), and 80 °C (open square).

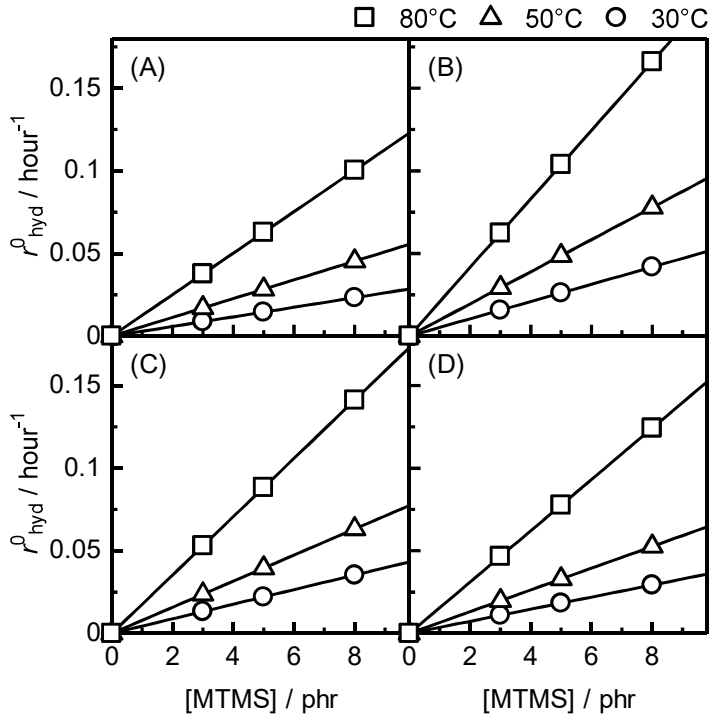

Figure 3-9. Dependence of the MTMS concentration on r^0_{hyd} for the EPR-*g*-MTMS system in the presence of the (A) Cu(II)(curc{Ph(OH)(Ome)}$_2$)$_2$, (B) Cu(II)(curc{Ph(OH)}$_2$)$_2$, (C) Cu(II)(curc{Ph}$_2$)$_2$, and (D) Cu(II)(curc{Ph(OH)$_2$}$_2$)$_2$ complexes at 30 (open circle), 50 (open triangle), and 80 °C (open square).

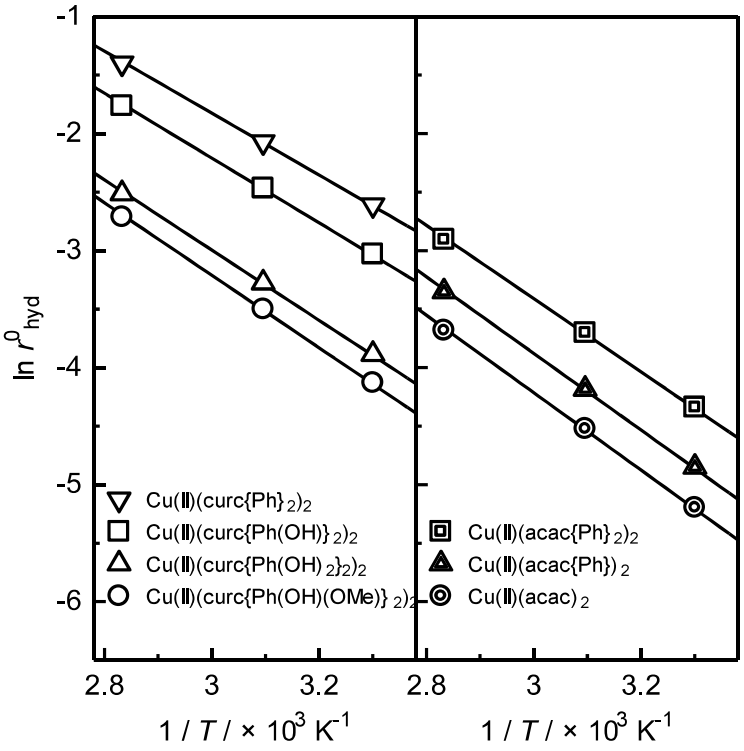

Figure 3-10. Dependence of $\ln r^0_{hyd}$ on the reciprocal absolute temperature for the EPR-*g*-MTMS system containing various Cu(II)(βDiK)$_2$ complexes. The solid lines were obtained using Eq. (3.8).

Table 3-3. Calculated activation energies for the hydrolysis reaction of EPR-*g*-MTMS ($E_{a,hyd}$) and average molecular weight between crosslinks (M_c) of the corresponding water-crosslinked EPR-*g*-MTMS system.

Catalyst [a]	Activation Energy $E_{a,\,hyd}$ [b] [kJ mol^{-1}]	Average molecular weight between crosslinks M_c [c] [g mol^{-1}]
Cu(II)(curc{Ph(OH)(OMe)}$_2$)$_2$	25.8 ± 0.5	(3.3 ± 0.1) × 10^4
Cu(II)(curc{Ph(OH)$_2$}$_2$)$_2$	24.9 ± 0.3	(3.8 ± 0.3) × 10^4
Cu(II)(curc{Ph(OH)}$_2$)$_2$	23.0 ± 1.0	(3.1 ± 0.2) × 10^4
Cu(II)(curc{Ph}$_2$)$_2$	21.9 ± 0.2	(2.0 ± 0.2) × 10^4
Cu(II)(acac)$_2$	27.5 ± 0.2	(5.0 ± 0.1) × 10^4
Cu(II)(acac{Ph})$_2$	27.2 ± 0.1	(4.8 ± 0.1) × 10^4
Cu(II)(acac{Ph}$_2$)$_2$	26.0 ± 0.2	(4.0 ± 0.1) × 10^4
without catalyst	46.9 ± 0.9	---

[a] catalyst concentration: 5.0 × 10^{-4} mol/100 g EPR

[b] determined using ATR–FTIR spectroscopy

[c] aged in 80 °C water for 24 h

Theoretical calculations for the hydration of the Cu(II)(βDiK)$_2$ complexes

We used the results of the aforementioned UV–vis spectroscopic titrations and the kinetics analysis of the hydrolysis reaction in the EPR-*g*-MTMS system to evaluate the differences in catalytic activity between Cu(II)(βDiK)$_2$ complexes. The dependence of the $E_{a,hyd}$ values of the EPR-*g*-MTMS systems containing Cu(II)(βDiK)$_2$ complexes on the K_{cpx} values of the corresponding complexes is illustrated in Figure 3-11. The good linear correlation between the $E_{a,hyd}$ and K_{cpx} values indicates that the highly stable Cu(II)(βDiK)$_2$ complexes served as remarkable catalysts for water-crosslinking in the EPR-*g*-MTMS systems. The critical aspect in elucidating the cause of the differences in catalytic activities was that the stabilities and catalytic performances of the Cu(II)(βDiK)$_2$ complexes depended on the βDiK ligands. Previous studies suggested that planar metal β-diketonate complexes can form hydrates in aqueous solution by coordinating with water molecules in their axial position.[26,27] Axially coordinated water molecules presented different bias charges depending on their distance to the central metal ions. Hence, in the EPR-*g*-MTMS systems, the axially coordinated water of the Cu(II)(βDiK)$_2$ complexes can serve as effective reaction trigger with a bias charge. Moreover, in a previous study,[2] we investigated the catalytic effect of metals on the silane–water-crosslinking reaction in a vinyltrimethoxysilane-grafted EPR copolymer system, which is similar to the EPR-*g*-MTMS system, using seven divalent acetylacetonate complexes. The results of the study indicated that the activation energy of the hydrolysis step of the metal-catalyzed silane–water-crosslinking reaction depended on the water-exchange rate constants of the metal ions. These findings suggested that the pathway for the silane–water-crosslinking reaction catalyzed by divalent metal complexes was similar to that for the water-exchange reaction of the metal ions in aqueous systems. Consequently, concerning the catalytic mechanism

of the Cu(II)(βDiK)$_2$ complexes in the EPR-*g*-MTMS system, we concluded that a free water molecule axially coordinated with the central metal ion of the complex during a rapid first step, and then hydrolysis occurred via the displacement of a methoxide group on the Si atom of the alkoxysilane group during the water-exchange reaction of the metal ion. In the 1960s, Eigen and Wilkins studied the kinetics of the water-exchange reaction in aqueous systems.[23] According to the Eigen mechanism principles, the reaction rate at which water molecules are exchanged between the first coordination sphere of a metal ion and the bulk free water is of primary importance in the kinetics of complex formation. For divalent 3d metals, such as Cu(II), Zn(II), and Co(II), the changes in the water-exchange rate are primarily induced by variations in the electronic occupancy of the d orbitals of the metals. Particularly, copper(II) complexes present the so-called Jahn–Teller distortion owing to the d^9 electronic configuration of the Cu^{2+} ions, leading to atypically high water-exchange rates.[29,30] In addition, the decrease in the electron density around the central metal ions that serve as water coordination sites in complexes, can accelerate the water-exchange reaction of the coordination water in metal complexes.[31] This promotes the removal of the coordinated water molecules via a dissociation process, which is the most common mechanism responsible for the water-exchange reaction in metal complexes.

DFT calculations were performed to gain insight into the water-exchange reactions of the Cu(II)(βDiK)$_2$ complexes with different βDiK ligands. The most stable optimized structure of the Cu(II)(curc{Ph}$_2$)$_2$ complex and its hydrate are presented in Figure 3-12. For all the Cu(II)(βDiK)$_2$ complexes subjected to DFT calculations, the octahedral coordination environment of Cu(II) was achieved using the two water molecules axially coordinated with the Cu(II)(βDiK)$_2$ complexes, as suggested by

Mattia[32] et al. The Cu–H_2O(axial) distances of the Cu(II)(βDiK)$_2$ hydrate complexes provide insight into the difference in stability between the coordinated water molecules in the complexes. The Cu–H_2O(axial) distances increased as follows: Cu(II)(acac)$_2$ < Cu(II)(acac{Ph})$_2$ < Cu(II)(acac{Ph}$_2$)$_2$ < Cu(II)(curc{Ph(OH)(OMe)}$_2$)$_2$ < Cu(II)(curc{Ph(OH)$_2$}$_2$)$_2$ < Cu(II)(curc{Ph(OH)}$_2$)$_2$ < Cu(II)(curc{Ph}$_2$)$_2$ (Table 3-4). These results indicate that the bonds between the axially coordinated water molecules and Cu^{2+} ions in the Cu(II)(curc{Ph}$_2$)$_2$ complex were stronger than those in the other Cu(II)(βDiK)$_2$ complexes. The elongation of the bonds between the axially coordinated water molecules and Cu^{2+} ions led to atypically high water-exchange reaction rates. The strength of the Cu–H_2O(axial) bonds was further investigated by calculating the dissociation energies of the axially coordinated water molecules (Δ*E*). According to Carlos et al.,[33] Δ*E* decreased with increasing water-exchange reaction rate. Typically, Δ*E* can be calculated as follows:

$$\Delta E = TE_{hyd} - TE_s \quad , \text{..... (3.9)}$$

Where TE_s is the sum of the total energy of the complex and two water molecules and TE_{hyd} is the total energy of the corresponding hydrate complex. The calculated Δ*E* values are listed in Table 3-4. Typically, the rates of the water-exchange reactions catalyzed by Jahn–Teller ions, such as Cu^{2+} [d^9] and Cr^{2+} [d^4] ions, are high, because the water molecules in the metal coordination sphere are loosely bound and can be easily lost via a dissociative interchange mechanism. Therefore, the water-exchange rates are significantly influenced by the coordinated ligands of the metal ions. The Δ*E* values confirmed the dependence of the water-exchange reaction rates on the βDiK ligands of the Cu(II)(βDiK)$_2$ complexes, and the trend in Δ*E* values matched the kinetic data for the hydrolysis reactions in the EPR-*g*-MTMS systems containing various Cu(II)(βDiK)$_2$

complexes. This behavior was attributed to the electron-withdrawing groups of the βDiK ligands. The metal-chelating abilities of the βDiK ligands primarily depended on the electron densities on the βDiK moieties, which were affected by the electronic effects of the substituents in the ligands.[34] Moreover, the electron-withdrawing phenyl rings and extended π-conjugation structures in curcuminoids can promote inductive and resonance effects. Therefore, electron-withdrawing curcuminoid ligands can shift the electron density away from the central metal ion, leading to a decrease in the water dissociation energy of the Cu–H_2O(axial) bonds. In addition, as the substituents on the phenyl rings of the curcuminoids were in a conjugated position, the electron-withdrawing properties of the phenyl rings slightly depended on the character of the substituents.[35] DFT calculations cannot directly describe the water-crosslinking reactions in the EPR-*g*-MTMS systems. However, our experimental and theoretical results indicate that the electron-withdrawing groups of the βDiK ligands can significantly enhance the catalytic activity of Cu^{2+} ions, as demonstrated by the high water-exchange reaction rates. Therefore, we believe that our findings will be of considerable interest to polymer chemistry researchers.

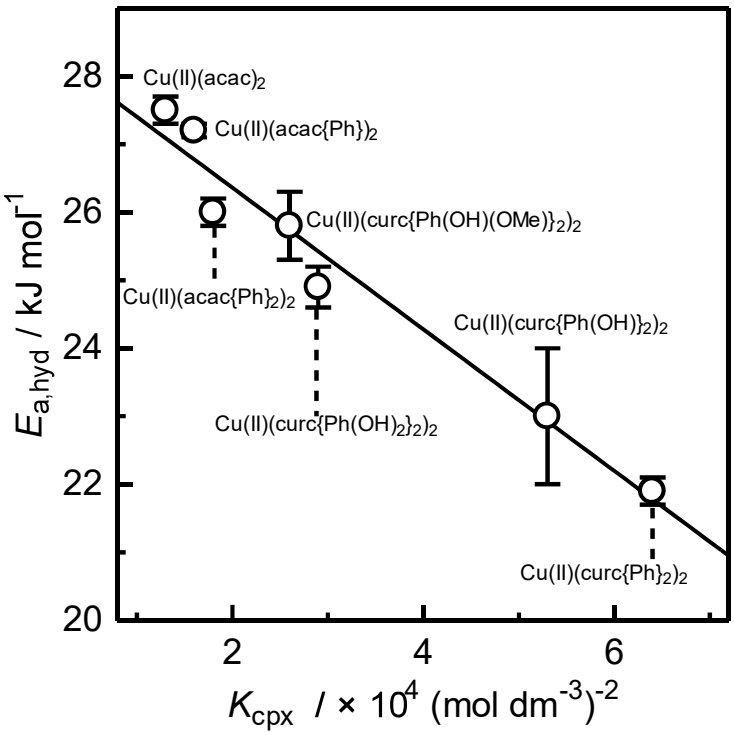

Figure 3-11. Dependence of the hydrolysis activation energies of the EPR-*g*-MTMS systems containing various Cu(II)(βDiK)$_2$ complexes on the stability constants of the corresponding complexes.

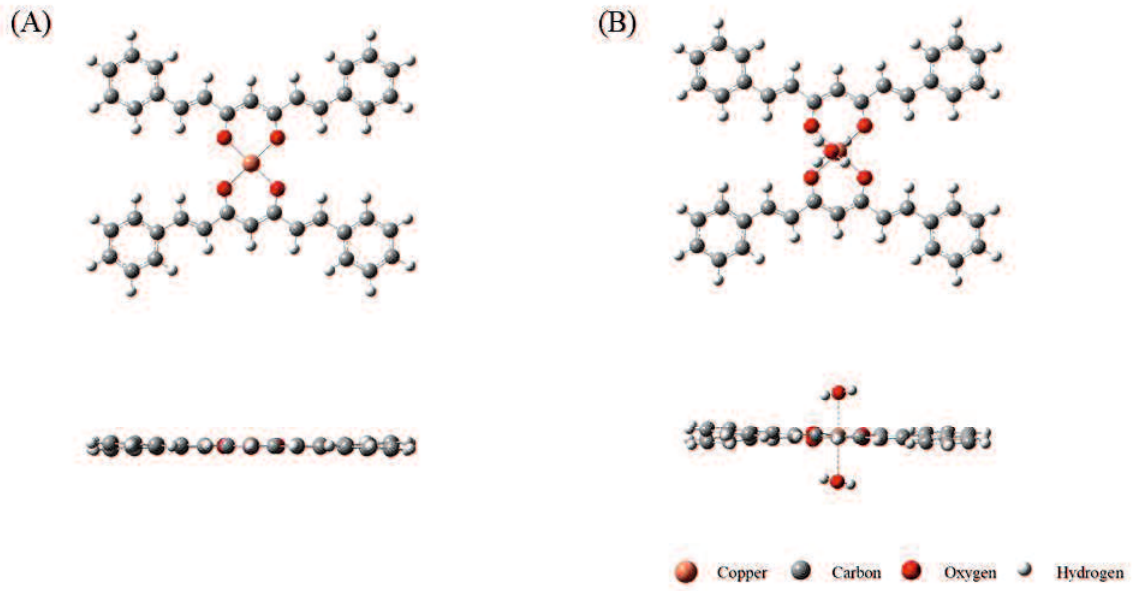

Figure 3-12. Final optimized structures of the (A) Cu(curc{Ph}$_2$)$_2$ and (B) Cu(curc{Ph}$_2$)$_2$ hydrate complexes.

Table 3-4. Calculated water dissociation energy (ΔE) values and Cu–H_2O(axial) distances of the Cu(II)(βDiK)$_2$ hydrate complexes.

Catalyst	Water dissociation energy ΔE [10^6 kJ mol^{-1}]	Cu-H_2O(axial) [Å]
Cu(II)(curc{Ph(OH)(OMe)}$_2$)$_2$	1.8 ± 0.1	3.31
Cu(II)(curc{Ph(OH)$_2$}$_2$)$_2$	1.6 ± 0.1	3.37
Cu(II)(curc{Ph(OH)}$_2$)$_2$	1.5 ± 0.1	3.42
Cu(II)(curc{Ph}$_2$)$_2$	1.3 ± 0.1	3.58
Cu(II)(acac)$_2$	2.6 ± 0.1	2.49
Cu(II)(acac{Ph})$_2$	2.2 ± 0.2	2.55
Cu(II)(acac{Ph}$_2$)$_2$	2.0 ± 0.1	2.63

Conclusion

The effect of the chelating ability of the βDiK ligands with Cu^{2+} ions on the catalytic performance of the Cu(II)(βDiK)$_2$ complexes for the silane–water-crosslinking reaction was investigated. The UV–vis spectroscopic titration data revealed that the curcuminoids, which featured βDiK moieties attached to the substituted phenyl rings and unsaturated alkyl chains, presented good chelating affinity for Cu^{2+} ions and formed stable Cu(II)(βDiK)$_2$ complexes. The results of the detailed analysis of the spectral changes suggest that the decrease in the number of electron-donating hydroxy and methoxy groups on the phenyl rings led to an increase in the K_{cpx} values of the Cu(II)(βDiK)$_2$ complexes owing to the high electron density on the βDiK moieties. Moreover, the kinetic study of the silane–water-crosslinking reaction using ATR–FTIR spectroscopy revealed that all the Cu(II)(βDiK)$_2$ complexes in this study presented high catalytic activity for the hydrolysis reaction. Furthermore, the $E_{a,hyd}$ values obtained using the Arrhenius equation demonstrated the dependence of $E_{a,hyd}$ on the βDiK ligands. The linear relationship between the $E_{a,hyd}$ and K_{cpx} values suggested that the differences in catalytic activities between the Cu(II)(βDiK)$_2$ complexes was primarily attributed to the stability of the complexes. The theoretical calculations demonstrated that curcuminoid chelation led to a decrease in the water dissociation energies of the Cu(II)(βDiK)$_2$ hydrate complexes. These results indicate that the chelating ability of the βDiK ligands with Cu^{2+} ions predominantly affected the catalytic activity of the Cu(II)(βDiK)$_2$ complexes for the silane–water-crosslinking reaction.

references

1. A. Shafir, S. L. Buchwald, *J. Am. Chem. Soc.*, **2006**, *128*, 8742-8743.
2. S. M. Krajewski, A. S. Crossman, E. S. Akturk, T. Suhrbier, S. J. Scappaticci, M. W. Staab, M. P. Marshak, *Dalton Trans.*, **2019**, *48*, 10714-10722.
3. J. H. Olivier, J. Harrowfield, R. Ziessel, *Chem. Commun.*, **2011**, *47*, 11176-11188.
4. S. Wanninger, V. Lorenz, A. Subhan, F. T. Edelmann, *Chem. Soc. Rev.*, **2015**, *44*, 4986-5002.
5. A. Kareem, M. S. Khan, S. A. A. Nami, S. A. Bhat, A. U. Mirza, N. Nishat, *J. Mol. Struct.*, **2018**, *1167*, 261-273.
6. K. Adachi, T. Hirano, K. Fukuda, K. Nakamae, *Macromol. React. Eng.*, **2007**, *1*, 313-320.
7. W. F. Chen, S. L. Deng, B. Zhou, L. Yang, Z. L. Li, *Free Radic. Biol. Med.*, **2006**, *40*, 526-535.
8. M. S. Refat, *Spectochim. Acta A*, **2013**, *105*, 326-337.
9. M. J. Frisch, G. Trucks, H. Scglegel, G. Scuseria, J. Cheeseman, G. Scalmani, V. Barone, B. Mennucci, G. Petersson, *Gaussian 09 Revision D. 01*; Gaussian Inc., Wallingford CT, USA, **2009**.
10. A. D. Mclean, C. S. Chandler, *J. Chem. Phys.*, **1980**, *72*, 5639-5648.
11. K. Adachi, K. Honda, S. Yamazaki, T. Hirano, H. Kurokawa, A. Wakabayashi, P. H. Kasai, K. Nakamae, H. Iwabuki, K. Murakami, *Polym. Eng. Sci.*, **2011**, *51*, 632-640.
12. A. F. M. Bartob, *Handbook of Solubility Parameters and Other Cohesion Parameters.* CRC Press, Boca Raton, Florida, USA, **1983**.
13. A. F. M. Bartob, *Pure Appl. Chem.*, **1985**, *57*, 905-912.

14. D. K. Singh, R. Jagannathan, P. Khandelwal, P. M. Abraham, P. Poddar, *Nanoscale*, **2013**, *5*, 1882-1893.
15. M. H. M. Leung, D. T. Pham, S. F. Lincoln, T. W. Kee, *Phys. Chem. Chem. Phys.*, **2012**, *14*, 13580-13587.
16. L. Wang, Y. Shen, X. Lai, Z. Li, M. Liu, *J. Polym. Res.*, **2011**, *18*, 469-476.
17. Q. Zhao, Q. Liu, H. Xu, Y. Bei, S. Feng, *RSC Adv.*, **2016**, *6*, 38447-38453.
18. R. M. Silverstein, G. C. Bassler, T. C. Morrill, Morrill, T.-C. *Spectrometric Identification of Organic Compounds. 5th ed.*; John Wiley & Sons Inc., New York, USA, **1991**.
19. S. Tanaka, K. Adachi, *Mater. Today Commun.*, **2019**, *21*, 100584.
20. J. C. Kenvin, M. G. White, M. B. Mitchell, *Langmuir*, **1991**, *7*, 1198-1205.
21. V. Vallet, U. Wahlgren, I. Grenthe, *J. Am. Chem. Soc.*, **2003**, *125*, 14941-14950.
22. K. Adachi, T. Hirano, *Eur. Polym. J.*, **2008**, *44*, 542-549.
23. M. Eigen, R. G. Wilkins, *Adv. Chem. Ser.*, **1965**, *49*, 55-80.
24. C. F. Schwend, B. M. Rode, *ChemPhysChem*,J **2003**, *4*, 931-943.
25. T, Hattori, T. Toraishi, T. Tsunede, S. Nagasaki, S. Tanaka, *J. Phys. Chem. A*, **2005**, *109*, 10403-10409.
26. S. Karimi, G. Hunter, L. Moriggi, C. P. Iglesias, I. Helm, *Inorg. Chem.*, **2016**, *44*, 6231-6239.
27. M. Asti, E. Ferrari, S. Croci, G. Atti, S. Rubagotti, M. Iori, P. C. Capponi, A. Zerbini, M. Saladini, A. Versari, *Inorg. Chem.*, **2014**, *53*, 4922-4933.
28. M. R. Figueroa, C. P. Iglesias, *J. Phys. Chem. A*, **2015**, *119*, 6436-6445.
29. H. Yekeler, M. Yekeler, *J. Mol. Model*, **2006**, *12*, 763-768.
30. M. M. Conradie, J. Conradie, *J. Electrochim. Acta*, **2015**, *152*, 512-519.

31. T. Hattori, T. Toraishi, T. Tsunede, S. Nagasaki, S. Tanaka, *J. Phys. Chem. A*, **2005**, *109*, 10403-10409.
32. M. Asti, E. Ferrari, S. Croci, G. Atti, S. Rubagotti, M. Iori, P. C. Capponi, A. Zerbini, M. Saladini, A. Versari, *Inorg. Chem.*, **2014**, *53*, 4922-4933.
33. S. Karimi, G. Hunter, *Inorg. Chem.*, **2016**, *44*, 6231-6239.
34. M. R. Figueroa, C. P. Iglesias, *J. Phys. Chem. A*, **2015**, *119*, 6436-6445.
35. H. Yekeler, M. Yekeler, *J. Mol. Model.*, **2006**, *12*, 763-768.

Silane–water-crosslinking of polyolefins using organophosphorus compounds as catalysts

Introduction

OTCs have been widely used as catalysts for the water-crosslinking reaction of silane-grafted polyolefins owing to their good efficiency and selectivity toward the hydrolysis and condensation reactions. However, owing to the health and environmental concerns associated with OTCs, they have been slowly replaced by more sustainable alternative catalysts. Nowadays, the shift toward "green polymers" with favorable environmental and economic outlooks requires the development of "metal-free" catalysts.

Silicate sol–gel researchers have increasingly turned their attention toward the development of organocatalysts for the hydrolysis and condensation reactions of alkoxysilanes.[1-4] Several types of the organocatalysts, including Bronsted and Lewis acid or base catalysts, have been used for metal-free sol–gel processes with practical applications in the biomedical and electronic fields. Various Lewis basic catalysts have been used for the activation of the silane sol–gel reaction. Several amine-, guanidine-, and phosphazene-based catalysts present remarkable catalytic activity for hydrolysis and condensation reactions in silane sol–gel systems (Scheme 4-1).[5-8] According to the aforecited reports, highly nucleophilic Lewis bases are required for smooth activation and generation of high-density silicate structures. The success of Lewis-base-catalyzed silicate sol–gel reactions has inspired us to use Lewis base catalysts for the water-crosslinking reaction of silane-grafted polyolefin resins and develop a convenient method

for controlling the crosslinking rate and density.

Herein, we focus on organophosphorus compounds containing P=O functional groups as potential catalysts for the water-crosslinking reaction in the EPR-*g*-MTMS system (Scheme 4-1). Because the Lewis base P=O groups serve as proton acceptors, phosphoryl compounds exhibit excellent catalytic performance for the silylation reaction of primary alcohols under mild conditions.[9-15] Inspired by the previous reports, we designed new water-crosslinking catalysts comprising highly nucleophilic Lewis base P=O moieties, which served as the catalytic activation sites, and substituents to tune the Lewis basicity of the catalyst. The catalytic performance of several organophosphorus compounds for the water-crosslinking reaction in the EPR-*g*-MTMS system was evaluated. The organophosphorus compounds analyzed in this study (i.e., phosphonic acids, phosphoric esters ($O=P(OR')_3$), phosphine oxides ($O=PR_3$), phosphine (PR_3), and polyphosphoric acid (PPA)) are illustrated in Scheme 4-2. Kinetic investigations demonstrated that the phosphoryl compounds presented excellent catalytic activity for the water-crosslinking reaction in the tested system. Additionally, a theoretical study was conducted to provide mechanistic insight on the catalytic active sites of the phosphoryl compounds.

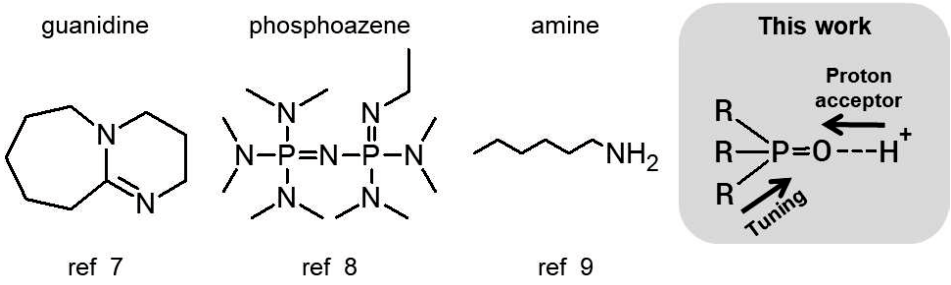

Scheme 4-1. Lewis base catalyst for silane sol–gel reactions and design concept of the Lewis base catalyst in this study.[7-9]

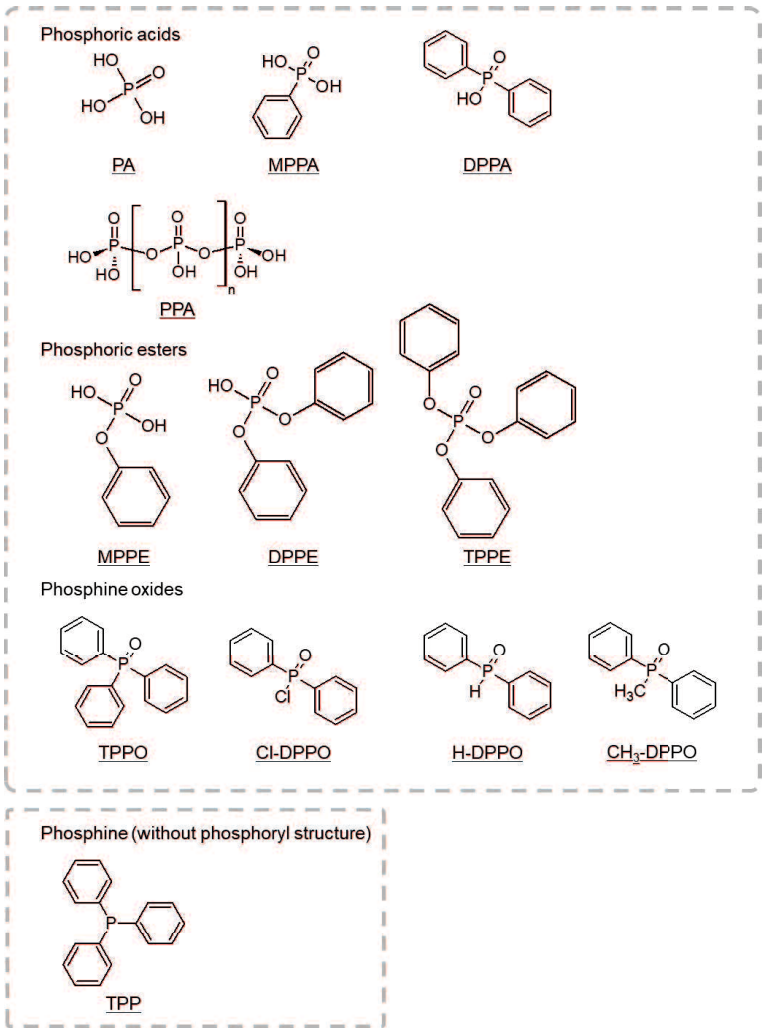

Scheme 4-2. Organophosphorus compounds used as organocatalysts for the water-crosslinking reaction in the EPR-*g*-MTMS system in this study.

Experimental

Materials

Phosphoric acid (PA; >88 % purity), monophenylphosphonic acid (MPPA; >98 % purity), diphenyl phosphinic acid (DPPA; >98 % purity), monophenyl phosphate (MPPE; >99 % purity), diphenyl phosphate (DPPE; >99 % purity), triphenyl phosphate (TPPE; >99 % purity), triphenylphosphine oxide (TPPO; >98 % purity), methyl(diphenyl)phosphine oxide (CH_3–DPPO; >98 %, purity), diphenylphosphinic chloride (Cl–DPPO; >98 % purity), diphenylphosphine oxide (H–DPPO; >98 % purity), triphenylphosphine (TPP; >95 % purity) were purchased from TCI, Tokyo, Japan. Polyphosphoric acids (PPA; 75 %P_2O_5 (PPA($P_2O_5$75)), 80 %P_2O_5 (PPA($P_2O_5$80)), 82 %P_2O_5 (PPA($P_2O_5$82)), and 84 %P_2O_5 (PPA($P_2O_5$84)) were acquired from Nacalai Tesque Inc. (Kyoto, Japan) All chemicals were used as received. Dibutyltin dilaurate (DBTL; Wako Pure Chemicals, Osaka, Japan) was used as the reference. All other materials were the same as those described in the Materials section of Chapter 3 and were used as received without further purification.

Preparation of water-crosslinked EPR-*g*-MTMS containing organophosphorus compounds

EPR-*g*-MTMS was prepared using the same method described in Chapter 3. After grafting, the organophosphorus compounds were added to the EPR-*g*-MTMS resin melted at 120 °C. The amounts of $O{=}PR_3$, $O{=}P(OR')_3$, and PR_3 added to the resin were 5.0×10^{-4} mol/100 g resin, and the amount of PPA was 0.15 parts per 100 parts of resin (phr). The resultant EPR-*g*-MTMS systems containing the water-crosslinking catalysts were shaped into ~1.0 mm thick compression-molded sheets via air pressing. The sheets were cut into identical pieces, which were placed in water baths at 30, 50, or 80 °C. The

samples were then removed from the water baths at various times to evaluate the reaction progress. To avoid undesired water crosslinking while waiting for analysis or further treatment, the samples were stored under dry conditions.

Hydrolysis and condensation of water-crosslinked EPR-*g*-MTMS

The hydrolysis reaction of the EPR-*g*-MTMS systems containing organophosphorus compounds was analyzed using the same methods described in Chapter 3.

The overall water-crosslinking reaction (hydrolysis and condensation steps) in the EPR-g-MTMS systems containing organophosphorus compounds was analyzed by determining the gel contents of the crosslinked EPR-g-MTMS samples. The gel contents of the crosslinked EPR-*g*-MTMS samples were determined by extracting the soluble fraction using a Soxhlet extractor and boiling xylene for 6 h. The gel fraction of each sample was calculated as the percentage of the dry mass of the insoluble fraction (M_d) to the initial mass (M_i) of the sample, as follows:

$$\text{gel content (\%)} = \frac{M_d}{M_i} \times 100 \quad \text{..... (4.1)}$$

Quantum chemistry calculations

All the theoretical calculations were performed using the Gaussian 09 programming package. The geometry of the phosphoryl compounds used as catalysts in this study was optimized using DFT calculations with the B3LYP functional, which was believed to be superior to the ab-initio and MP2 methods in predicting molecular properties. The 6-31 basis set was used for the C, H, P, and O atom-containing molecules for all the calculations. The DFT calculations were used to determine the molecular

structure and heat of formation of each phosphoryl compound. According to previous reports,[16,17] the conformations of the intermediates of the hydrolysis and condensation steps were built by binding the O atom of a nucleophilic complex to the Si atoms of alkoxysilane and hydroxysilane, respectively, followed by minimizing the energy using DFT calculations.

Results and discussion

Water-crosslinking reaction of the EPR-*g*-MTMS systems containing organophosphorus compounds

The typical ATR–FTIR spectra during the water-crosslinking reaction in the EPR-*g*-MTMS system over the TPPO catalyst at 80 °C and several aging times is presented in Figure 4-1(A). The absorption peaks at 1095 and 1193 cm^{-1} in the initial spectrum corresponded to the Si–O and Si–C stretching, respectively, of the –Si–OCH_3 groups of the MTMS moieties, and the intensities of these peaks decreased gradually with aging time. The intensity of the new absorption band at 890 cm^{-1} in the spectrum of the TPPO-containing EPR-*g*-MTMS system, which was attributed to the –Si–OH groups of the MTMS moieties, decreased with aging time. As the water-crosslinking reaction proceeded, the new absorbance peaks at 1048 and 1120 cm^{-1}, which correspond to the –Si–O–Si– and –Si=$(O)_2$=Si– or –Si≡$(O)_3$≡Si– linkages, respectively, emerged, and their intensities increased with aging time. These results indicate that several successive condensation steps occurred after the formation of hydrolyzed species in the EPR-*g*-MTMS system.

Two minor differences were observed between the ATR–FTIR spectra of the water-crosslinked EPR-*g*-MTMS systems containing TPPO and TPPE, as follows: (1) the intensity of the multi-siloxane linkage band at 1120 cm^{-1} in the TPPE-containing system was negligible and (2) the bands at 1007 and 1320 cm^{-1} emerged only in the spectrum of the TPPE-containing system. According to previous reports, the bands at 1007 and 1320 cm^{-1} corresponded to the stretching of the P–O–Si and P=O bonds, respectively. These differences between the ATR–FTIR spectra of the water-crosslinked EPR-*g*-MTMS resin containing phosphine oxides and phosphoric esters are critical in understanding the catalytic mechanism of organophosphorus compounds for water-crosslinking and is be

discussed below.

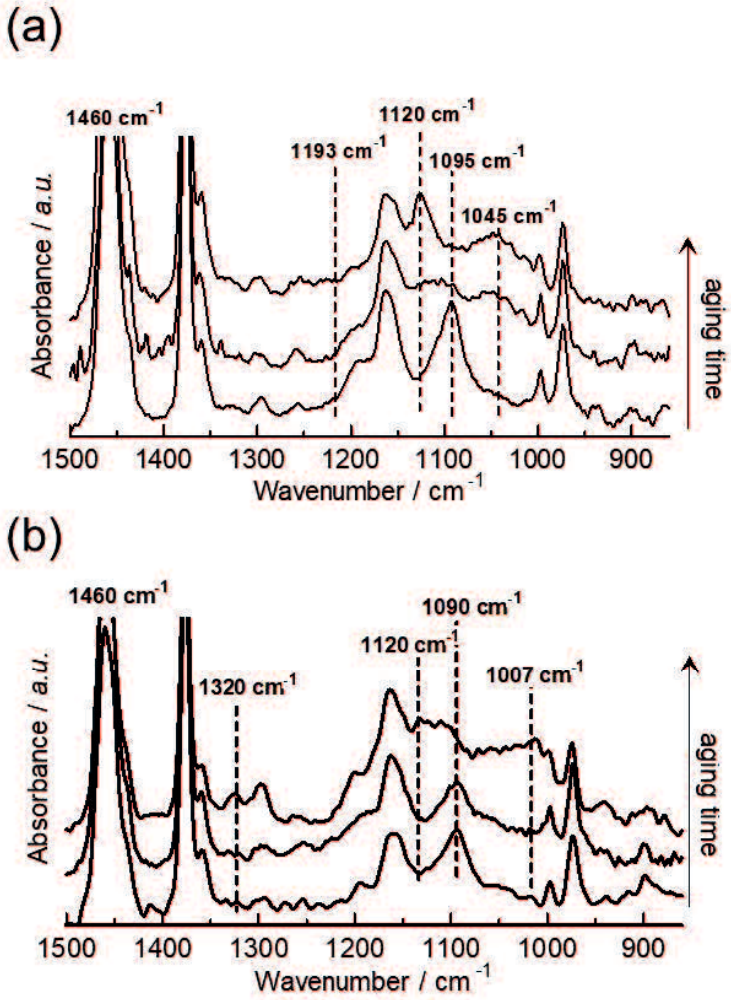

Figure 4-1. Changes in the ATR–FTIR spectra of the EPR-*g*-MTMS systems during the water-crosslinking reaction in the presence of (a) TPPO (5.0×10^{-4} mol/100 g EPR resin) and (b) TPPE (5.0×10^{-4} mol/100 g EPR resin) at 80 °C. The peak assignments are summarized in the text.

Kinetics of the hydrolysis in the EPR-*g*-MTMS system containing several organophosphorus compounds using Arrhenius plots

In our previous study, since water diffusion into the EPR-*g*-MTMS system was not the rate-determining step of the water-crosslinking reaction, the extent of the hydrolysis reaction of the Si–OCH_3 groups was determined using the A_{1095}/A_{1460} ratios. The dynamics of a typical hydrolysis reaction performed at 30, 50, and 80 °C using PA, TPPE, TPPO, and TPP as the catalysts are presented in Figure 4-2, where the A_{1095}/A_{1460} ratios are plotted against the aging time. Under these conditions, all tested systems underwent hydrolysis of the alkoxysilane groups of the EPR-*g*-MTMS systems. To evaluate the kinetics of the hydrolysis reaction in detail, the r^0_{hyd} (h^{-1}) of the reaction was defined as follows:

$$r^0_{hyd} = \left| \frac{d\left(A_{1095} / A_{1460}\right)}{dt} \right|_{t=0} \quad \text{..... (4.2)}$$

The actual r^0_{hyd} values were determined by differentiating the quadratic equation used to fit the experimental data. The catalytic performance of TPP was poor; however, the phosphoryl compounds, such as TPPO, PA, and TPPE, significantly promoted the hydrolysis reaction in the EPR-*g*-MTMS system. These results indicated that the P=O units of the catalysts improved their catalytic activity for the hydrolysis reaction. The r^0_{hyd} value of the TPPO-containing EPR-*g*-MTMS system was higher than those of the systems containing the other catalysts. Activation energy is a commonly used to evaluate catalytic activity. Typically, the lower the activation energy of a catalyst, the higher its catalytic activity. The Arrhenius plots of the hydrolysis reaction in the EPR-*g*-MTMS system using several catalysts are presented in Figure 4-3. According to the Arrhenius equation:

$$\ln r^0_{hyd} = \ln A'_{hyd} - \frac{E_{a,hyd}}{RT}, \quad \text{..... (4.3)}$$

where A'_{hyd} is the empirical constant comprising the frequency factors A and [MTMS], and $E_{a,hyd}$ is the activation energy for the hydrolysis reaction. The $E_{a,hyd}$ values obtained from Figure 4-3 are listed in Table 4-1 and were used to compare the catalytic activities of the organophosphorus compounds for the hydrolysis reaction in this system. The $E_{a,hyd}$ values increased as follows: phosphine oxides < phosphoric acids < phosphoric esters < phosphine ≈ no catalyst. It can be inferred that the phosphine oxides outperformed the other catalysts for the hydrolysis reaction in this system, as confirmed by the changes in the A_{1095}/A_{1460} ratios of the analyzed systems with time (Figure 4-2). The catalytic activity of CH_3–DPPO was significantly higher than those of the other phosphine oxides. Furthermore, the $E_{a,hyd}$ values of the phosphoric acids depended significantly on the number of hydroxyl groups in their structure. The $E_{a,hyd}$ value of PA (38.4 kJ mol^{-1}) was the highest among all the phosphoric acids used as catalysts in this study, and was comparable to those of the systems containing phosphoric esters. Herein, the catalytic activities of the phosphoric acids did not depend on their pK_a values (PA: 1.83, MPPA: 1.83, and DPPA: 2.32).[18] These results indicate that the catalytic activities of the phosphoryl compounds depended on the substituents.

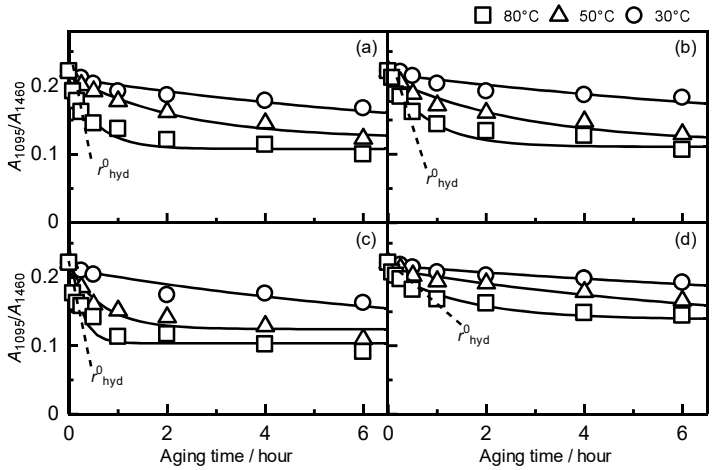

Figure 4-2. Dependence of the A_{1095}/A_{1460} ratio of water-crosslinked EPR-*g*-MTMS in the presence of (a) PA, (b) TPPE, (c) TPPO, and (d) TPP on the aging time at 30 (open circle), 50 (open triangle), and 80 °C (open square).

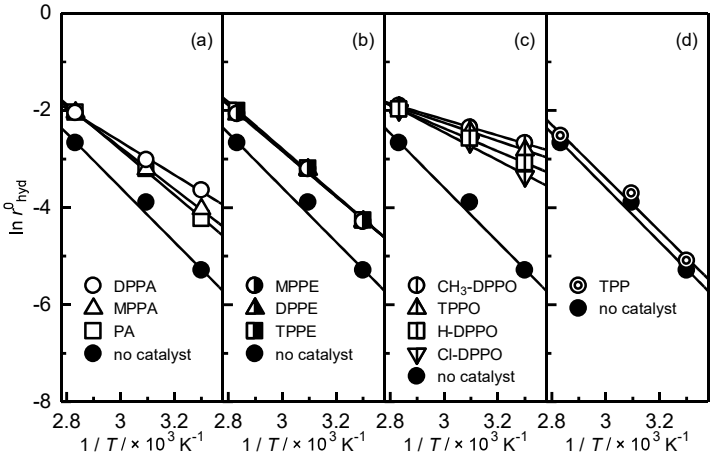

Figure 4-3. Dependence of the logarithmic hydrolysis rates on the reciprocal absolute temperature for the EPR-*g*-MTMS in the presence of (a) phosphoric acids, (b) phosphoric esters, (c) phosphine oxides, and (d) phosphine. The solid lines were obtained using Eq (4.3)

Table 4-1. Calculated Mulliken atomic charges on the O atoms of the phosphoryl (P=O) groups, activation energy of the hydrolysis and overall water-crosslinking reactions ($E_{a,hyd}$ and $E_{a,crk}$, respectively) for the EPR-*g*-MTMS system and the average molecular weight between crosslinks (M_c) for the water-crosslinked EPR-*g*-MTMS

Catalyst[a]		Atomic charge on the O atom of the P=O group	Activation energy [kJ mol^{-1}]		Average molecular weight between crosslinks
			$E_{a,\,hyd}$[c]	$E_{a,\,crk}$[d]	M_c[e] [g mol^{-1}]
Phosphoric acids	PA	-0.608	38.8 ± 0.5	43.1 ± 1.2	(4.55 ± 0.09) × 10^4
	MPPA	-0.625	35.4 ± 1.5	40.7 ± 1.0	(3.69 ± 0.08) × 10^4
	DPPA	-0.652	28.4 ± 0.2	38.4 ± 0.5	(3.49 ± 0.15) × 10^4
Phosphoric esters	MPPE	-0.598	39.2 ± 1.1	44.7 ± 0.8	(4.58 ± 0.37) × 10^4
	DPPE	-0.602	38.3 ± 0.6	43.6 ± 1.8	(4.62 ± 0.20) × 10^4
	TPPE	-0.602	39.9 ± 0.2	43.8 ± 1.2	(4.65 ± 0.11) × 10^4
Phosphine oxides	TPPO	-0.822	15.6 ± 0.8	31.4 ± 0.8	(1.20 ± 0.08) × 10^4
	Cl-DPPO	-0.733	24.0 ± 0.2	36.9 ± 0.3	(1.40 ± 0.10) × 10^4
	H-DPPO	-0.776	19.7 ± 0.2	34.6 ± 0.6	(1.27 ± 0.05) × 10^4
	CH_3-DPPO	-0.900	13.7 ± 1.2	30.4 ± 0.4	(1.11 ± 0.08) × 10^4
Phosphine	TPP	---	45.5 ± 0.8	64.0 ± 1.5	(10.09 ± 0.75) × 10^4
no catalyst		---	46.5 ± 0.9	66.4 ± 1.2	---

[a] catalyst concentration: 5.0 × 10^{-4} mol/100 g EPR resin; [b] obtained using DFT calculation at the B3LYP/6-31 level of theory. [c] determined using ATR-FTIR spectroscopy; [d] determined using the gel content; [e] aged in water at 80 °C for 24 h

Kinetics of the overall water-crosslinking reaction of EPR-g-MTMS containing various organophosphorus compounds using gel fraction measurements

The time evolution of the gel contents of the crosslinked EPR-*g*-MTMS systems in the presence of PA, TPPE, TPPO and TPP is presented in Figure 4-4. The gel content dependent significantly on the catalyst and aging temperature. In the absence of catalysts, the gel contents were negligible after 6 h of aging. Conversely, the gel content of the TPPO-containing EPR-*g*-MTMS system exceeded 85 %. This gel content was significantly higher than those of the PA-, TPPE-, and TPP-containing EPR-*g*-MTMS systems. The gel contents of the PA-, TPPE-, and TPP-containing EPR-*g*-MTMS systems reached 85 % after 24 h even when the overall water-crosslinking reaction was performed at 80 °C. To compare the catalytic activities of PA, TPPE, TPPO, and TPP for the overall water-crosslinking reaction of the EPR-*g*-MTMS systems, kinetic studies were performed. The initial overall water-crosslinking reaction rate, (r^0_{crk} (% h^{-1})), can be expressed using the gel content as follows:

$$r^0_{crk} = \left| \frac{d(\text{gel content})}{dt} \right|_{t=0} \quad \text{..... (4.4)}$$

The actual r^0_{crk} values were determined by differentiating the quadratic equation used to fit the experimental data. Our results indicated that the r^0_{crk} value of the TPPO-containing EPR-*g*-MTMS system was significantly higher than those of the PA-, TPPE-, and TPP-containing EPR-*g*-MTMS systems. The differences in the r^0_{crk} values were ascribed to the collision efficiency, which was attributed to the diffusion behavior of the organophosphoryl compounds in the EPR-*g*-MTMS systems. Although we could not evaluate the diffusion of the organophosphoryl compounds in the EPR-*g*-MTMS systems, the results indicated that the r^0_{crk} values were affected by the catalyst structures. These findings were critical in determining the comprehensive catalytic mechanism of the

water-crosslinking reaction, which is discussed below. The linear dependence of the $\ln r^0_{crk}$ values of the EPR-*g*-MTMS systems containing various catalysts on the reciprocal absolute temperature is presented in Figure 4-5. According to Eq (4.5), the activation energies for the overall water-crosslinking reaction ($E_{a,crk}$) were determined from the slopes of the plots, as follows:

$$\ln r^0_{crk} = \ln A'_{crk} - \frac{E_{a,crk}}{RT}, \quad (4.5)$$

where A'_{crk} is the empirical constant comprising the frequency factors A for the overall water-crosslinking reactions and [MTMS]. The least-squares linear regression was very reliable ($R^2 > 0.98$). The observed $E_{a,crk}$ values are listed in Table 4-1. According to the data in Table 4-1, the phosphoryl compounds, especially the phosphine oxides, presented excellent catalytic activity for the hydrolysis and overall water-crosslinking reactions in the EPR-*g*-MTMS systems. The values of $E_{a,crk}$ increased as follows: phosphine oxides < phosphoric acids < phosphoric esters < phosphine ≈ no catalyst, which matched the trend in the $E_{a,hyd}$ values. These results indicate that the catalytic performance of the phosphine oxides featuring $O{=}PR_3$ moieties for the overall water-crosslinking reaction was superior to those of $O{=}P(OR')_3$ and PR_3.

M_c is a critical parameter that determines how far a network can extend to accommodate solvent and solute molecules. Therefore, M_c is a crucial property of crosslinked networks that can promote the application of silane-grafted polyolefin resins. The M_c values of the water-crosslinked EPR-*g*-MTMS systems were calculated using the Flory–Rehner equation (Eq. (2.29)), and the results are summarized in Table 4-1. The M_c values depended significantly on the catalysts type, indicating that the phosphoryl compounds played an important role in the silane–water-crosslinked network structure of the EPR-*g*-MTMS system. The M_c values obtained using the phosphine oxides were

considerably smaller than those obtained using the other catalysts, indicating that the crosslinked EPR-*g*-MTMS systems catalyzed by phosphine oxides consisted of high-density network structures. According to the silicate sol–gel chemistry principles, under base-catalyzed conditions, the sol–gel derived siloxane networks yield more highly branched clusters, which do not interpenetrate prior to gelation, therefore behaving as discrete clusters (so-called "monomer-cluster growth").[19,20] Based on this information, we concluded that the mechanism of the water-crosslinking reaction catalyzed by phosphoryl compounds resembled closely that of the silicate hydrolysis–condensation reactions catalyzed by basic catalysts. The detailed catalytic mechanism of the phosphoryl compounds is discussed in the following section.

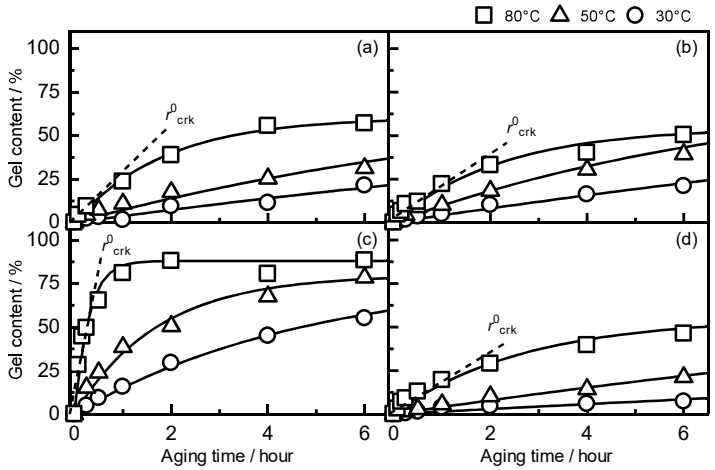

Figure 4-4. Time evolution of the gel content of the water-crosslinked EPR-*g*-MTMS in the presence of (a) PA, (b) TPPE, (c) TPPO, and (d) TPP at 30 (open circle), 50 (open triangle), and 80 °C (open square)

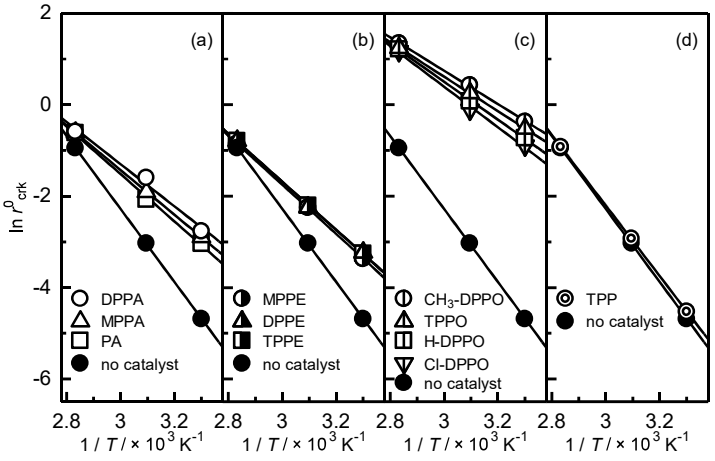

Figure 4-5. Dependence of the logarithmic overall water-crosslinking rates of the EPR-*g*-MTMS in the presence of (a) phosphoric acids, (b) phosphoric esters, (c) phosphine oxides, and (d) phosphine on the reciprocal absolute temperature. The solid lines were obtained using Eq (4.5).

DFT calculations of the organophosphorus compounds

To validate and identify the catalytic active sites of the phosphoryl compounds in this study, we used DFT calculations and MEP mappings. The MEP depends on the dipole moment, electronegativity, partial charges and chemically reactive sites of molecules, and MEP mappings provide a visual method for evaluating the relative polarity of molecules. Additionally, the atomic charges determined using Mulliken analysis were used to elucidate the nature of the P=O units of the catalysts. The values of the Mulliken charges of the O atoms of the P=O units are included in Table 4-1. The Mulliken charge decreased significantly as follows: phosphine oxides < phosphoric acids < phosphoric esters. These results indicate the strong relationship between the $E_{a,hyd}$ values of the phosphoryl compounds and Mulliken charges of the O atoms of the P=O units. That is, the phosphine oxides with lower Mulliken charges presented higher catalytic activities (Table 4-1). The MEP mappings revealed that the electron density was more localized on the P=O units and was lower on the hydroxyl functional groups of the phosphoric acids (Figure 4-6). This was ascribed to the high electron density of the P=O units enhancing their Lewis basicity, making them the preferential sites for nucleophilic attacks.[21,22] Consequently, the kinetic analysis data and theoretical results indicate that the catalytic activities of the phosphoryl compounds for the hydrolysis reaction primarily depended on the Lewis basicity of the P=O units. Considering these results, the catalytic mechanism of the phosphoryl compounds is discussed below.

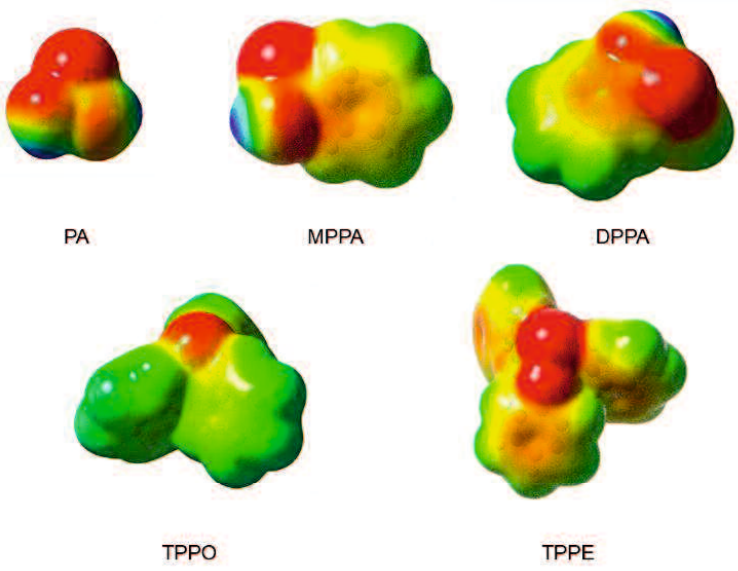

Figure 4-6. Molecular electrostatic potential mappings of the isodensities of PA, MPPA, DPPA, TPPO, and TPPE.

Calculated equilibrium geometries for the hydrolysis and condensation reactions

The equilibrium geometries for the complexes formed by CH_3–DPPO, TPPO, H–DPPO, and Cl–DPPO with water molecules in vacuum were obtained at the B3LYP/6-31 level of theory (Figure 4-7). The POH hydrogen bonds of all the complexes were short (1.78-1.86 Å). Moreover, the hydrogen bonds between the CH_3–DPPO and water molecules were shorter than those between the other phosphine oxides and water molecules. Experimentally, it was determined that CH_3–DPPO was a stronger Lewis base than the other phosphine oxides, and the Lewis basicity of the phosphine oxides was correlated with the DFT-calculated length of the hydrogen bonds.

Additionally, a comprehensive computational study was conducted using DFT calculations to determine the possible mechanistic pathways of the silane–water-crosslinking reaction in the presence of phosphine oxides. To ensure that the computational study was tractable, methyltrimethoxysilane ($CH_3Si(OCH_3)_3$) and trihydroxylmethylsilane ($CH_3Si(OH)_3$) were selected for the model reaction. The reaction pathways for the hydrolysis and condensation reactions to form a silanol and siloxane, respectively, were determined in the presence of TPPO, CH_3–DPPO, H–DPPO, and Cl–DPPO. The heats of formation of the reactants, intermediates, and products of the hydrolysis and condensation reactions were calculated using the corresponding total energy values of the reactants, intermediates, and products, respectively. The energies of the hydrolysis and condensation reactions in the presence of the phosphine oxides are listed in Table 4-2. The energy barrier values for the hydrolysis and condensation reactions in the presence of the phosphine oxides were calculated as follows:

$$\Delta H = H_{inter} - H_{ini}, \quad (4.6)$$

where H_{ini} and H_{inter} are the energies of the reactants and intermediates, respectively, for

both reactions. The equilibrium structures of the complexes obtained during the hydrolysis of $CH_3Si(OCH)_3$ in the presence of CH_3–DPPO are presented in Figure 4-8 as typical examples of DFT-calculated configurations. The stability of the $CH_3Si(OCH)_3$–H_2O–CH_3–DPPO complex, as an intermediate of the hydrolysis reaction was ascribed to the pentacoordinated Si atoms and O···Si and O···H hydrogen bonds. The condensation reaction of two $CH_3Si(OH)_3$ molecules in the presence of CH_3–DPPO is illustrated in Figure 4-9. The reaction intermediate consisted of the $CH_3Si(OH)_3$–CH_3–DPPO complex, which was formed via silanol···phosphoryl hydrogen bonds, whereas another $CH_3Si(OH)_3$ molecule participated in the condensation reaction. The optimal geometry for the condensation reaction was similar to that for the hydrolysis reaction (Figure 4-8). Moreover, the trends in the energy barriers of the hydrolysis and condensation reactions were the same: CH_3–DPPO < TPPO < H–DPPO < Cl–DPPO. Although these results cannot directly describe the reactions in the EPR-*g*-MTMS system, they demonstrate that a complex was formed between the phosphine oxide and water during the water-crosslinking reaction using phosphoryl compounds as catalysts.

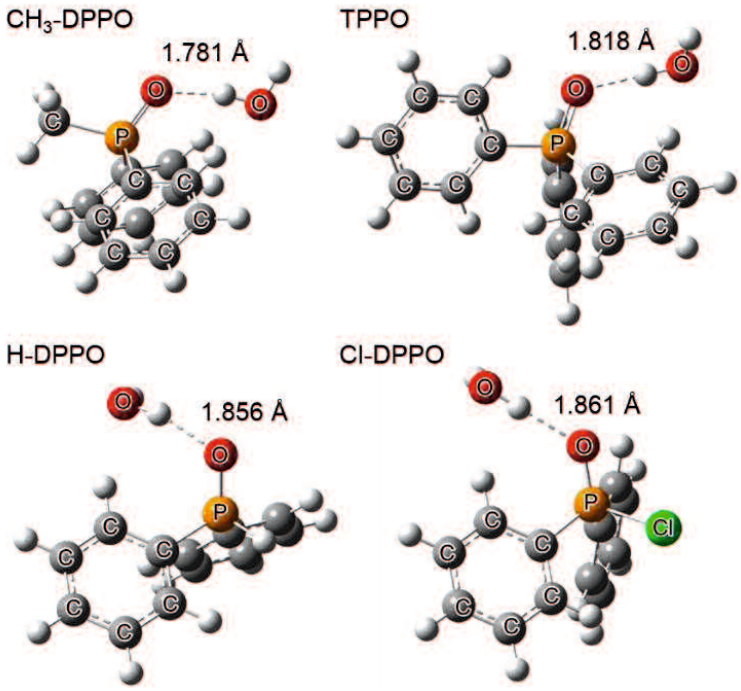

Figure 4-7. Calculated equilibrium structures of the complexes formed by the phosphine oxides with water molecule in vacuum. The bond lengths are listed next to the corresponding POH hydrogen bonds.

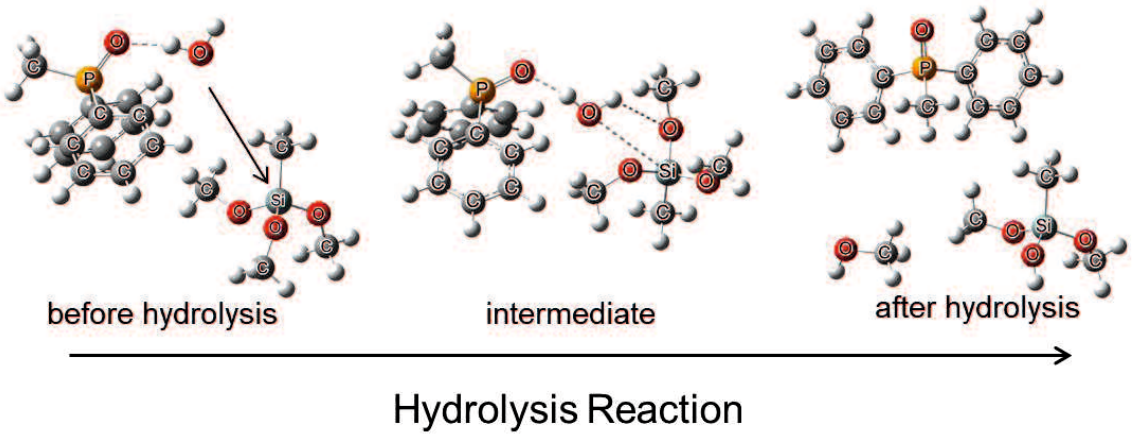

Figure 4-8. Geometries of the reactant, catalyst, intermediate, and products of the CH_3–DPPO-catalyzed hydrolysis of $CH_3Si(OCH)_3$.

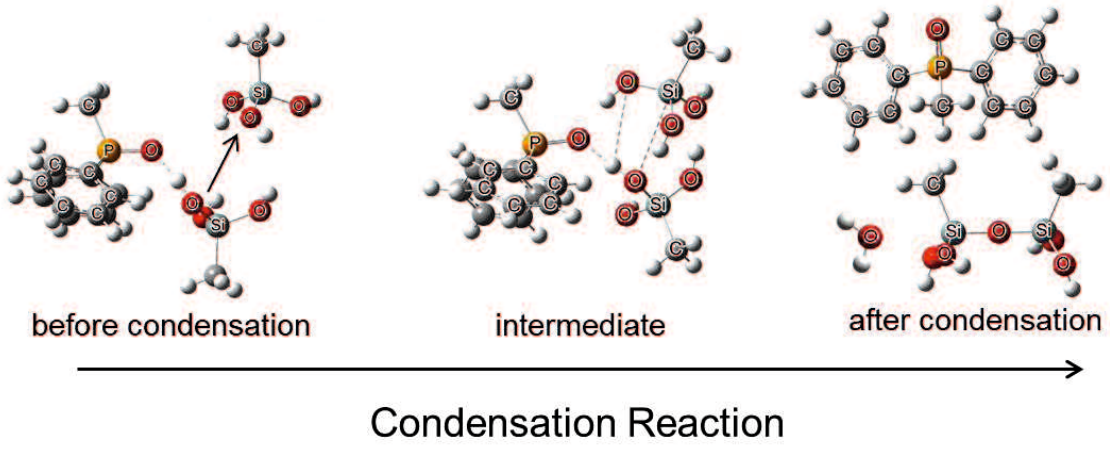

Figure 4-9. Geometries of the reactant, catalyst, intermediate, and products of the CH_3-DPPO– catalyzed condensation reaction of $CH_3Si(OCH)_3$.

Table 4-2. Heats of formation of the reactants (H_{ini}), intermediates (H_{inter}), and products (H_{prod}) of the hydrolysis and condensation reactions of EPR-*g*-MTMS in the presence of CH_3–DPPO, TPPO, H–DPPO and Cl–DPPO and calculated energy gaps (ΔH).

Catalyst	Hydrolysis				Condensation			
	H_{ini}[a]	H_{inter}[a]	ΔH	H_{prod}[a]	H_{ini}[a]	H_{inter}[a]	ΔH	H_{prod}[a]
	[kJ mol^{-1}]				[kJ mol^{-1}]			
CH_3-DPPO	-4370.77	-4344.28	26.48	-4357.28	-5336.81	-5289.66	47.15	-5304.84
TPPO	-4871.53	-4844.31	27.22	-4857.32	-5839.45	-5787.04	52.41	-5805.04
H-DPPO	-4272.75	-4242.32	30.44	-4257.37	-5250.58	-5187.70	64.98	-5204.94
Cl-DPPO	-5474.26	-5441.50	32.76	-5459.67	-6455.02	-6386.85	68.17	-6407.24

[a] calculated in vacuo at the B3LYP/6-31 level of theory at 298.15 K

Mechanism of the water-crosslinking reactions in the EPR-*g*-MTMS system with phosphoryl compounds

Based on the phenomena described above, we that the phosphoryl compounds served as conjugated Lewis base catalysts for the water-crosslinking reaction in the EPR-*g*-MTMS system. The possible elementary pathways for the water-crosslinking reactions of the EPR-*g*-MTMS systems using the phosphoryl compounds as the catalysts are presented in Scheme 4-3. The water-crosslinking reaction is considered to consist of the following steps. (a) The H and O atoms of water molecules form polar covalent bonds. The nucleophilicity of the O atoms and electrophilicity of the P atoms of the phosphoryl groups of phosphoric acid and related compounds are high. Therefore, the phosphine-oxide-based compounds can readily form conjugated Lewis bases with water molecules (Scheme 4-3(A)). The conjugated Lewis bases act as strong nucleophilic species. (b) The nucleophilic water moieties of the conjugated Lewis bases attack the unobstructed backsides of the Si atoms via an S_N2 mechanism and form a ternary intermediate state (methoxysilane group–water–phosphoryl compound) via weak O···Si and O···H bonds, subsequently forming silanol, methanol, and the original phosphoryl compounds. (c) The activation of the –Si–OH groups by the hydrogen-bonded complexes of the phosphoryl catalysts leads to an increase in the rate of Si–O–Si bond formation during the condensation step. Currently, we lack experimental evidence to support this reaction pathway that involves nucleophilic attack on the Si center of the alkoxysilane group. Nevertheless, a similar mechanism is widely adopted for the nucleophilic substitution reactions at the central Si atoms in traditional silicate sol–gel chemistry. For example, Bassindale et al. suggested that the conjugation of –Si–OH groups and Lewis base catalysts via hydrogen bonding led to a partial proton transfer from the –Si–OH groups to the catalysts, resulting in the formation of Si–O–Si linkages via the reaction of the

conjugated Lewis base with another –Si–OH group.[23]

The conjugated Lewis base of the phosphoryl compound and water molecule is a critical structure for understanding the origin of the catalytic efficiency of the phosphoryl compounds in the EPR-*g*-MTMS systems (Figure 4-7 and Scheme 4-3). The catalytic activities of the phosphoric acids and phosphoric esters for the hydrolysis and overall water-crosslinking reactions were weaker than those of the phosphine oxides. According to Mulloyarova et al.,[24] phosphoric acids and phosphoric esters easily formed water-bridged cyclic dimers and trimers via inter/intramolecular contiguous hydrogen bonds in the aqueous system. Consequently, the S_N2-Si reaction pathway via a nucleophilic attack can be hindered by the steric and electronic requirements of the comparatively bulky conjugated Lewis bases in the EPR-*g*-MTMS systems (Scheme 4-3(B)). Phosphoric acids and phosphoric esters contain highly nucleophilic $O=P(OR')_3$ units, promoting the formation of networks consisting of silicophosphate (Si–O–P) linkages via transesterification.[25-27] Phosphoric acids and phosphoric esters are consumed to form the Si–O–P linkages; therefore, they cannot serve as catalysts during the condensation step. Further mechanistic studies on the water-crosslinking reaction catalyzed by various phosphoryl compounds (conjugated Lewis bases) are underway.

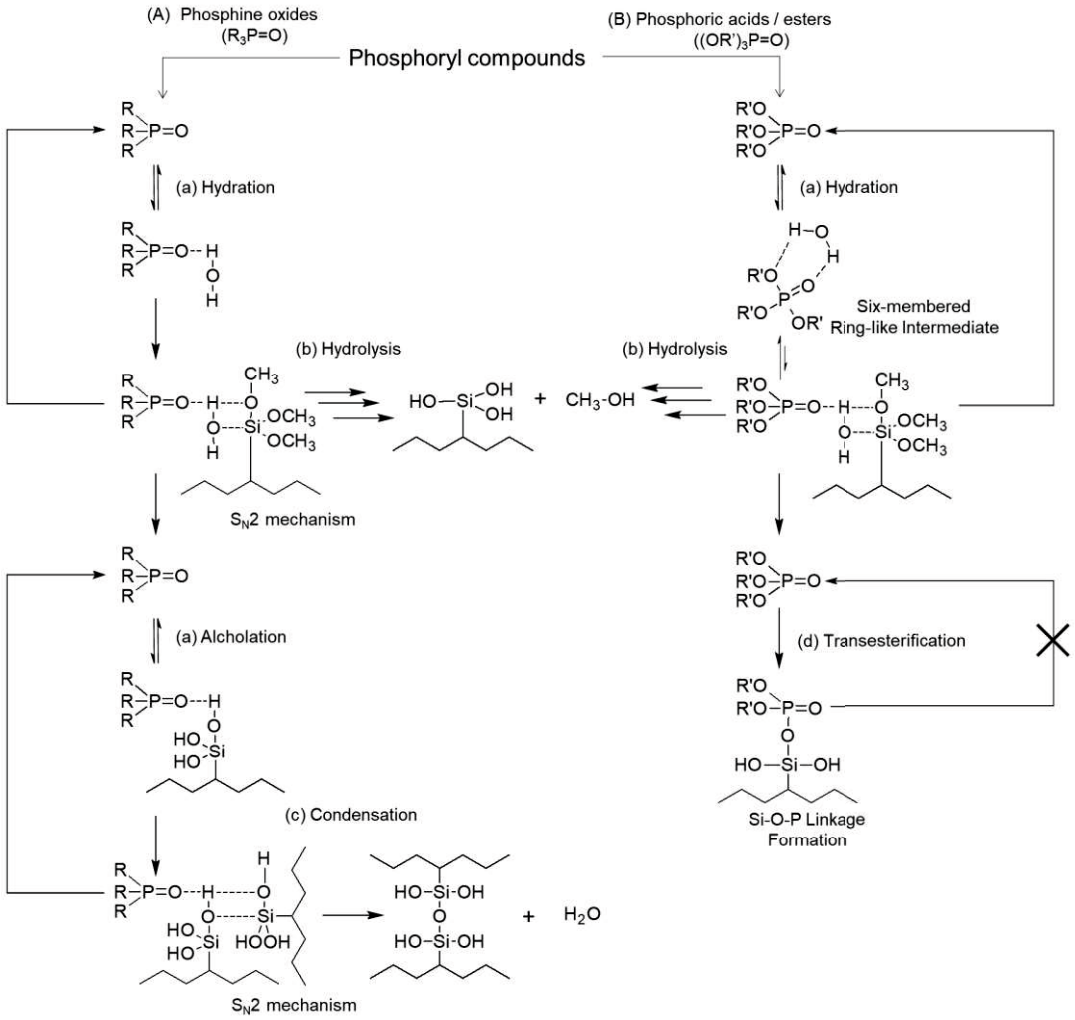

Scheme 4-3. Suggested catalytic cycle for the water-crosslinking reaction in a silane-grafted polyolefin system with phosphoryl compounds.

Kinetics of the hydrolysis reaction in the phosphoric-acid-containing EPR-*g*-MTMS system

In the previous section, we demonstrated that the Lewis base P=O moieties of organophosphorus compounds served as catalytic active sites to accelerate the water-crosslinking reaction in the EPR-*g*-MTMS system. PPA has been used as a Lewis base catalyst for the silicate hydrolysis–condensation reaction since its P=O moieties form hydrogen bonds with the proton donor to enhance the nucleophilicity of the reaction trigger. Being inspired by this concept, the catalytic performance of PPA for the water-crosslinking reaction in the silane-grafted polyolefin system was investigated.

PPA exists as an equilibrium mixture comprising several linear phosphoric acid oligomers. Acyclic oligomers have been denoted in the literature as P*n*, where *n* is the degree of oligomerization. Jameson evaluated the distribution of the oligomers and determined that it depended on the phosphorus pentoxide content (%P_2O_5) of the mixture.[28] The distribution of the oligomers in the catalysts in this study is listed in Table 4-3. The distribution of the oligomers in PA, which corresponded to PPA($P_2O_5$72), is listed in Table 4-3 as a reference. For PA, the P1 oligomer dominated. As the P_2O_5 content of PPA was increased, the shorter oligomers were converted into longer ones ($n > 3$). For PPA($P_2O_5$84), the complexity of the oligomers increased rapidly, and P1-P14 were present in this sample.

The water-crosslinking reaction in the EPR-*g*-MTMS system was monitored using ATR–FTIR absorbance spectroscopy. The ATR–FTIR spectra of the EPR-*g*-MTMS resin in the presence of DBTL and PPA($P_2O_5$84) are illustrated in Figure 4-10(A) and (B), respectively. The changes in the ATR–FTIR spectra of the DBTL- and PPA($P_2O_5$84)-containing EPR-*g*-MTMS resins were similar to those in the spectra of the TPPO-containing EPR-*g*-MTMS system during the water-crosslinking reaction (Figure 4-1(A)).

These results demonstrated that the water-crosslinking reaction in the EPR-*g*-MTMS system was catalyzed by PPA and DBTL. The time evolution of the A_{1095}/A_{1460} ratio for the reaction catalyzed by DBTL and PPA($P_2O_5$84) at 30, 50, and 80 °C is presented in Figure 4-11. As a reference, the A_{1095}/A_{1460} ratio for the water-crosslinking reaction of the EPR-*g*-MTMS system in the absence of catalysts is also illustrated in Figure 4-11. The r^0_{hyd} (h^{-1}) values calculated using Eq. (4.2) were obtained by differentiating the quadratic equation used to fit the experimental data. Because the hydrolysis reaction in this EPR-*g*-MTMS system was thermally activated, the temperature dependence of r^0_{hyd} can be expressed using an Arrhenius-type exponential function (Eq. (4.3)). The temperature dependence of r^0_{hyd} presented an excellent Arrhenius-type behavior (Figure 4-12). The $E_{a,hyd}$ values were calculated from the slopes of the $\ln r^0_{hyd}$ vs. $1/T$ curves of the catalysts, and the results are summarized in Table 4-4. The $E_{a,hyd}$ values decreased as follows: no catalyst > PA > DBTL > PPA($P_2O_5$75) > PPA($P_2O_5$80) > PPA($P_2O_5$82) > PPA($P_2O_5$84). These results indicate that the catalytic activity of PPA for the hydrolysis reaction in the EPR-*g*-MTMS system was higher than that of DBTL.

Although the ATR–FTIR spectra for the hydrolysis of the EPR-*g*-MTMS systems containing various PPAs were similar, the $E_{a,hyd}$ values of these reactions were significantly different. The catalytic efficiencies of the PPAs used for the hydrolysis reaction were affected by the P_2O_5 contents of the PPAs. To gain more in-depth insight into the dependence of the catalytic activity of the PPAs on their P_2O_5 contents, we assessed the relative Lewis basicity of each oligomer (P1-P14) using comprehensive DFT calculations. The average Mulliken atomic charge of the O atoms of the P=O moieties decreased with increasing degree of oligomerization (Table 4-5). Moreover, according to the molecular structure of P3 (Figure 4-13), the Mulluiken charge decreased toward the

center of the P=O unit from the terminal ones. Similar tendencies were observed for the other P*n* oligomers. This behavior was ascribed to the inductive effect. Upon increasing the degree of oligomerization of PPAs, the electrons in the resonance structure became stabilized via delocalization, causing the central P=O units of the higher phosphoric acid oligomers to became negatively charged. Masson and Gagne have previously reported that the Lewis basicity of the P=O units was remarkably enhanced by the neighboring electronegative groups, which inductively withdrew electrons, and the resonance effect.[29]

In the previous section, we reported that the organophosphoryl ($R_3P=O$) compounds formed conjugated bases with water molecules via hydrogen bonding ($R_3P=O\cdots H–OH$), and then catalyzed the water-crosslinking reaction in the EPR-*g*-MTMS system owing to their Lewis base behavior. According to the Mulliken charge transfer theory, the formation of hydrogen bonds between proton donors and acceptors depends on the electron density, which is transferred from a non-bonding orbital of the acceptor to an anti-bonding orbital of the donor.[30] Therefore, the hydrogen bond strength is a potential descriptor of Lewis basicity. The binding energies of the hydrogen bonds (ΔE) can be calculated as follows:

$$\Delta E = TE_{hyd} - TE_{s} \quad , \quad (4.7)$$

where TE_s is the sum of the total energy of the P*n* oligomers and a water molecule, and TE_{hyd} is the total energy of the corresponding hydrate. ΔE increased with increasing degree of oligomerization, and the calculated ΔE values are listed in Table 4-5. The calculations predicted that P14 formed a more stable hydrate than the other oligomers. This was ascribed to the presence of the highly Lewis basic P=O units in the structure of P14, which played a critical role as proton acceptors and withdrew protons from water molecules. Although these results cannot directly describe the reaction in the EPR-*g*-

MTMS system, they revealed the differences in the catalytic activities of the PPAs for the water-crosslinking reaction.

Table 4-3. Distribution of the phosphoric acid oligomers in the investigated PPAs according to Jameson.[2]

P*n*	Catalyst phosphorus pentoxide content (%P_2O_5)				
	PA 72 %P_2O_5	PPA($P_2O_5$75) 75 %P_2O_5	PPA($P_2O_5$80) 80 %P_2O_5	PPA($P_2O_5$82) 82 %P_2O_5	PPA($P_2O_5$84) 84 %P_2O_5
P1	91.0	53.9	12.6	6.7	3.9
P2	9.0	40.7	38.2	23.0	11.8
P3		4.9	23.0	19.3	12.7
P4		0.5	13.0	15.9	12.0
P5			6.9	12.3	10.5
P6			3.4	8.2	9.0
P7			1.7	5.7	8.0
P8			1.0	3.9	6.6
P9			0.2	2.5	5.6
P10				1.4	4.5
P11				0.9	3.7
P12				0.1	3.0
P13					2.5
P14					6.1

Table 4-4. Calculated activation energies of the hydrolysis reactions ($E_{a,hyd}$) in the EPR-*g*-MTMS systems and average molecular weight between crosslinks (M_c) for the water-crosslinked EPR-*g*-MTMS.

Catalyst [a]	$E_{a,hyd}$ [c] [kJ mol^{-1}]	M_c [b] [g mol^{-1}]
PPA($P_2O_5$84)	9.0 ± 0.1	(2.3 ± 0.1) × 10^4
PPA($P_2O_5$82)	9.2 ± 0.1	(2.7 ± 0.1) × 10^4
PPA($P_2O_5$80)	11.6 ± 0.4	(3.3 ± 0.1) × 10^4
PPA($P_2O_5$75)	12.6 ± 0.2	(4.0 ± 0.1) × 10^4
PA	38.8 ± 0.3	(4.6 ± 0.1) × 10^4
DBTL	13.1 ± 0.5	(4.3 ± 0.1) × 10^4
without catalyst	46.9 ± 1.2	---

[a] catalyst concentration: 0.15 phr

[b] aged at 80 °C for 24 h

[c] determined using ATR–FTIR spectroscopy

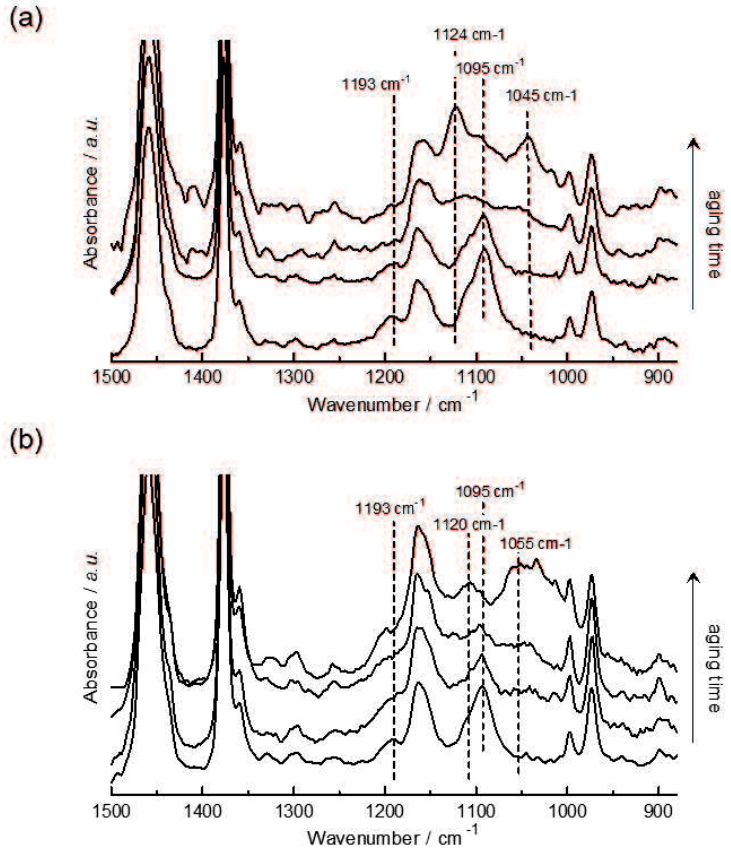

Figure 4-10. Changes in the ATR–FTIR spectra during the water-crosslinking reaction of the EPR-*g*-MTMS system in the presence of (a) DBTL and (b) PPA($P_2O_5$84). Catalyst concentration: 0.15 phr/100 g EPR resin.

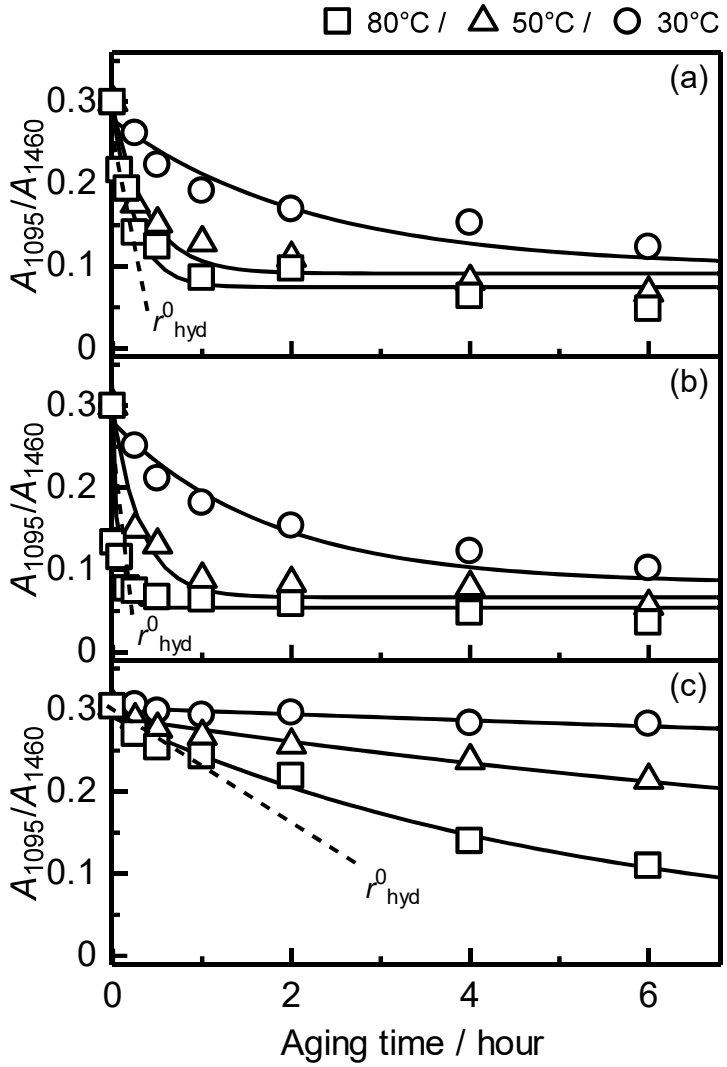

Figure 4-11. Time evolution of the A_{1095}/A_{1460} ratio for the water-crosslinked EPR-*g*-MTMS (a) DBTL, (b) PPA($P_2O_5$84), and (c) in the absence of catalysts at 30 (open circle), 50 (open triangle), and 80 °C (open square).

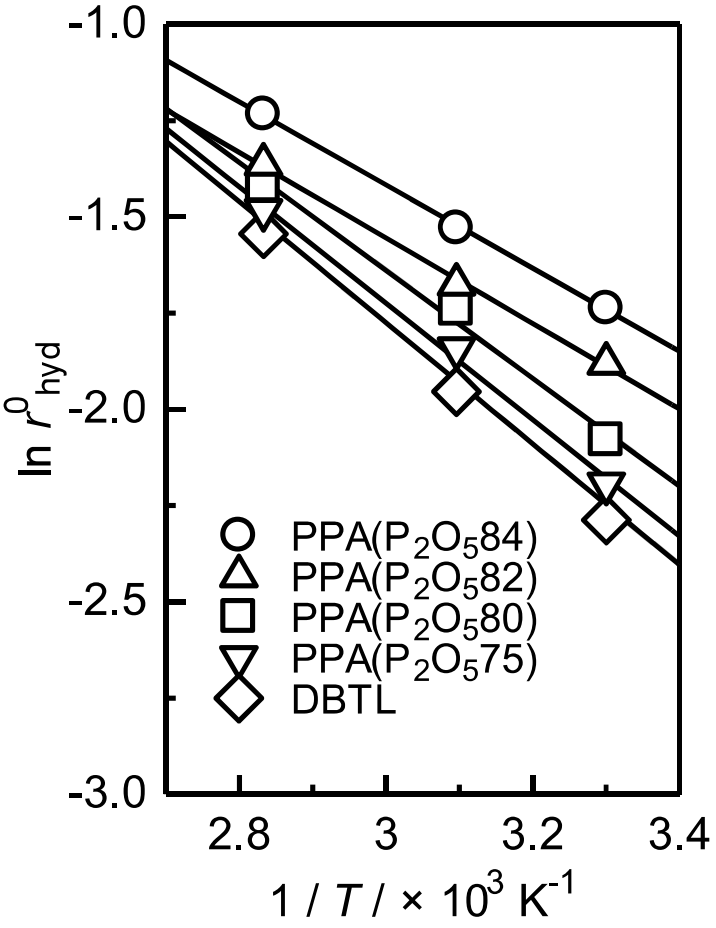

Figure 4-12. Dependence of the logarithmic hydrolysis rates on the reciprocal absolute temperature for the EPR-*g*-MTMS in the presence of PPA with various P_2O_5 contents and DBTL. The solid lines were obtained using Eq. (4.3).

Table 4-5. verage Mulliken atomic charge of the O atoms of the phosphoryl (P=O) moieties and calculated binding energies (ΔE) of the hydrogen bonds between the P=O moieties and water molecules.

Phosphoric acid oligomer (P*n*)		Average Mulluiken charge of the O atoms of the P=O moieties	Binding energy ΔE [kJ mol^{-1}]
P1	HPO_4	-0.63	$(1.87 \pm 0.05) \times 10^5$
P2	$H_4P_2O_7$	-0.65	$(1.97 \pm 0.03) \times 10^5$
P3	$H_5P_3O_{10}$	-0.69	$(1.99 \pm 0.02) \times 10^5$
P4	$H_6P_4O_{13}$	-0.72	$(2.01 \pm 0.03) \times 10^5$
P5	$H_7P_5O_{16}$	-0.79	$(2.14 \pm 0.05) \times 10^5$
P6	$H_8P_6O_{19}$	-0.81	$(2.19 \pm 0.03) \times 10^5$
P8	$H_{10}P8O_{25}$	-0.87	$(2.29 \pm 0.05) \times 10^5$
P10	$H_{12}P_{10}O_{31}$	-0.89	$(2.45 \pm 0.06) \times 10^5$
P12	$H_{14}P_{12}O_{37}$	-0.90	$(2.56 \pm 0.08) \times 10^5$
P14	$H_{16}P_{14}O_{43}$	-0.92	$(2.65 \pm 0.03) \times 10^5$

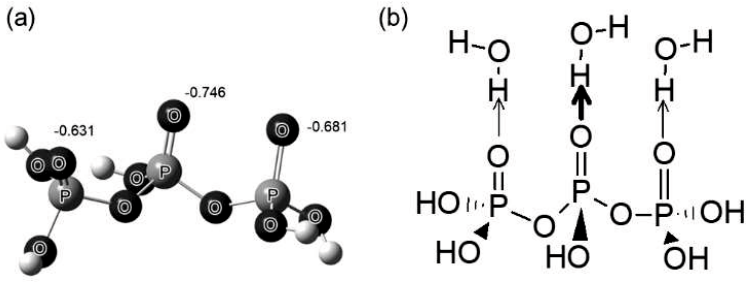

Figure 4-13. (a) Calculated equilibrium structure of P3 in vacuum. The Mulluiken atomic charges of the O atoms are listed next to the corresponding P=O units. (b) Hydrogen bonds between water molecules and the P=O units of the P3 oligomer. The arrow sizes illustrate the relative strengths of the hydrogen bonds.

Conclusion

In summary, we performed organocatalytic water-crosslinking reactions in the EPR-*g*-MTMS system using various organophosphorus compounds as catalysts. Phosphoryl compounds, in particular phosphine oxides, promoted the water-crosslinking reaction efficiently. Kinetic studies and DFT calculations indicated that the catalytic activity of the phosphoryl compounds depended on their Lewis basicity. Although the detailed catalytic mechanism has not been elucidated, DFT calculations were performed to determine the effects of the phosphine oxides and hydrogen donors on the catalytic performance, and the results suggested that the formation of hydrogen bonds promoted the nucleophilic activation of the water molecules in the reaction system. The use of phosphoryl compounds as catalysts can expand the scope of the metal-free water-crosslinking reaction in silane-grafted polyolefin systems and lead to the development of new advanced and environmentally friendly materials for industrial use.

References

1. M. Cypryk, B. Gostyruski, M. Pokora, *New J. Chem.*, **2019**, *43*, 15222-15232.
2. E. M. Valliant, J. R. Jones, *Soft Matter*, **2011**, *7*, 5083-5095.
3. L. S. Connell, L. Gabrielli, O. Mahony, L. Russo, L. Copolla, J. R. Jones, *Polym. Chem.*, **2017**, *8*, 1095-1103.
4. H. Sardon, A. C. Engler, J. M. W. Chan, J. M. Garcia, D. J. Coady, A. Pascual, D. Mecerreyes, G. O. Jones, J. E. Rice, H. W. Horn, J. L. Hedrick, *J. Am. Chem. Soc.*, **2013**, *135*, 16235-16241.
5. I. S. Ignatyev, M. Montejo, J. J. L. Gonzalez, *Phys. Chem. Chem. Phys.*, **2009**, *11*, 841-847.
6. A. R. Bassindale, Z. Liu, I. A. Mackinnon, P. G. Taylor, Y. Yang, M. E. Light, P. N.

Horton, M. B. Hursthouse, *Dalton Trans.*, **2003**, *14*, 2945-2949.

7. K. Suzawa, M. Ueno, A. E. H. Wheatley, Y. Kondo, *Chem. Commun.*, **2006**, 4850-4852.
8. K. Kobayashi, M. Ueno, Y. Kondo, *Chem. Commun.*, **2006**, 3128-3130.
9. T. Saito, Y. Aizawa, K. Tajima, T. Isono, T. Satoh, *Polym. Chem.*, **2015**, *6*, 4374-4384.
10. M. A. F. Delgove, A. A. Wroblewska, J. Stouten, C. A. M. R. van Slagmaat, J. Noordijk, S. M. A. De Wildeman, K. V. Bernaerts, *Polym. Chem.*, **2020**, *11*, 3573-3584.
11. S. Chen, H. Wang, Z. Li, F. Wei, H. Zhu, S. Xu, J. Xu, J. Liu, H. Gebru, K. Guo, *Polym. Chem.*, **2018**, *9*, 732-742.
12. J. F. Gal, P. C. Maria, M. Yanez, O. Mo, *ChemPhysChem*, **2019**, *20*, 2566-2576.
13. E. Y. Tupikina, M. Bondensteiner, P. M. Tolstoy, G. S. Denisov, L. G. Shenderovich, *J. Phys. Chem. C*, **2018**, *122*, 1711-1720.
14. X. Liu, J. G. Verkada, *Heteroat. Chem.*, **2011**, *12*, 21-26.
15. T. Huang, Y. Saga, H. Guo, A. Yoshimura, A. Ogawa, L. B. Han, *J. Org. Chem.*, **2018**, *83*, 8743-8749.
16. J. K. West, *J. Biomed. Mater. Res.*, **1997**, *35*, 505-511.
17. J. K. West, L. L. Hench, *J. Mater. Sci.*, **1994**, *29*, 3601-3606
18. K. Makiguchi, T. Satoh, T. Kakuchi, *Macromolecules*, **2011**, *44*, 1999-2005.
19. R. Aelion, A. Loebel, F. Eirich, *J. Am. Chem. Soc.*, **1950**, *72*, 5705-5712.
20. W. T. Grubb, *J. Am. Chem. Soc.*, **1954**, *76*, 3408-3414.
21. Y. C. Tan, H. C. Zeng, *Nature Commun.*, **2018**, *9*, 4326.
22. I. S. Giba, V. V. Mulloyarova, G. S. Denisov, P. M. Tolstoy, *J. Phys. Chem. A*, **2019**, *123*, 2252-2260.

23. A. R. Bassindale, H. Chen, Z. Liu, A. Mackinnon, D. J. Parker, P. G. Taylor, Y. Yang, M. E. Light, P. N. Horton, M. B. Hursthouse, *J. Organomet. Chem.*, **2004**, *689*, 3287-3300.
24. V. V. Mulloyarova, I. S. Giba, G. S. Denisov, A. S. Ostras, P. M. Tolstoy, *J. Phys. Chem. A*, **2019**, *123*, 6761-6771.
25. A. Styskalik, M. Babiak, P. Machac, B. Relichova, J. Pinkas, *Inorg. Chem.*, **2017**, *56*, 10699-10705.
26. A. Styskalik, D. Skoda, Z. Moravec, M. Babiak, C. E. Barenes, J. Pinkas, *J. Mater. Chem. A*, **2015**, *3*, 7477-7487.
27. C. Weinberger, T. Heckel, P. Schnippering, M. Schmitz, A. Guo, W. Keil, H. C. Marsmann, C. Schmidt, M. Tiemann, R. Wihelm, *Nanomaterials*, **2019**, *9*, 249.
28. R. F. Jameson, *J. Chem. Soc.*, **1959**, 752-759.
29. J. F. Masson, M. Gagne, *Energy Fuels*, **2008**, 22, 3390-3394.
30. S. K. Jain, T. Tabassum, L. Li, L. Ren, W. Fan, M. Tsapatsis, S. Caratzoulas, S. Han, S. L. Scott, *J. Am. Chem. Soc.*, **2021**, 143, 1968-1983.

Chapter 5

Acid–base hybrid catalysts for the water-crosslinking reaction in the EPR-*g*-MTMS system

Introduction

Conventional organometallic catalysts, organic bases, and organic acids efficiently catalyze sol–gel silicate systems. Organometallic catalysts and organic bases are the most commonly used catalysts for the water-crosslinking reaction in silane-grafted polyolefin systems. We have recently used divalent metal acetylacetonate complexes and amine compounds as catalysts for the water-crosslinking reaction in silane-grafted polyolefin systems. The divalent metal acetylacetonate complexes acted as Lewis acid catalysts and the amine compounds served as Lewis/Bronsted base catalysts. Studies on these types of catalysts for the water-crosslinking reaction of silane-grafted polyolefin systems indicated that the type of catalyst (acid or base) significantly affected the water-crosslinking reaction rate and the nature the of siloxane network.

In organic chemistry, the concept of hybrid acid–base catalysts has attracted considerable attention, since it allowed researchers to maximize the advantages of both types of catalysts and combined their respective advantages to promote reactions and processes that individual acids or bases cannot catalyze.[1-3] Hybrid acid–base catalysis, also known as dual catalysis, presents great promise and caused a paradigm shift in synthetic organic chemistry.

Inspired by these findings, in this study, we expanded the use of this type of catalysts by investigating the catalytic performances of acid–base hybrid catalysts comprising metal acetylacetonates with axially coordinated primary *n*-alkylamine

compounds (RNH_2–M(II)$(acac)_2$; R = C_{14}, C_{16}, and C_{18}; M = Cu(II) and Zn(II)), for the water-crosslinking reaction in the EPR-*g*-MTMS system. The catalytic activity of the RNH_2– M(II)$(acac)_2$ complex for the hydrolysis reaction depended on the axially coordinated *n*-alkylamine compounds, whereas the central metal ion of the RNH_2–M(II)$(acac)_2$ complexes affected the catalytic activity for the overall water-crosslinking reaction. The concept of acid–base hybrid catalysts can be expanded to a broad catalyst for the water-crosslinking reaction of alkoxysilane-grafted polyolefin systems.

Experimental

Materials

Primary *n*-alkylamine compounds (RNH_2) (i.e., *n*-octylamine (C_8NH_2), *n*-tetradecylamine ($C_{14}NH_2$), and *n*-octadecylamine ($C_{18}NH_2$)) were purchased from Tokyo Kasei Kogyo Co., Ltd. (Tokyo, Japan). The anhydrous divalent metal acetylacetonate complexes (M(II)$(acac)_2$), (i.e., copper(II) acetylacetonate [Cu(II)$(acac)_2$] and zinc(II) acetylacetonate [Zn(II)$(acac)_2$]) were purchased from Aldrich (Milwaukee, WI, USA). All other materials were same as those described in Chapter 3 and were used without further purification.

Synthesis of the acid–base hybrid catalysts RNH_2–M(II)$(acac)_2$

The RNH_2–M M(II)$(acac)_2$ complexes used in this study were synthesized using the method of Brahma,[4] and the reaction is illustrated in Scheme 5-1. A chloroform solution of M M(II)$(acac)_2$ (2 mol) was slowly added to a previously prepared solution of *n*-alkylamine in chloroform (2 mol), and then the mixture was stirred for 2 h to complete the reaction. Thereafter, the solvent was evaporated and the powder materials were collected. The ^{1}H NMR spectra of the RNH_2–M(II)$(acac)_2$ complexes were recorded

using an AVANCE DPX-400 (400 MHz) spectrophotometer (Bruker, City, State, USA) and tetramethylsilane as the internal standard.

C_8NH_2–Cu(II)(acac)$_2$: complex yield: 70.1 % based on Cu(II)(acac)$_2$; ^{1}H NMR ($CDCl_3$, 400 MHz) broad spectrum; IR (KBr pellet, cm^{-1}) 3329 (m), 3252 (m), 3155 (m) 2920 (s), 2855 (s), 1578 (s), 1525 (s), 1465 (m), 1411 (m), 1351 (m), 1285 (m), 1183 (w), 1014 (m), 941 (m), 774 (m), 719 (m), 689 (w), 647 (w), 599 (w).

$C_{14}NH_2$–Cu(II)(acac)$_2$: complex yield: 76.3 % based on Cu(II)(acac)$_2$; ^{1}H NMR ($CDCl_3$, 400 MHz) broad spectrum; IR (KBr pellet, cm^{-1}) 3329 (m), 3252 (m), 3155 (m), 2920 (s), 2855 (s), 1578 (s), 1525 (s), 1465 (m), 1411 (m), 1351 (m), 1285 (m), 1190 (w), 1022 (m), 941 (m), 774 (m), 719 (m), 687 (w), 652 (w), 601 (w).

$C_{18}NH_2$–Cu(II)(acac)$_2$: complex yield: 76.5 % based on Cu(II)(acac)$_2$; ^{1}H NMR ($CDCl_3$, 400 MHz) broad spectrum; IR (KBr pellet, cm^{-1}) 3341 (m), 3264 (m), 3161 (m) 2918 (s), 2854 (s), 1578 (s), 1525 (s), 1465 (m), 1411 (m), 1351 (m), 1285 (m), 1185 (w), 1026 (m), 941 (m), 774 (m), 719 (m), 689 (w), 647 (w), 601 (w).

C_8NH_2–Zn(II)(acac)$_2$: complex yield 92.6 % based on Zn(II)(acac)$_2$; ^{1}H NMR ($CDCl_3$, 400 MHz) δ5.31 (CH of the acetylacetonate ring), δ1.97 (CH_3 of the acetylacetonate ring), δ1.42 (NH_2), δ0.88 (CH_3 of the alkyl chain); IR (KBr pellet, cm^{-1}) 3329 (m), 3252 (m), 3155 (m), 2920 (s), 2919 (s), 1599 (s), 1520 (s), 1461 (m), 1403 (m), 1263 (m), 1208 (m), 1190 (w), 1017 (m), 928 (m), 774 (m), 766 (m), 668 (w), 612 (w), 567 (w).

$C_{14}NH_2$–Zn(II)(acac)$_2$: complex yield: 93.1 % based on Zn(II)(acac)$_2$; ^{1}H NMR ($CDCl_3$, 400 MHz) δ5.31 (CH of the acetylacetonate ring), δ1.97 (CH_3 of the acetylacetonate ring), δ1.69 (NH_2), δ0.88 (CH_3 of the alkyl chain); IR (KBr pellet, cm^{-1}) 3329 (m), 3252 (m), 3155 (m), 2920 (s), 2855 (s), 1601 (s), 1518 (s), 1463 (m), 1406 (m), 1263 (m), 1208 (m), 1197 (w), 1017 (m), 928 (m), 774 (m), 766 (m), 668 (w), 612 (w), 567 (w).

$C_{18}NH_2$-Zn(II)(acac)$_2$: complex yield: 88.9 % based on Zn(II)(acac)$_2$; ^{1}H NMR ($CDCl_3$, 400 MHz) δ5.31 (CH of the acetylacetonate ring), δ1.97 (CH_3 of the acetylacetonate ring), δ1.29 (NH_2), δ0.88 (CH_3 of the alkyl chain); IR (KBr pellet, cm^{-1}) 3345 (m), 3260 (m), 3161 (m) 2920 (s), 2855 (s), 1599 (s), 1520 (s), 1460 (m), 1400 (m), 1260 (m), 1208 (m), 1197 (w), 1017 (m), 928 (m), 770 (m), 766 (m), 668 (w), 612 (w), 567 (w).

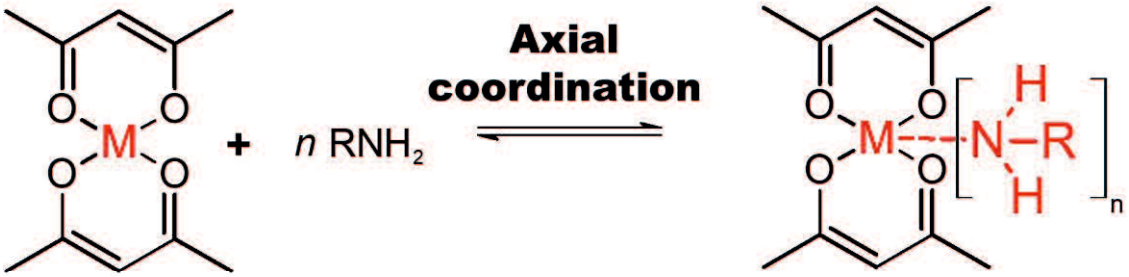

Scheme 5-1. Axial coordination reaction between the M(II)(acac)$_2$ complexes and *n*-alkylamine compounds in methanol solutions.

UV–vis spectroscopic titration

First, RNH_2 compounds were dissolved in chloroform to prepare stock solutions (5.0×10^{-4} mol dm^{-3}). Stock solutions of M(II)(acac)$_2$ (M = Cu(II) and Zn (II)) in chloroform (5.0×10^{-3} mol dm^{-3}) were also prepared. Various amounts of the RNH_2 stock solution were added to the M(II)(acac)$_2$ chloroform solution to obtain mixtures with different RNH_2:M(II)(acac)$_2$ molar ratios. Thereafter, the RNH_2–M(II)(acac)$_2$ chloroform solutions were injected into single compartment cells (path-lengths of 1.0 cm) with two quartz windows. The prepared binary solutions were stable for at least one week at room temperature. The UV–vis absorption spectra of the RNH_2–M(II)(acac)$_2$ chloroform solutions were obtained using a UV-1600 UV–vis spectrometer (Shimadzu, Kyoto, Japan).

Preparation of the water-crosslinked EPR-*g*-MTMS systems containing RNH_2–M(II)$(acac)_2$ complexes

EPR-*g*-MTMS was prepared using the same method described in Chapter 3. After grafting, the RNH_2–M(II)$(acac)_2$ complexes (5.0×10^{-4} mol/100 g resin) were added to the EPR-*g*-MTMS resin melted at 120 °C. The resultant EPR-*g*-MTMS samples containing the RNH_2–M(II)$(acac)_2$ complexes were shaped into ~1.0 mm thick compression-molded sheets via air pressing. Next, the sheets were cut into identical pieces, which were placed in water baths at 30, 50, or 80 °C. The samples were removed from the water baths after various times to examine the reaction progress. To avoid undesired water-cross-linking while waiting for analysis or further treatment, the samples were stored under dry conditions.

Kinetics of the hydrolysis and overall water-crosslinking reactions of the water-crosslinked EPR-*g*-MTMS systems

The kinetic analysis of the hydrolysis and overall water-crosslinking reactions of the water-crosslinked EPR-*g*-MTMS systems containing RNH_2–M(II)$(acac)_2$ complexes was performed using the same method described in Chapter 3.

Results and discussion

Stability constants of the RNH_2–$M(acac)_2$ complexes

Square-planar $M(II)(acac)_2$ complexes form octahedrally coordinated compounds with various ligands, such as nitrogen bases and phosphorous esters, in their axial positions.[5, 6] For example, $Cu(II)(acac)_2$ coordinates various N- and O-containing donor ligands to form coordination complexes. Spectrophotometry is an effective method for investigating the coordination of $M(II)(acac)_2$ complexes with various ligands.

The typical changes in absorption spectra upon the addition of a RNH_2 chloroform solution to a $Cu(II)(acac)_2$ chloroform solution are illustrated in Figure 5-1. For all the investigated conditions, the addition of the RNH_2 chloroform solution to the $Cu(II)(acac)_2$ chloroform solution led to significant changes in the absorption spectra. The absorption peaks at 552 and 668 nm in the UV–vis spectra of the $Cu(II)(acac)_2$ complex were assigned as metal-to-metal transitions (d–d transitions).[7] The intensity of the shoulder absorption peak at 552 nm decreased, whereas that of the absorption peak at 668 nm increased significantly during RNH_2 titration. Therefore, we hypothesized that these changes in the intensities of the absorption peaks were ascribed to the coordination between the planar $Cu(II)(acac)_2$ complex and RNH_2. Similar changes were observed in the UV–vis spectra of the RNH_2–$Zn(II)(acac)_2$ binary systems. Distinct isosbestic points were present in the UV–vis spectra of all the RNH_2–$M(II)(acac)_2$ chloroform solutions in this study, indicating that the spectral changes were caused by the initial and final species, and the effect of side reactions on the spectra can be neglected. In binary aqueous systems comprising $M(II)(acac)_2$ and organic compounds, such intensity changes with isosbestic points indicate the formation of 1:1 or 1:2 coordination complexes.[8] To determine the stability constants of the complexes formed by $M(II)(acac)_2$ and RNH_2 (K_{cpx}), the plots of $[(RNH_2)_n$–$M(II)(acac)_2]/[M(II)(acac)_2]$ vs. $[RNH_2]$ were obtained using the following

equations:

$$K_{\mathrm{cpx}} = \frac{[(\mathrm{RNH_2})_n - \mathrm{M(II)(acac)_2}]}{[\mathrm{M(II)(acac)_2}][\mathrm{RNH_2}]^n} \quad \text{..... (5.1)}$$

$$\log\left(\frac{\left[(\mathrm{RNH_2})_n\text{-}\mathrm{M(II)(acac)_2}\right]}{\left[\mathrm{M(II)(acac)_2}\right]}\right) = n \log\left[\mathrm{RNH_2}\right] + \log K_{\mathrm{cpx}} \quad \text{..... (5.2)}$$

where n is the number of ligands in the axial position the of $M(II)(acac)_2$ complexes and $[M(II)(acac)_2]$, $[RNH_2]$, and $[(RNH_2)_n–M(II)(acac)_2]$ are the equilibrium concentrations of the species in this system.

The $\log([(RNH_2)_n–M(II)(acac)_2]/[M(II)(acac)_2])$ vs. $\log([RNH_2])$ plots were linear, and their slopes were 1.0 (Figure 5-1(B)). Stoichiometric calculations using Eq. (5.2) suggested that a 1:1 complex was preferentially formed between $M(II)(acac)_2$ and RNH_2. The obtained K_{cpx} values of the $RNH_2–M(II)(acac)_2$ complexes are summarized in Table 5-1. The K_{cpx} values decreased as the carbon chain length of the substituents increased, as follows: $C_{18}NH_2 < C_{14}NH_2 < C_8NH_2$. These results indicated that the stability of the $RNH_2–M(II)(acac)_2$ complexes depended on the length of the alkyl chain of the axial ligand.

The chemical structure of the $RNH_2–M(II)(acac)_2$ complexes was investigated using FTIR spectrometry. For convenience, the FTIR spectra of the $C_8NH_2–Cu(II)(acac)_2$ and $C_{18}NH_2–Cu(II)(acac)_2$ complexes, $C_{18}NH_2$, and $Cu(II)(acac)_2$ are presented in Figure 5-2. We determined that the structures of all the $RNH_2–M(II)(acac)_2$ complexes were similar and presented features of both the $M(II)(acac)_2$ complexes and RNH_2 compounds. The peak at approximately 3280 cm^{-1} in the FTIR spectrum of the $C_{18}NH_2–Cu(II)(acac)_2$ complex was attributed to the stretching vibration of the N–H bonds.[9-11] This peak was redshifted by 10 cm^{-1} in the FTIR spectra of the $RNH_2–M(II)(acac)_2$ complexes compared with that of the pure RNH_2 compounds, indicating that the RNH_2 compounds coordinated

with Cu(II) via $–NH_2$ groups. In addition, the peak ascribed to the stretching vibration of the N–H bonds in the FTIR spectrum of the C_8NH_2–Cu(II)$(acac)_2$ complex exhibited a stronger red shift than that of the $C_{18}NH_2$–Cu(II)$(acac)_2$ complex. The red shifts of the absorption peaks toward lower wavenumbers indicated lower bonding energies and the formation of longer bond. Therefore, the red shift of the peak associated with the N–H bonds suggested that the structure formed in the $C_{18}NH_2$–Cu(II)$(acac)_2$ complex was tighter than that formed in the C_8NH_2–Cu(II)$(acac)_2$ complex. Several researchers demonstrated that the coordination complexes formed with M(II)$(acac)_2$ complexes via the N atoms of *n*-alkylamine compounds and the electronic density of the N atoms were the most important factors for coordination with M(II)$(acac)_2$ complexes.[12,13] The spectrophotometric data indicated that the changes in electronic density with the alkyl chains were probably responsible for the differences in the K_{cpx} values of the RNH_2–M(II)$(acac)_2$ complexes. These results indicated that coordination of the RNH_2 compounds to the metal ions in the acetylacetonate complexes stabilized the 1:1 complexes.

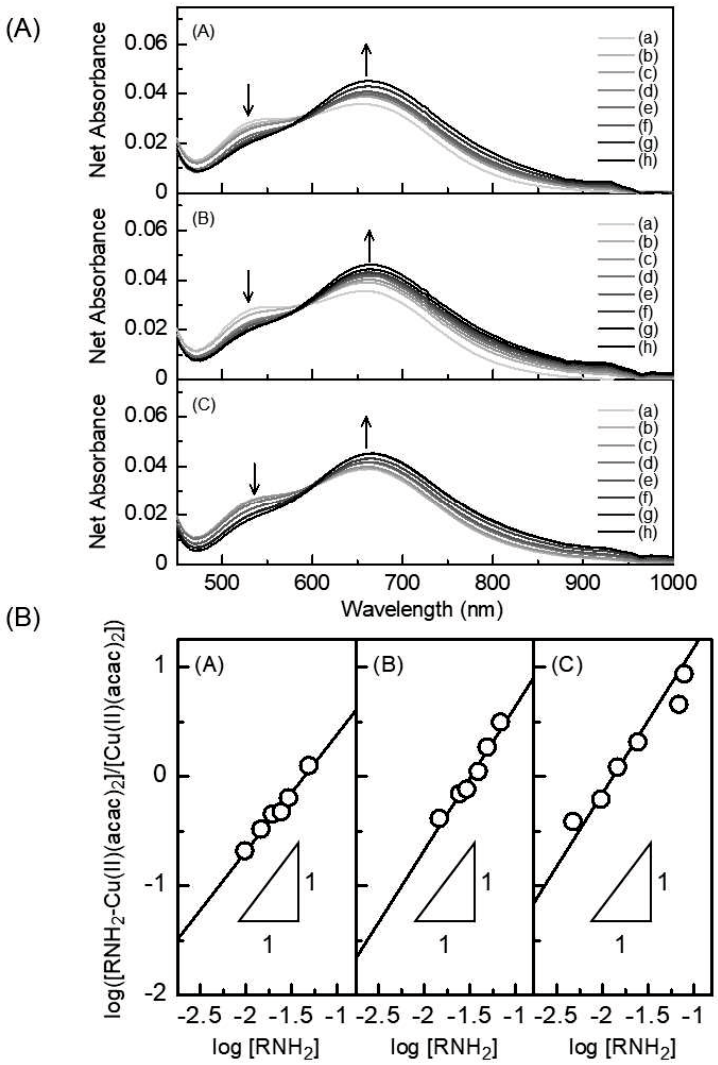

Figure 5-1. (A) Changes in the UV–vis absorption spectra of the Cu(II)(acac)$_2$ chloroform solution as a function of the concentration of added (A) $C_{18}NH_2$, (B) $C_{14}NH_2$, and (C) C_8NH_2 chloroform solutions. Experimental conditions: [Cu(II)(acac)$_2$] = 1.0 × 10^{-3} mol dm^{-3} and [RNH_2] = (a) 0, (b) 1.0 × 10^{-3}, (c) 5.0 × 10^{-3}, (d) 0.01, (e) 0.02, (f) 0.04, (g) 0.06, and (h) 0.08 mol dm^{-3}. The arrows indicate the directions of the changes in absorbance with increasing RNH_2 concentration. (B) Dependence of log([$(RNH_2)_n$–M(II)(acac)$_2$]/[M(II)(acac)$_2$]) on log([RNH_2]). The solid lines were obtained using Eq. (5.2).

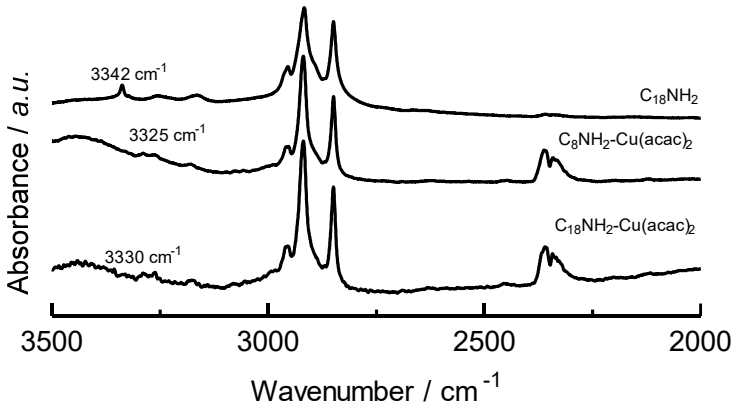

Figure 5-2. ATR–FTIR spectra of the $C_{18}NH_2$–Cu(II)$(acac)_2$ and C_8NH_2–Cu(II)$(acac)_2$ complexes and $C_{18}NH_2$.

Table 5-1. Stability constants of the RNH_2–M(II)$(acac)_2$ complexes (K_{cpx}) and numbers of ligands in the axial positions of the M(II)$(acac)_2$ complexes (n).

Metal(II) acetylacetonate complex	n-alkylamine compounds	Number of ligands n [a]	Stability constant K_{cpx} [a] [(mol dm^{-3})$^{-2}$]
Cu(II)$(acac)_2$	$C_{18}NH_2$	1	$(0.54 \pm 0.08) \times 10^2$
	$C_{14}NH_2$		$(0.92 \pm 0.16) \times 10^2$
	C_8NH_2		$(1.77 \pm 0.20) \times 10^2$
Zn(II)$(acac)_2$	$C_{18}NH_2$		$(0.48 \pm 0.12) \times 10^2$
	$C_{14}NH_2$		$(0.72 \pm 0.12) \times 10^2$
	C_8NH_2		$(0.93 \pm 0.30) \times 10^2$

[a] determined using UV–vis spectroscopic titration

Water-crosslinking reaction of the EPR-*g*-MTMS resins containing RNH_2–M(II)$(acac)_2$ complexes

The typical ATR–FTIR spectra obtained for the water-crosslinking of EPR-*g*-MTMS using the $C_{18}NH_2$–Cu(II)$(acac)_2$ complex as the catalysts are presented in Figure 5-3. The ATR–FTIR spectra of the systems catalyzed by the other RNH_2–M(II)$(acac)_2$ complexes were similar (data not reported). Two new peaks at 1060 and 1120 cm^{-1} emerged, and their intensities increased gradually with aging time (Figure 5-3). The absorption peaks at 1060 and 1120 cm^{-1} were assigned to –Si–O–Si– and –Si=$(O)_2$=Si– or –Si≡$(O)_3$≡Si– linkages, respectively. Correspondingly, the intensities of the peaks at 1095 and 1193 cm^{-1}, which correspond to the Si–O stretching and Si–C stretching vibration, respectively, of the methoxysilane groups (C–Si–OCH_3), decreased with aging time. These spectral changes suggested that the water-crosslinking reaction (hydrolysis followed by condensation reaction) in the EPR-*g*-MTMS system in the presence of the $C_{18}NH_2$-Cu(II)$(acac)_2$ complex proceeded gradually with aging time under the experimental conditions in this study.

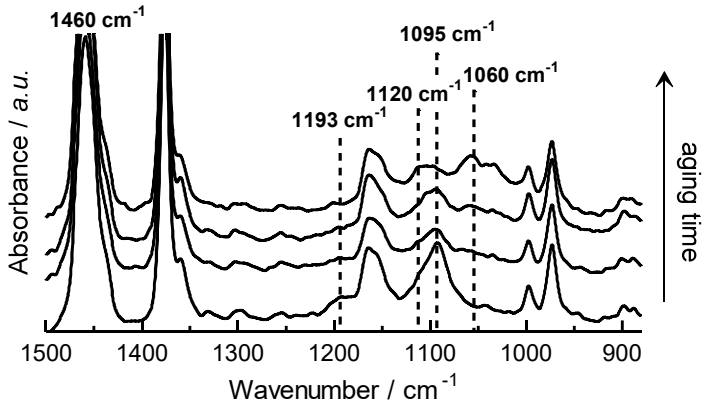

Figure 5-3. Changes in the ATF–FTIR spectra for the water-crosslinking reaction of the EPR-*g*-MTMS system in the presence of the $C_{18}NH_2$–Cu(II)$(acac)_2$ complex (5.0×10^{-4} mol/100 g EPR resin). The peak assignments are included in the text.

Kinetic analysis of the hydrolysis reaction of the EPR-*g*-MTMS systems containing various RNH_2–M(II)$(acac)_2$ complexes using Arrhenius plots

In this study, the amount of methoxysilane groups used during the hydrolysis reaction was determined using the A_{1095}/A_{1460} ratio. The representative changes in the A_{1095}/A_{1460} ratios with the reaction time for the EPR-*g*-MTMS systems containing various RNH_2–Cu(II)$(acac)_2$ complexes at 30, 50, and 80 °C are presented in Figure 5-4. As illustrated in Figure 5-4, r^0_{hyd} (h^{-1}) can be expressed as follows:

$$r^0_{hyd} = \left| \frac{d\left(A_{1095} / A_{1460}\right)}{dt} \right|_{t=0} \quad \text{..... (5.3)}$$

The actual r^0_{hyd} values were obtained by differentiating the quadratic equation used to fit the experimental data in Figure 5-4. Since the observed r^0_{hyd} values increased linearly with increasing the concentration of methoxysilane groups, it was concluded that the diffusion rate of water into the EPR-*g*-MTMS system was not the rate-determining step of the water-crosslinking reaction in this system. The temperature dependence of r^0_{hyd} can

be described using the Arrhenius equation:

$$\ln r^{0}_{\mathrm{hyd}} = \ln A'_{\mathrm{hyd}} - \frac{E_{\mathrm{a,hyd}}}{RT} \quad \text{..... (5.4)}$$

where A'_{hyd} is the empirical constant comprising the frequency factors A and [MTMS]. The $E_{\mathrm{a,hyd}}$ values were calculated from the slopes of the $\ln r^{0}_{\mathrm{hyd}}$ vs. $1/T$ plots for each RNH_2–M(II)$(acac)_2$ complex (Figure 5-5). The calculated $E_{\mathrm{a,hyd}}$ values are summarized in Table 5-2. For convenience, only the water-crosslinking reactions of the EPR-*g*-MTMS systems with M(II)$(acac)_2$ complexes and $C_{18}NH_2$ were investigated. All the RNH_2–M(II)$(acac)_2$ complexes presented good catalytic activity for the water-crosslinking reaction in the EPR-*g*-MTMS system. Moreover, the calculated $E_{\mathrm{a,hyd}}$ values decreased as follows: no catalyst >> M(II)$(acac)_2$ > $C_{18}NH_2$ > RNH_2–M(II)$(acac)_2$ complexes. These results indicate that the catalytic activities of the RNH_2–M(II)$(acac)_2$ complexes for this reaction were significantly higher than those of the previously reported catalysts. To confirm the primary factor that enhanced the activity of the catalysts for hydrolysis reaction, we investigated the acid–base co-catalytic activities of the M(II)$(acac)_2$ and $C_{18}NH_2$ mixtures (i.e., M(II)$(acac)_2$+$C_{18}NH_2$ [axial uncoordinated]) for the water-crosslinking reaction in the EPR-*g*-MTMS system. The $E_{\mathrm{a,hyd}}$ values for the EPR-*g*-MTMS system containing M(II)$(acac)_2$ and $C_{18}NH_2$ mixtures were comparable to that of the $C_{18}NH_2$-catalyzed system (Table 5-2). Conversely, the calculated $E_{\mathrm{a,hyd}}$ value for the EPR-*g*-MTMS system with $C_{18}NH_2$ was significantly higher than those of the EPR-*g*-MTMS systems containing various RNH_2–M(II)$(acac)_2$ complexes. These results suggested that the remarkable catalytic activities of the RNH_2–M(II)$(acac)_2$ complexes for the hydrolysis reaction in the EPR-*g*-MTMS system was ascribed to the *n*-alkylamine axially coordinated with M(II)$(acac)_2$.

The $E_{\mathrm{a,hyd}}$ values for the EPR-*g*-MTMS system with various RNH_2–M(II)$(acac)_2$

complexes varied with the alkyl chain length of the RNH_2 compounds in the axial positions of the $M(II)(acac)_2$ complexes. Since the K_{cpx} values of the RNH_2–$M(II)(acac)_2$ complexes depended on the axial ligands, we expected that the differences in the $E_{a,hyd}$ values were ascribed to the stability of the RNH_2–$M(II)(acac)_2$ complexes in the EPR-*g*-MTMS systems.

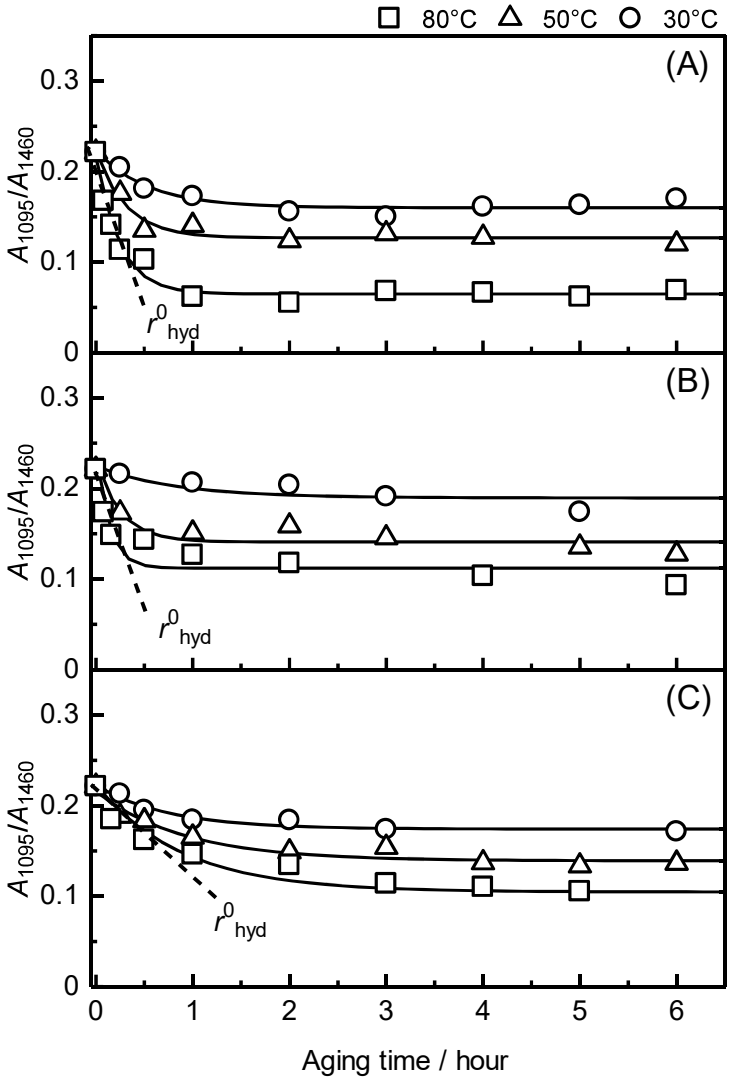

Figure 5-4. Time evolution of the A_{1095}/A_{1460} ratio of the water-crosslinked EPR-*g*-MTMS systems in the presence of (A) $C_{18}NH_2$–Cu(II)(acac)$_2$, (B) $C_{14}NH_2$–Cu(II)(acac)$_2$, and (C) C_8NH_2–Cu(II)(acac)$_2$ at 30 °C (open circle), 50 °C (open triangle), and 80 °C (open square).

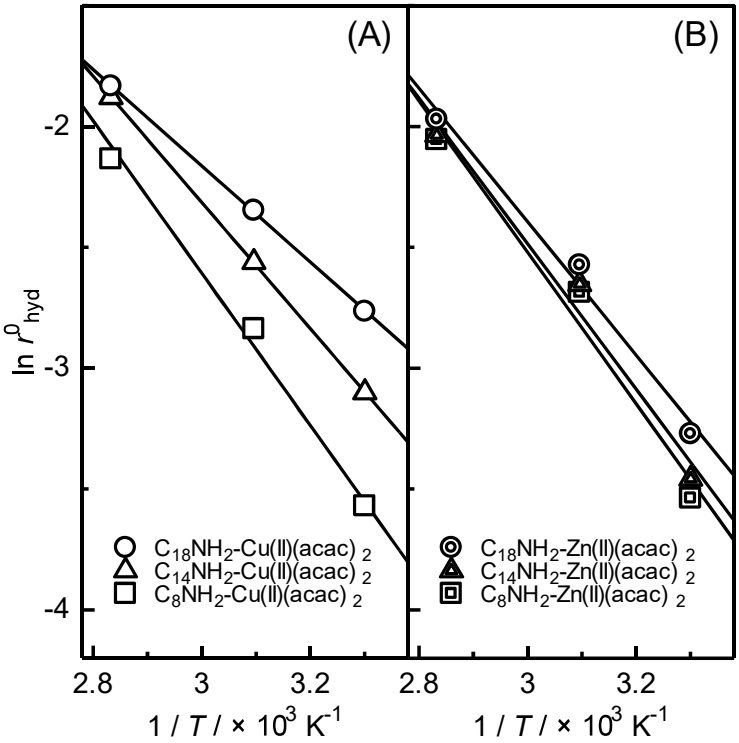

Figure 5-5. Dependence of the logarithmic hydrolysis rates on the reciprocal absolute temperature for the EPR-*g*-MTMS systems in the presence of the (A) RNH_2–Cu(II)$(acac)_2$ and (B) RNH_2–Zn(II)$(acac)_2$ complexes. The solid and dotted lines were obtained using Eq. (5.4).

Table 5-2. Calculated activation energies for the hydrolysis and overall water-crosslinking reactions of EPR-*g*-MTMS ($E_{a,hyd}$ and $E_{a,crk}$, respectively) and average molecular masses between crosslinks (M_c) for the water-crosslinked EPR-*g*-MTMS.

Metal(II) acetylacetonate complex	*n*-Alkylamine compound	Activation Energy [kJ mol^{-1}]		Average molecular weight between crosslinks M_c [c]
		$E_{a,hyd}$ [a]	$E_{a,crk}$ [b]	[g mol^{-1}]
Cu(II)(acac)$_2$	$C_{18}NH_2$	16.6 ± 1.2	46.3 ± 0.8	(7.48 ± 0.5) × 10^4
	$C_{14}NH_2$	21.9 ± 0.8	46.8 ± 0.2	(6.48 ± 0.2) × 10^4
	C_8NH_2	25.9 ± 0.6	47.3 ± 1.2	(5.98 ± 0.8) × 10^4
	no ligand	27.4 ± 1.2	46.9 ± 0.5	(4.22 ± 1.0) × 10^4
Zn(II)(acac)$_2$	$C_{18}NH_2$	19.1± 1.0	50.5 ± 0.8	(5.40 ± 0.5) × 10^4
	$C_{14}NH_2$	25.0 ± 0.9	51.2 ± 0.2	(3.88 ± 0.2) × 10^4
	C_8NH_2	26.1 ± 1.2	51.9 ± 0.5	(3.61 ± 0.1) × 10^4
	no ligand	30.2 ± 1.5	50.3 ± 0.6	(1.72 ± 0.8) × 10^4
Cu(II)(acac)$_2$ + $C_{18}NH_2$ [d]		26.4 ± 0.9	48.1 ± 0.6	---
Zn(II)(acac)$_2$ + $C_{18}NH_2$ [d]		27.1 ± 0.8	51.7 ± 0.2	---
$C_{18}NH_2$		26.8 ± 1.0	56.1 ± 1.0	---
without catalyst		46.9 ± 0.9	71.8 ± 1.2	---

[a] catalyst concentration 5.0 × 10^{-4} mol/100g EPR; [b] determined using ATR-FTIR spectroscopy; [c] determined using gel fraction measurements; [d] aged in 80 °C water for 24 h; [e] mixtures of M(II)(acac)$_2$ complexes and $C_{18}NH_2$.

Kinetic analysis of the overall water-crosslinking reactions of the EPR-*g*-MTMS systems containing RNH_2–M(II)$(acac)_2$ complexes using gel fraction measurements

The typical time evolution of the gel contents of the EPR-*g*-MTMS systems containing RNH_2–Cu(II)$(acac)_2$ complexes at 30, 50, and 80 °C is presented in Figure 5-6 ((A) $C_{18}NH_2$, (B) $C_{14}NH_2$, and (C) C_8NH_2). The rates and degrees of overall water-crosslinking increased with aging temperature. For example, for the $C_{18}NH_2$–Cu(II)$(acac)_2$ complex (Figure 5-6(A)), the gel content reached a plateau after 2 h at 80 °C; however, the gel content still increased after 4 h at 30 °C. The r^0_{crk} values were determined using the gel contents, as follows:

$$r^0_{crk} = \left| \frac{d(\text{gel content})}{dt} \right|_{t=0} \quad \text{..... (5.5)}$$

The dependence of the $\ln r^0_{crk}$ values for the EPR-*g*-MTMS systems with various RNH_2–M(II)$(acac)_2$ complexes on the reciprocal absolute temperature is presented in Figure 5-7. The data can be fitted well using a straight line over a significant temperature range. According to the Arrhenius equation:

$$\ln r^0_{crk} = \ln A'_{crk} - \frac{E_{a,crk}}{RT}, \quad \text{..... (5.6)}$$

where A'_{crk} is the empirical constant comprising the frequency factors A for the overall-water-crosslinking reaction and [MTMS]. Therefore, we determined the $E_{a,crk}$ values of all the catalyst from the slopes of the $\ln r^0_{crk}$ vs. $1/T$ plots, and the results are listed in Table 5-2. The $E_{a,crk}$ values for the EPR-*g*-MTMS systems containing various RNH_2–M(II)$(acac)_2$ complexes were significantly smaller than those of the EPR-*g*-MTMS system containing $C_{18}NH_2$ and were comparable to those of the EPR-*g*-MTMS systems containing the corresponding M(II)$(acac)_2$ systems. Furthermore, we determined the $E_{a,crk}$ values for the EPR-*g*-MTMS systems containing mixtures of M(II)$(acac)_2$ complexes and

$C_{18}NH_2$ [axial uncoordinated] as acid–base co-catalysts. The obtained $E_{a,crk}$ values were comparable to those of the EPR-*g*-MTMS systems containing the corresponding M(II)$(acac)_2$ complexes (Table 5-2). Therefore, the catalytic activity for the condensation reaction in the EPR-*g*-MTMS system depended primarily on the presence of the metal(II) ions in the RNH_2–M(II)$(acac)_2$ complexes, whereas the catalytic effect of the axially coordinated *n*-alkylamines was negligible. The experimental data revealed that catalytic activities of the RNH_2–Cu(II)$(acac)_2$ complexes were stronger than those of the RNH_2-Zn(II)$(acac)_2$ complexes.

M_c values are critical parameters used to characterize crosslinked polymers, and directly related to the crosslinking densities of the polymers. The M_c values of the EPR-*g*-MTMS systems containing various RNH_2–M(II)$(acac)_2$ complexes aged for 24 h in 80 °C water were calculated using the Flory–Rehner equation (Eq. (3.1), and the results are listed in Table 4-2. The M_c values of the EPR-*g*-MTMS systems containing the RNH_2–M(II)$(acac)_2$ complexes decreased as follows: M(II)$(acac)_2$ < C_8NH_2–M(II)$(acac)_2$ < $C_{14}NH_2$–M(II)$(acac)_2$ < $C_{18}NH_2$–M(II)$(acac)_2$, which matched the trend in the $E_{a,hyd}$ values reported in the previous section. The differences in the M_c values between the crosslinked EPR-*g*-MTMS systems catalyzed by various RNH_2–M(II)$(acac)_2$ complexes indicated that the RNH_2–M(II)$(acac)_2$ complexes played a critical role in the formation of the silane–water-crosslinking network structures in the EPR-*g*-MTMS systems.

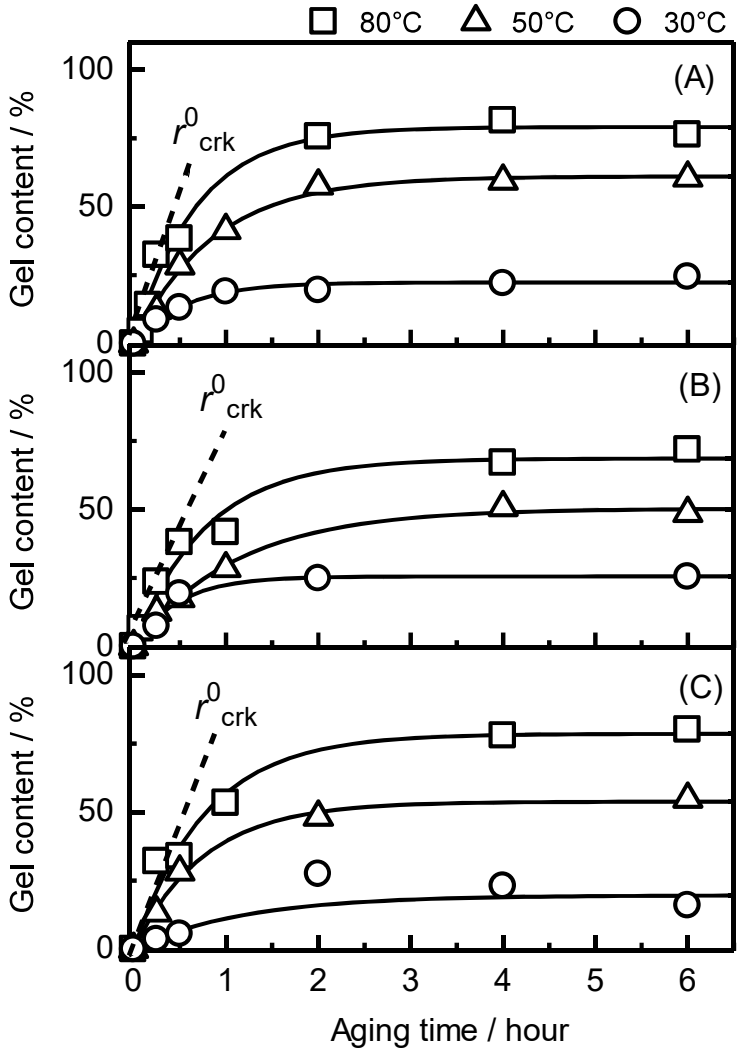

Figure 5-6. Time evolution of the gel contents of the water-crosslinked EPR-*g*-MTMS in the presence of (A) $C_{18}NH_2$-Cu(II)(acac)$_2$, (B) $C_{14}NH_2$-Cu(II)(acac)$_2$ and (C) C_8NH_2-Cu(II)(acac)$_2$ at 30 °C (open circle), 50 °C (open triangle), and 80 °C (open square).

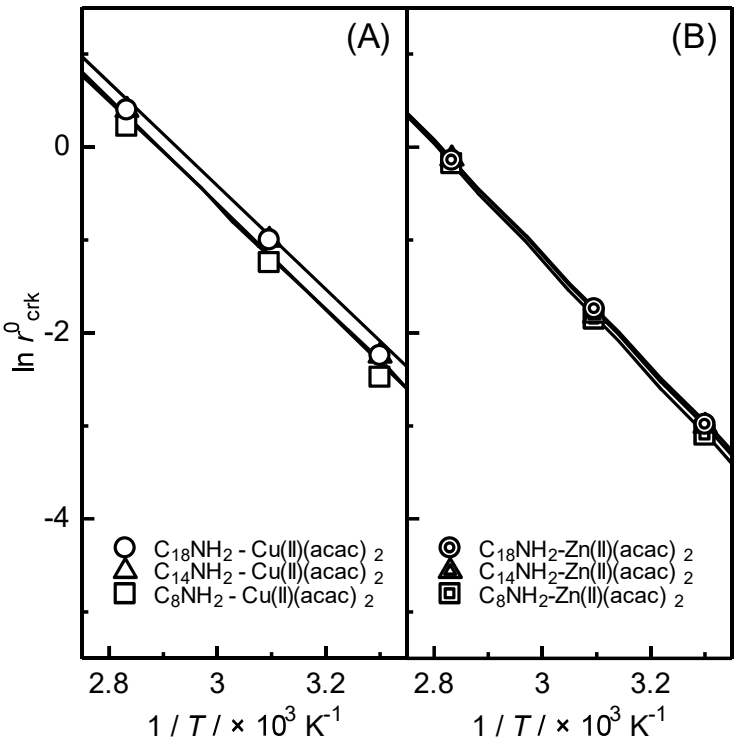

Figure 5-7. Dependence of the logarithmic overall crosslinking rates on the reciprocal absolute temperature for the EPR-*g*-MTMS in the presence of (A) RNH_2-Cu(II)$(acac)_2$ complex and (B) RNH_2-Zn(II)$(acac)_2$ complexes. The solid and dotted lines were obtained using Eq. (5.6).

Proposed catalytic mechanism for the water-crosslinking reaction in the EPR-*g*-MTMS systems containing the RNH_2–M(II)$(acac)_2$ complexes

Using the aforementioned UV–vis absorption and ATR–FTIR spectroscopy results and gel fraction measurement data, we evaluated the catalytic activities of the RNH_2–M(II)$(acac)_2$ complexes for the water-crosslinking reaction in the EPR-*g*-MTMS system. The following conclusions were drawn. (i) The ATR–FTIR spectra for the hydrolysis reactions of the EPR-*g*-MTMS systems containing various RNH_2–M M(II)$(acac)_2$ complexes were similar; however, the corresponding $E_{a,hyd}$ values were significantly different. (ii) The axially coordinated *n*-alkylamine compounds played a critical role in the remarkable catalytic activities of the RNH_2–M(II)$(acac)_2$ complexes for the hydrolysis step of the water-crosslinking reactions of the EPR-*g*-MTMS systems. (iii) The $E_{a,crk}$ values for the EPR-*g*-MTMS systems containing various RNH_2–M M(II)$(acac)_2$ complexes were independent on the alkyl chain lengths of the axial amine ligands; however, the metal ions of the RNH_2–M(II)$(acac)_2$ complexes significantly affected the catalytic activities of the complexes for the overall water-crosslinking reaction of the EPR-*g*-MTMS systems.

To date, several studies have been conducted on silicate sol–gel systems using acid and base catalysts.[14-16] Despite their shortcomings, one-component acid–base catalysts possess two types of catalytic active sites in one molecule, unlike their two-component counterparts comprising acid and base co-catalysts. Therefore, acid–base hybrid catalysts can exhibit bifunctional behavior. The RNH_2–M(II)$(acac)_2$ complexes in this study presented dual catalytic active sites. In particular, the metal ions of the M(II)$(acac)_2$ complexes and the N atoms of the *n*-alkylamine compounds served as the acidic and basic sites, respectively. According to the associative substitution mechanism based on the Eigen–Wilkins model, the free water molecule initially present in the

coordination sphere of each anhydrous RNH_2–M(II)$(acac)_2$ complex in the EPR-*g*-MTMS system would immediately enter the first coordination sphere of the RNH_2–M(II)$(acac)_2$ complex. Typically, hydrates are more widely used as nucleophilic reactants to attack the Si atoms of alkoxysilanes. Therefore, during the hydrolysis step, the basic amine groups of the hydrated RNH_2–M(II)$(acac)_2$ complexes would react with the Si atoms of the methoxysilane groups of the EPR-*g*-MTMS systems, forming silanol groups. During the condensation step, the Lewis acid metal sites of the nucleophilic hydrated RNH_2–M(II)$(acac)_2$ complexes would attack the resulting silanol groups, subsequently generating siloxane structures.

Conclusion

We investigated the catalytic activities of several novel acid–base hybrid catalysts, comprising RNH_2–$M(II)(acac)_2$ complexes, for the water-crosslinking reaction of EPR-*g*-MTMS. Using the Arrhenius equation, we demonstrated that the $E_{a,crk}$ values of the RNH_2–$M(II)(acac)_2$ complexes with longer alkyl chains were lower than those of the complexes with shorter alkyl chains. The differences in the kinetics of the hydrolysis reactions were primarily attributed to the stabilities of the RNH_2–$M(II)(acac)_2$ complexes. The RNH_2–$M(II)(acac)_2$ complexes with longer alkyl chain compounds were less stable than those with shorter alkyl chains. Moreover, the $E_{a,crk}$ values for the RNH_2–$M(II)(acac)_2$ complexes with the same metal ion were not different from those of the axially coordinated *n*-alkylamine compounds, whereas the catalytic activities of the RNH_2–$M(II)(acac)_2$ complexes with different metal ions were significantly different. Therefore, we proposed that the catalytic active sites of the RNH_2–$M(II)(acac)_2$ complexes for the hydrolysis and condensation reactions in the EPR-*g*-MTMS system were different. In particular, the axially coordinated *n*-alkylamine compounds served as basic catalysts for the hydrolysis step, whereas the metal ions of the $M(II)(acac)_2$ complexes served as acidic catalysts for the condensation step. We believe that our results are critical in developing a comprehensive catalytic mechanism for the water-crosslinking reaction of alkoxysilane and can promote further research into crosslinking, thereby advancing silicon resin chemistry.

References

1. Z. H. Shao, H. B. Zhang, *Chem. Soc. Rev.*, **2009**, *38*, 2745-2755.
2. I. Ibrahem, A. Cordova, *Angew. Chem. Int. Ed.*, **2006**, *45*, 1952-1956.
3. S. Chem, H. Wang, Z. Li, F. Wei, H. Zhu, S. Xu, J. Xu, J. Liu, H. Gebru, K. Guo, *Polym. Chem.*, **2018**, *9*, 732-742.
4. S. Brahma, S. A. Shivashankar, *J. Mol. Struct*., **2015**, 1101, 41-49.
5. K. Ueda, *Chem. Soc. Jpn.*, **1978**, *51*, 805-810.
6. K. J. de Almeida, T. C. Ramalho, Z. Rinkevicus, O. Vahtras, H. Agren, A. Cesar, *J. Phys. Chem. A*, **2011**, *115*, 1331-1339.
7. M. Anjomsjhoa, H. Hadadzadeh, M. T. Mahani, S. J. Fatemi, M. A. Sardou, H. A. Rudbari, V. M. Nardo, *Eur. J. Med. Chem.*, **2015**, *96*, 66-82.
8. A. A. Soliman, A. Taha, W. Linert, *Spectrochim. Acta A Mol. Biomol. Spectrosc.*, **2006**, *64*, 1058-1064.
9. W. Xu, T. Wang, *Langmuir*, **2017**, *33*, 82-90.
10. C. H. Ke, N. C. Li, *J. Inorg. Nucl. Chem.*, **1969**, *31*, 1383-1393.
11. S. H. Liu, K. A. Fichthorn, *J. Phys. Chem. C.*, **2017**, *121*, 22531-22541.
12. D. A. Fine, *J. Inorg. Nucl. Chem.*, **1973**, *35*, 4023-4028.
13. J. M. Haigh, N. P. Slabbert, D. A. Thornton, *J. Inorg. Nucl. Chem.*, **1970**, *32*, 3635-3640.
14. S. Katayama, I. Yoshinaga, Y. Kubo, N. Yamada, *J. Ceram. Soc. Jpn.*, **2003**, *111*, 743–748.
15. C.R. Silva, C. Airoldi, *J. Colloid Interface Sci.*, **1997**, *195*, 381–387.
16. A. Mehner, J. Dong, T. Prenzel, W. Datchary, D.A. Lucca, *J. Solgel Sci. Technol.*, **2010**, *54*, 355–362.

Chapter 6

Concluding Remarks

This thesis reported the specific effects of the building blocks on the catalytic activities of the Lewis acid and base catalysts for the silane–water-crosslinking reaction in polymer systems, and the newly designed bifunctional water-crosslinking catalysts comprising Lewis acid and Lewis base catalysts for the first time.

There are many inconsistent reports to develop new general catalytic systems to expand the applications of silane water-crosslinkable polyolefins. Among the developed systems, metal complexes with Lewis acid catalytic active sites and organocatalysts with Lewis base active sites have recently attracted increasing attention owing to their high catalytic efficiencies and unique properties. Furthermore, it was reported that judicious design of the building blocks of these compounds can enhance their Lewis acidity and basicity. However, to date, the specific effects of the building blocks on the catalytic activities of these compounds for the silane–water-crosslinking reaction in polymer systems have not been elucidated and should be further investigated.

In this thesis, I investigated the effects of the building blocks on the catalytic performance of three catalytic systems for the water-crosslinking reaction of an alkoxysilane-grafted polyolefin system. **Chapter 3** and **Chapter 4** focused on the effects of βDiK ligand on the catalytic performance of Lewis acid Cu(II)(βDiK)$_2$ complexes and those of substituents on the activity of organophosphorus catalysts, respectively. In **Chapter 3** and **Chapter 4**, the effects of building blocks on the catalytic activities were estimated experimentally and theoretically. The results in **Chapter 3** and **Chapter 4**

consistently demonstrated that the catalytic performance of Lewis acid and base catalysts could be finely controlled by judiciously selecting the coordinate ligands and substituents, and developed more efficient crosslinking catalysts than the previously reported catalytic system. In **Chapter 5**, I introduced the concept of acid–base hybrid catalysts for the water-crosslinking reaction of alkoxysilane-grafted polyolefin systems. Hybrid catalysts were synthesized using $M(II)(acac)_2$ complexes and RNH_2 compounds as the Lewis acid and Lewis base catalysts, respectively. Unlike the two-component acid and base co-catalyst systems, the RNH_2–$M(II)(acac)_2$ complexes presented two types of catalytic active sites within the same molecule. We believe that the newly proposed mechanism using acid–base hybrid catalysts can be used to further develop tunable silane water-crosslinkable polyolefins for various applications.

In summary, three catalytic systems for the water-crosslinking reaction of silane-grafted polyolefins were developed, and the factors contributing to the remarkable catalytic performance of each system were identified. Furthermore, I concluded that it was possible to achieve greater efficiency in catalyst design by the holistic approach including advanced collaboration of experimental and computational studies. Kinetic and theoretical studies demonstrated that the electron withdrawing / donating characters of building blocks in catalysts could precisely tune the Lewis acidity and basicity of catalysts, and improve their catalytic performance for the silane water-crosslinking reaction in polyolefin system. Although the details of catalytic mechanism require further investigation, we anticipate that these findings will lead to new concepts for the further design of crosslinking catalyst for the silane water-crosslinking reaction in polymer system.

List of Publications

1. A novel efficient catalyst for water-crosslinking reaction of silane-grafted polyolefin system: Specific influence of axially coordinated n-alkylamine ligand on catalytic abilities of metal acetylacetonate complex
   S. Tanaka, K. Adachi
   Mater. Today Commun. **2019** 21 100584.

2. Origin of catalytic activity differences between phosphine and phosphine oxide-based structures in the water-crosslinkable polyalkoxysilane composition
   S. Tanaka, K. Adachi
   Polyolefins J. **2021** 8 49-62.

3. Kinetic Insights into Metaphosphoric Acid-Catalyzed Water-Crosslinking Reactions in Silane-Grafted Polyolefin System
   S. Tanaka, K. Adachi
   Phosphorus Sulfur **submitted.**

4. Enhancing Catalytic Activity of Copper(II) Complexes by Curcuminoid as Electron-Withdrawing Ligand for Silane Water-Crosslinking Reaction: A Joint Experimental and Theoretical Study
   S. Tanaka, M. Imamura, K. Adachi
   J. Sol-Gel Sci. Technol. **submitted.**

List of Awards

1. 第 25 回中国四国支部分析化学若手セミナー　優秀ポスター賞

2. 第 27 回中国四国支部分析化学若手セミナー　優秀ポスター賞

Acknowledge

First and foremost, I would like to show my greatest appreciation to my supervisor, Assoc. Prof. Kenta Adachi. He offered me this wonderful opportunity. Thanks for guiding, supporting, and giving me a lot of delightful ideas throughout my thesis. I have learned a great deal from his unique perspective on research, scientific attitude, sharp insight on issue, personal integrity, and expectation of excellence.

I would like to extend my sincere gratitude to Prof. Jun Kawamata, Prof. Suzuko Yamazaki, Prof. Kensuke Honda, and Prof. Toshihiro Murafuji for their contribution in my defense.

I am thankful to my friends and members in Adachi laboratory for their valuable contribution, not only about work and also about my life during my study in Yamaguchi University.

Finally, this thesis have not been possible without support and encouragement from my family, Kyoko, Hinako, and Sakurako, throughout the years of my study. Thanks very much to them for 100 % supporting and endless love throughout my life.

Shohei Tanaka

Graduate School of Sciences and Technology for Innovation

Yamaguchi University

1677-1 Yoshida, Yamaguchi, Yamaguchi 753-8512, Japan

February, 2022

Appendices

Appendix 1 Silane grafting onto the EPR copolymer

ATR–FTIR spectroscopy was used to evaluate the extent of silane grafting of the EPR copolymer. Prior to the ATR–FTIR measurements, EPR-*g*-MTMS was washed with excess acetone to remove unreacted MTMS. The ATR–FTIR spectra of pristine EPR and EPR-*g*-MTMS after grafting are presented in Figure A1. Unlike the ATR–FTIR spectrum of pristine EPR, that of EPR-*g*-MTMS presented several characteristic peaks of MTMS. The absorption peaks at 803, 1095, 1193, and 1720 cm^{-1}, which correspond to the Si–O bending, Si–O stretching, and Si–C stretching vibrations of the functional Si–OCH_3 groups and the C=O stretching vibration of the methacryl groups of MTMS, respectively, were present in the spectrum of EPR-*g*-MTMS prepared using the free radical method. As mentioned in the literature, because of the presence of the reactive trimethoxysilyl group in its structure, MTMS was sensitive to homo-polymerization and should be carefully manipulated. To confirm the self-reactivity of MTMS, we obtained the ATR–FTIR spectra of MTMS mixed with DCP and heated to 180 °C for more than 15 min. The intensity of the peak at 1720 cm^{-1}, which was attributed to the C=C bonds in MTMS, did not change. These results indicated that MTMS homo-polymerization could not occur under these conditions and most of the MTMS was successfully grafted onto EPR.

In this study, we calculated the degree of silane grafting using FTIR spectroscopy. The ratio between the intensity of the absorbance peak at 1095 cm^{-1} (A_{1095}), which was ascribed to the –$SiOCH_3$ groups and that at 1460 cm^{-1} (A_{1460}; internal reference), which was attributed to the bending of the –CH_3 groups, was used as an index

of the extent of silane grafting onto the EPR resin. The peak intensity analysis results presented good reproducibility. Lastly, the extent of silane grafting onto EPR in this study was determined to be approximately 4.8 phr.

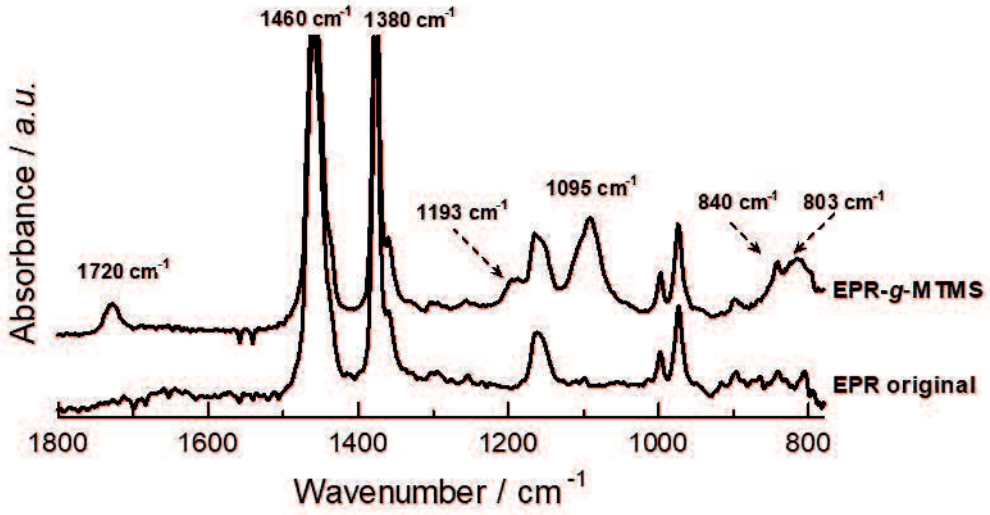

Figure A1 ATR-FTIR spectra of virigin EPR and MTMS-grafted EPR (EPR-*g*-MTMS)

Appendix 2 NMR spectrum of curc{Ph}$_2$

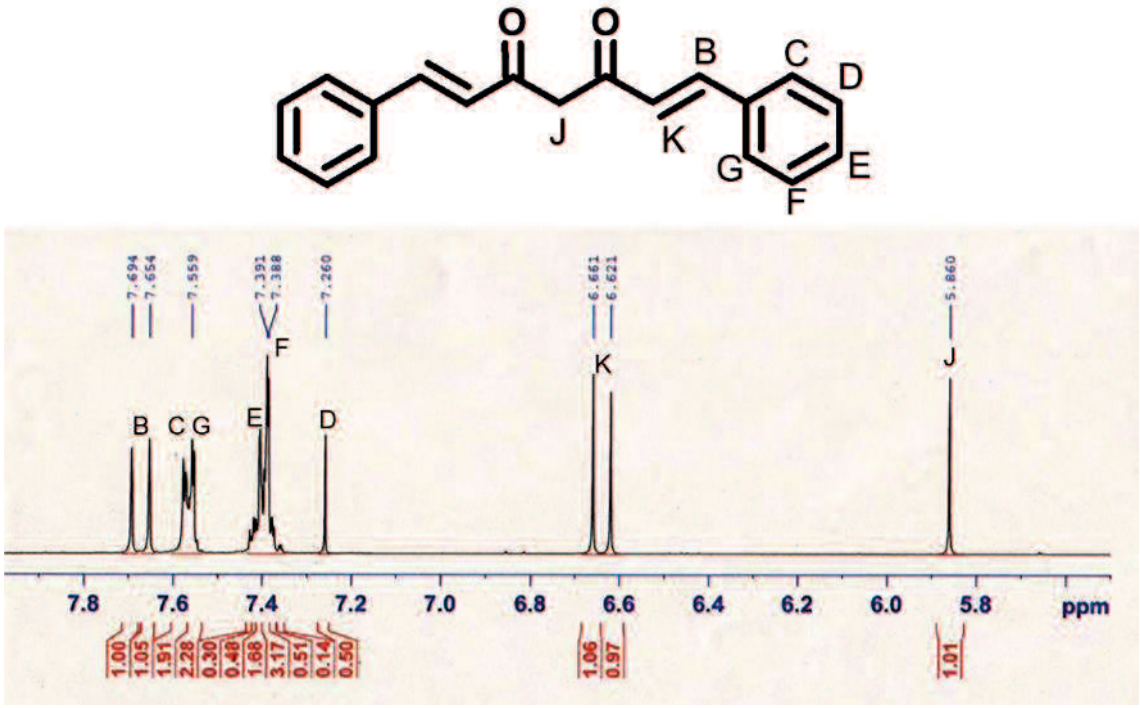

Appendix 3 NMR spectrum of curc{Ph(OH)$_2$}$_2$